Structure and properties of SiO_2-bearing aqueous fluids and glasses from first principles modeling

Dissertation zur Erlangung des Doktorgrades
im Fachbereich Geowissenschaften
an der Freien Universität Berlin

vorgelegt von

Georg Spiekermann

Berlin, August 2012

Öffentliche Verteidigung:
23. November 2012, 14:30 Uhr, FU Berlin, Campus Lankwitz, Gebäude C, Raum 014

Promotionskommission:

Prof. Harry Becker,	FU Berlin	(Vorsitzender)
Dr. Sandro Jahn,	FU Berlin	(Erstgutachter)
PD Dr. Ralf Milke,	FU Berlin	(Zweitgutachter)
Prof. Serge Shapiro,	FU Berlin	
Dr. Philipp Gleißner,	FU Berlin	

Table of Contents

Zusammenfassung

Ungeordnete silikatische Materialien kommen in der Natur vor in Form von Schmelzen und Gläsern sowie als Silikatspezies in wässriger Lösung. Diese Materialien sind von großer Bedeutung in verschiedenen Bereichen der Geowissenschaften. Es ist eines der grundlegenden Ziele in der Untersuchung solcher Materialien, die Zusammenhänge zwischen der atomaren Struktur und makroskopischen Eigenschaften wie zum Beispiel der Viskosität von Schmelzen oder der Löslichkeit von SiO_2 in Wasser besser zu verstehen. Die ab initio Modellierung gibt Einblicke auf der atomaren Skala in Struktur und Eigenschaften. Sie trägt somit zum Verständnis von ungeordnetem silikatischem Material bei. Mit den Mitteln der ab initio molekulardynamischen Modellierung und nachgeordneten Auswertungsalgorithmen untersucht die vorliegende Arbeit einige strukturelle und dynamische Eigenschaften von Silikatgläsern und Silikatspezies in wässriger Lösung.

Im ersten Teil der Arbeit stellen wir berechnete Schwingungseigenschaften von Silikatspezies in Magnesiosilikatgläsern und wässrigen Fluiden vor. Diese können experimentell mit Hilfe von Raman-Spektroskopie gemessen werden. Allerdings besteht eine der größten Herausforderungen der experimentellen Raman-Spektroskopie in der Interpretation der Spektren, das heißt, in der Zuordnung der beobachteten Raman-Banden zu einzelnen Silikatspezies und deren strukturellen Einheiten. Die für gegebene Silikatspezies berechneten Frequenzen helfen, die theoretische Basis für die Zuordnung der Banden zu verbreitern. Zu diesem Zweck haben wir die Methode der Moden-Zerlegung auf Silikatspezies in allen Graden der Polymerisierung erweitert und die Algorithmen in Fortran90 zu dem Programm SPECDOC (SPECtral Decomposition Of Calculated trajectories) umgesetzt. Diese Methode zerlegt die totale Schwingungs-Zustandsdichte der ab initio molekulardynamischen Trajektorie einer gegebenen Silikatspezies in Subspektren von theoretisch hergeleiteten Normalmoden-ähnlichen Schwingungen wie zum Beispiel der Raman-spektroskopisch bedeutsamen symmetrischen Streckschwingung des SiO_4^{4-} Tetraeders. Die Ergebnisse in der Form von Subspektren pro Mode und Spezies erlauben es, präzise Schwingungsfrequenzen und deren Verschiebung bei sich änderndem Polymerisierungsgrad zu bestimmen. Eines der wichtigsten Resultate dieser Untersuchung ist die Bestätigung der bimodalen Verteilung der Schwingungsdichte der symmetrischen Streckschwingung von Q^2-Spezies, die vor einigen Jahren von Experimentatoren vorgeschlagen worden war. Diese bimodale Verteilung der Q^2-Spezies sollte die übliche Interpretation von Raman-Spektren bezüglich des Polymerisierungsgrades von Silikatspezies in Gläsern und Fluiden verändern. Ein weiteres wichtiges Ergebnis ist die Vorhersage einer Schwingungsbande des $H_6Si_2O_7$ Dimers bei 790 bis 800 cm^{-1}. Dieser Schwingungsbeitrag des Dimers könnte der Grund für die bisher unerklärte Verschiebung des bislang nur dem H_4SiO_4 Monomer zugeordneten Raman-Bandes bei 770 cm^{-1} zu höheren Wellenzahlen sein, wie sie in einigen Raman-Studien über wässrige Silikatlösungen beobachtet wurde.

Im zweiten Teil der vorliegenden Arbeit untersuchen wir die Struktur und einige dynamische Eigenschaften von überkritischem SiO_2-reichem wässrigen Fluid. Das System SiO_2-H_2O repräsentiert in erster Näherung die Interaktion von Fluiden und silikatischem Gestein. Natürlich vorkommende überkritische silikatreiche wässrige Fluide könnten die magmatischen Prozesse in Subduktionszonen bestimmend beeinflussen. Sie entstehen bei hohen Drücken von über 1 GPa und hohen Temperaturen oberhalb von etwa 1300 K. Das macht experimentelle Untersuchungen äußerst schwierig. In relativ großen Modellen von etwa 200 Atomen konnten wir eine deutliche Zunahme des Polymerisierungsgrades bei gleichzeitigem Entstehen von Wassermolekülen beobachten, nachdem in der molekulardynamischen Modellierung die Temperatur von 3000 K auf 2400 K gesenkt wurde. Das interpretieren wir als Vorläufer der bei niedrigeren Temperaturen zu erwartenden auftretenden Entmischung der Komponenten SiO_2 und H_2O.

Diese konsistent in mehreren großen Modellen beobachteten strukturellen Veränderungen wurden nicht beobachtet in mehreren Modellen von der üblichen Größe von etwa 100 Atomen. Diese Tatsache deckt auf, dass Modellierungen von etwa 100 Atomen einem Größen-Effekt unterliegen, der strukturelle Veränderungen verhindert oder sogar zu gegenläufigen Entwicklungen zu größeren Modellen führt. Das gilt wahrscheinlich generell für die Modellierung von teilweise depolymerisierten Silikatschmelzen. Wir haben die Si-O Bindungsdynamik untersucht, das heißt, die Häufigkeit des Brechens und Entstehens von Si-O Bindungen. Die Ergebnisse zeigen, dass schon bei 2400 K die Bindungsdynamik gegenüber höheren Temperaturen so stark abgenommen hat, dass das Erreichen von strukturellem Gleichgewicht bei 2400 K die übliche Dauer der Trajektorien von ab initio Molekulardynamik deutlich überschreitet. Diese Entdeckung legt die engen Grenzen der ab initio molekulardynamischen Modellierung von silikatreichen wässrigen Fluiden offen. Umgekehrt unterstützen unsere Ergebnisse die Verlässlichkeit und Vorhersagekraft von ab initio Molekulardynamik, wenn diese Grenzen bei der Modellierung berücksichtigt werden.

Summary

Disordered silicate materials occur in nature as melts, glasses and silica species in aqueous fluids. It is therefore of great importance in numerous branches of geosciences. Understanding the relation between the atomic-scale structure of disordered silicate materials and their macroscopic properties such as melt viscosity or silica solubility in water is one of the fundamental aims of experimental investigation of these materials. Ab initio modeling provides atomic-scale insight into both the structure and macroscopic properties, and thereby contributes to our understanding of disordered silicate materials. The present work investigates several structural and dynamical properties of silicate glasses and silica species in aqueous fluids by means of ab initio molecular dynamics (MD) and post-run evaluation tools.

In the first part of this work, we present calculated vibrational properties of silica species in magnesiosilicate glasses and in aqueous fluids. In experiment, these are probed by Raman spectroscopy. However, one of the biggest difficulties in experimental Raman spectroscopy of disordered silicate materials is the assignment of observed vibrational bands to specific silica species and their structural subunits. Ab initio calculated frequencies of given species help to enhance the theoretical basis for the experimental assignment. For that aim, we extended the mode-decomposition approach to the vibrational modes of silica species in all degrees of polymerization, and implemented it in the SPECDOC software (SPECtral Decomposition Of Calculated trajectories), written in Fortran90. The approach decomposes the complete vibrational density of states of silica species from ab initio MD trajectories into subspectra of theoretically well-defined normal mode-like vibrations such as the Raman spectroscopically important SiO_4^{4-} tetrahedral symmetric stretch. These subspectra allowed us to obtain precise mode-wise vibrational frequencies and polymerization-driven frequency shifts. One of the main findings is the corroboration of the bimodal vibrational contribution of the tetrahedral symmetric stretch of Q^2-species which had been proposed by a group of experimentalists a few years ago. This finding changes the interpretation of Raman spectra with respect to the degree of polymerization of the silica species in a glass or a fluid. Another important result is the prediction of a vibrational contribution of the $H_6Si_2O_7$ dimer at 790 to 800 cm^{-1}. This vibrational contribution could be the reason for a hitherto unexplained shift and a shoulder of the important 770 cm^{-1} band observed in several Raman studies of silica in aqueous fluids.

In the second part of this work, we investigate the structure and several dynamical properties of a supercritical silica-rich aqueous fluid with 77wt% SiO_2. The system SiO_2-H_2O is a first order chemical approximation of fluid-rock interaction, and naturally occurring supercritical hydrous silicate fluids are presumed to govern magmatic processes in the crustal wedge above subduction zones. They form under high pressure above 1 GPa and high temperatures above 1300 K, which makes their experimental investigation extremely challenging. In ab initio MD models of about 200 atoms we found that the average degree of polymerization remarkably increases after the fluid was quenched from the typical MD temperature for silica of 3000 K down to 2400 K. We interpret this as a precursor to the formation of nanoscale compositional heterogeneities in the supercritical fluid, which would eventually lead to the unmixing of the two phases at even lower temperatures and pressures. This observed structural changes do not occur in models of the commonly used size in ab initio MD of about 100 atoms. On the contrary, the 100 atom models decrease their average degree of polymerization after decrease of temperature. This reveals an impact of the model size on the atomic structure of the silica-rich fluid which may be valid for partially depolymerized silicate melts in general. We analyzed the Si-O bond breaking dynamics as a function of temperature. The result reveals the low-temperature limitation of MD of silica-bearing fluids and partially depolymerized silicate melts. Our results show that already at 2400 K, the achievement of structural equilibrium is beyond the computationally affordable ab initio MD run durations of up to

200 ps. These findings highlight the limitations of ab initio MD for the investigation of structural equilibrium in silica-rich aqueous fluids. In turn, these results strengthen the reliability and predictive power of ab initio MD, if the limitations with respect to structure and dynamics are carefully observed.

Chapter 1
Introduction

1.1 Motivation

Silicon dioxide (SiO_2) is the most abundant chemical component in rock-forming minerals of the Earth's crust and mantle. Down to a depth of several hundred kilometers, the basic structural unit of the SiO_2-component is the SiO_4^{4-} tetrahedron. It can form one-, two- or three-dimensional networks and clusters, with each Si-O-Si bridging oxygen shared by two tetrahedra. The structure and properties of crystalline silicate solids are governed by the degree of connectivity of the SiO_2 network to such an extent that the characteristics of the SiO_2 network are the basis of the ordering systematics of all crystalline silicate materials. For instance, in feldspars, quartz and other polymorphs of pure SiO_2, the network is completely polymerized and each oxygen is shared by two SiO_4^{4-} tetrahedra. In pyroxenes, amphibols and mica the network is partly polymerized, and each tetrahedron is built from Si-O-Si bridging oxygen and Si-O^- terminal (non-bridging) oxygen atoms.
Knowledge of the various naturally occurring forms of *disordered* silicate materials is also crucial for various branches in geosciences. One form of disordered silicate material is the molten form of silicate minerals. The importance of silicate melt (that is, magma) is particularly evident at active volcanoes around the world. But magma is even more important for the Earth's structure than as the agent of volcanism at the Earth's surface. There is geophysical evidence from seismology and magnetotellurics that suggests the existence of magma at various depths throughout the Earth's mantle (Baba et al., 2006; Brasse and Eydam, 2008; Schilling et al., 2006; Schilling and Partzsch, 2001; Shankland et al., 1981). At an early stage of the Earth's history, its surface has probably evolved from a hot magma ocean to a cold solid crust, chemically differentiated from the mantle (Adjaoud et al., 2008). In this scenario, many important questions about silicate melts remain open. For instance, the density difference between a silicate melt and the surrounding minerals determines whether the melt ascends, descends, or buoyantly remains at a certain depth in the mantle (de Koker et al., 2008). The viscosity of magma influences its speed of ascent (Hack and Thompson, 2010). The amount of H_2O that dissolves in silicate melt influences the melt's viscosity and also affects our understanding of the Earth's water cycle (Hack and Thompson, 2010). These questions show how important it is for geology to know about non-crystalline silicate material in its liquid state.
When a silicate melt is cooled sufficiently quick below the crystallization temperature of expected silicate minerals, the network-forming ability of the SiO_4^{4-} tetrahedra may prevent crystallization. The lack of long-range order of the silicate network in the molten state is then preserved, and the disordered state is "frozen in". This state is referred to as glass. The importance of silicate glass in technical applications such as window glass, optical devices and many other applications does not require emphasis. Silicate glasses also occur in nature. For example, obsidian is a rock formed almost entirely by glass. Many basalts contain several volume percent of interstitial glass. The glassy state of silicate material is commonly considered as a structural analog to its molten state, which is difficult to investigate experimentally because of the required high temperature. Therefore, a big part of the research aiming at silicate melts is carried out on silicate glasses instead (Mysen and Richet, 2005; McMillan, 1984).
The dissolution in aqueous fluid is yet another state of the component SiO_2 that is important for a range of branches in geosciences. The fluids present in the Earth's crust transport large amounts of SiO_2. Modeling of the solubility of SiO_2 with varying pressure, temperature and presence of other components

requires an understanding of the speciation of SiO_2, that is, the structures it forms in the fluid (Hunt and Manning, 2012; Gerya et al., 2005; Felmy et al., 2001). A technical application of silica-rich solutions is the hydrothermal production of zeolites that are important for instance as catalysts the chemical industry (Szyja et al., 2009).
At pressures below 1 GPa, the solubility of SiO_2 in aqueous fluid and, vice-versa, of H_2O in silicate melts is limited to a few mol% and increases slowly with increasing temperature. However, at pressure and temperature conditions of the Earth's lower crust, the aqueous fluid and silicate melt (as simplified in the system SiO_2-H_2O) become mutually completely miscible. These conditions exist for example in subduction zones, where large amounts of aqueous fluids are released from the subducted slab and potentially form such a supercritical silica-rich fluid (Shen and Keppler, 1997). Knowledge of its properties is important for the understanding of the subduction-zone related processes (Audétat and Keppler, 2004). However, the experimental investigation of such fluid is very challenging.

1.2 Experimental structural investigation

SiO_2-bearing melts, glasses and aqueous fluids share fundamental structural aspects. In any of those types of materials, the SiO_4^{4-} tetrahedra form clusters and networks without a long-range periodicity. The structure of the network and its interaction with other components such as cations or H_2O determine structural properties such as density, energetical properties such as mixing enthalpy and entropy, and dynamical properties such as viscosity and diffusivity. In the case of aqueous fluids, the silica speciation (that is, the structure and relative abundance of small silica clusters) determines the solubility of SiO_2. Small clusters are directly referred to as monomer, dimers, trimers, etc. Larger clusters and networks are commonly characterized by indicating the distribution of degrees of polymerization of the individual tetrahedra (Mysen and Richet, 2005). This is expressed in Q^n-species, where n indicates the number of bridging oxygen atoms at the tetrahedra, ranging between 0 and 4. The average degree of polymerization of all tetrahedra in a system is given by the average Q^n-value.
The simplest models for the properties of a silicate system, such as its density, calculate them as separate functions of total composition, pressure and temperature, based on statistical regression in the limits of experimental data (Kress and Carmichael, 1991; Lange and Carmichael, 1987; Lange, 1994). However, the ultimate aim is to understand the relation between atomic-scale structure and macroscopically observable properties. Several chemical models predict the state of polymerization or silica speciation for a melt, glass or fluid, and derive energetical properties (including solubility) from the speciation (Hunt and Manning, 2012; Gerya et al., 2005; Felmy et al., 2001; Lin and Pelton, 1979; Romero-Serrano et al., 2010). Such models reproduce measured properties quite accurately. The reliability of predictions for PTx-conditions outside those of the "training set" used for the model is as limited as our general understanding of the structure of disordered silicate systems is.
The experimental investigation of the structure of disordered silicate materials at geologically relevant conditions is a challenging task for a number of reasons. Firstly, it requires high temperatures and eventually high pressures, achievable only in the small sample chamber volumes of multi-anvil presses or diamond-anvil cells (DAC). As mentioned above, quenched silicate glasses have commonly been used as structural analogs for silicate melts. However, it has been shown that the quench process alters for instance the speciation of H_2O in hydrous silicate melts (Nowak and Behrens, 2001). Therefore, in situ experiments are indispensable the structure of hydrous silicate melts, if not for silicate melts in general. Secondly, the number of experimental probes available for the structural investigation at in situ conditions is very limited, and cross-validation of results with complementary methods is not generally applied. Thirdly, the results of some measurement methods, especially spectroscopy probes, require substantial additional, "external" input of information and assumptions, without which the measured spectra remain rather "fingerprint" like. This includes spectral band assignment, that is, the identification of the structure that causes an observed vibrational band. Unfortunately, the reliability of band assignment is

not always equally well established, and different practices exist among experimentalists (Mysen, 2008, 2009; Malfait et al., 2007; Zakaznova-Herzog et al., 2007; Neuville et al., 2008).

Nuclear magnetic resonance (NMR) spectroscopy is one of the most powerful techniques for the structural investigation of silicate glasses. NMR probes the electronic environment selected isotopes with a nuclear magnetic spin, such as ^{1}H, ^{17}O, ^{27}Al and ^{29}Si. The NMR signal is sensitive to the nearest- and next-to-nearest-neighbor environment, the interpretation of spectra is well established, and NMR is considered a quantitative method (Chemtob et al., 2012; Kroeker and Stebbins, 2000). The major drawback of NMR is that relatively large sample quantities are required for measurements. This limits NMR measurements to ambient pressure.

Raman spectroscopy is the most commonly used technique for in situ measurements at high temperatures and pressures, for instance in the diamond anvil cell. Raman spectroscopy requires only very small sample volumes, little sample preparation, and it can be applied in the laboratory, contrary to synchrotron techniques described below. The sample area is irradiated with laser light. A small fraction of the light is inelastically scattered by optical-like vibrational modes. The energy change of the scattered light is proportional to the vibrational frequency. The Raman scattering intensity depends on the electronic polarizability changes induced by the vibration. Raman spectroscopy is more commonly used for the measurement of vibrational properties of disordered silicate materials than infrared spectroscopy (McMillan and Hofmeister, 1988).

Raman spectra reflect the quasi-optical normal mode-like vibrations of structural units of the silicate network, such as the SiO_4^{4-} tetrahedra and the Si-O-Si bridging oxygen atoms, whose vibrational frequencies change with the degree of polymerization (Mysen and Richet, 2005). Therefore, Raman spectra reflect the state of polymerization of a silicate network. The common assignment of Raman bands of silicate melts and glasses to separate degrees of polymerization has been established over decades by comparison to Raman spectra of crystalline materials of known structure and by observation of correlation between band intensities and chemical composition (Mysen and Richet, 2005; McMillan, 1984; McMillan and Hofmeister, 1988). The bands are commonly fitted by Gaussians whose center frequency is a parameter as adjustable as the height. Relative band intensities and changes in intensity are interpreted linearly as changes in concentration, with the assumption of equal Raman scattering intensity of, for instance, different Q^n-species (Mysen and Richet, 2005). There is no uniform interpretation for certain Raman bands, for example the contribution of the Si-O-Si antisymmetric stretching vibrations (Mysen, 2008). The situation is even more complicated for Raman spectra of silica species in aqueous fluids, where the Raman contribution of small silica species has not been clarified in a satisfactory way (Tossell, 2005). For these reasons, Raman spectroscopy is generally not considered as a quantitative, but semi-quantitative method. Statistical spectra evaluation tools such as principle component analysis (PCA) have been tested with promising results (Zakaznova-Herzog et al., 2007; Malfait et al., 2007, 2008). However, more development is necessary to establish Raman spectroscopy as a second fully quantitative method besides NMR.

X-ray absorption spectroscopy around the absorption edges of heavy elements can selectively probe the structural environment of those cations in silicate glasses and melts or in aqueous environment (Wilke et al., 2006). The spectrum around the absorption edge indirectly reflects the oxidation state of the cation, the number and spatial distribution of oxygen neighbors and even the next-to-nearest-neighbor structure, influenced by other cations (Wilke et al., 2006). However, the method is not commonly applied to oxygen and silicon that form the silicate network.

Diffraction of x-rays, neutrons or electrons at the atomic lattices is by far the main method of atomic structure investigation of *crystalline* materials. Unfortunately, diffraction is of limited use in disordered systems that lack periodicity. The diffraction pattern of a silicate glass or a melt is little more than a fingerprint and it is therefore not straightforward to extract structural information from it (Wilding et al., 2004, 2008, 2010).

1.3 Computational methods

Computational atomic-scale modeling has become an powerful tool to complement experimental investigation of the structure and properties of disordered silicate materials. Ab initio molecular dynamics is a technique especially suitable to account for their disordered character (Drabold, 2009; Gillan et al., 2006). It can make structural predictions at pressure and temperature conditions that are either challenging or inaccessible by experiments (Karki, 2010). Ab initio MD provides insights into the relation between structure and properties with a high degree of accuracy. Atomic-scale modeling may also help to extend the reliability of the interpretation of experimental measurements. For instance, vibrational spectroscopy techniques such as Raman spectroscopy can be supported by the calculation of vibrational properties of given silica species (Zotov and Keppler, 2000; Hunt et al., 2011).
Molecular dynamics is the computation of trajectories of a set of atoms at finite temperatures in their own potential energy fields (see below). The atomic trajectories are the evolution of positions and velocity vectors of the atomic nuclei, obtained by the numerical integration of the classical Newtonian equations of motion (Allen and Tildesley, 1987). The integration step needs to be very small with respect to the curvature of the atomic trajectories, and it is typically 1 femtosecond ($1x10^{-15}$ s). To eliminate the effect of surfaces, the model volume is considered in periodic boundary conditions. The temperature of the atoms can be controlled by various thermostat algorithms that are based on the Boltzmann distribution of kinetic energy. The pressure of a modeled volume can be controlled by barostat algorithms.
The calculation of the potential necessary for the derivation of forces on the nuclei is the computationally expensive part of the MD calculations. In the case of ab initio calculation of forces as described below, the forces are obtained from the electronic density distribution. This requires the calculation of the electronic wavefunction in its minimum energy state. However, the solution of the full Schrödinger equation is computationally too demanding for more than a few electrons. Therefore, a theoretical framework is required with a set of computational time-saving approximations sufficient to allow the calculation of the electronic wavefunction(s) for at least several hundred of electrons.
Kohn-Sham density functional theory (DFT) is a quantum mechanical modeling method for electronic structure calculation (Hohenberg and Kohn, 1964). The Kohn-Sham equations (Kohn and Sham, 1965) are based on the theorems that, firstly, properties of the electronic ground state are functionals of the electronic density distribution, and secondly, there is only one electronic density distribution that minimizes the electronic ground state energy (Hohenberg and Kohn, 1964). The many-body wavefunction is replaced by single-electron wavefunctions. The electronic energy potential is a functional of the electronic density. An initial density distribution is evolved in iterative cycles towards the energy-minimizing electronic density distribution, under the constraint of self-consistency with respect to the electronic potential energy (Marx and Hutter, 2000). The electron-electron interaction potential is split into the Coulomb's charge repulsion term (Hartree-potential) and the exchange-correlation energy functional of electronic density. Density functional theory is in principle exact, but the exact electronic density functional for the exchange-correlation energy is not known. Nowadays many different approximate parametrization exist for the exchange-correlation functional (Demichelis et al., 2010). The calculation of wavefunctions requires a basis set of functions. For calculations in periodic boundary conditions, plane-waves are especially suitable (Ashcroft and Mermin, 1976; Payne et al., 1992; Gillan et al., 2006). Only valence electrons are treated explicitly, core electrons are replaced by effective core potentials or pseudopotentials. The plane-wave pseudopotential approach to density functional theory allows for ab initio molecular dynamics of typically up to two hundred atoms and tens of picoseconds of trajectory length.

1.4 Scope of the thesis

In the present thesis, several approaches have been made to gain atomic-scale insight into structure-related properties of SiO_2-bearing glasses and fluids. In particular, a new method for the calculation

of the vibrational properties of silica species has been devised, from which the interpretation of Raman spectra may benefit. The performance of this method was tested on silica species of varying degree of polymerization in aqueous solutions and on silica species in magnesiosilicate glasses, that are considered as structural analogs to the geologically important magnesiosilicate melts. The results of these first applications of the method are presented in chapter 2 to 4.
The structure of silica-rich fluid at pressure conditions of the Earth's upper mantle is reported in Chapter 5, together with interesting structural changes occurring after temperature is lowered. At the same time, the limitations of plane-wave ab initio molecular dynamics are explored with respect to the limitations in the number of atoms (Chapter 5) and the MD trajectory durations (Chapter 6).

Chapters 2 to 4 are based on the following manuscripts :

Chapter 2:
Spiekermann, G., Steele-MacInnis, M., Schmidt, C., Jahn, S. (2012)
Vibrational mode frequencies of silica species in SiO_2-H_2O liquids and glasses from ab initio molecular dynamics
Journal of Chemical Physics, Vol. 136, pp. 154501, doi: 10.1063/1.3703667

Chapter 3:
Spiekermann, G., Steele-MacInnis, M., Kowalski, P. M., Schmidt, C., Jahn, S. (2012)
Vibrational mode frequencies of H_4SiO_4, D_4SiO_4, $H_6Si_2O_7$, and $H_6Si_3O_9$ in aqueous environment, obtained from ab initio molecular dynamics
Journal of Chemical Physics, Vol. 137, pp. 164506, doi: 10.1063/1.4761824

Chapter 4:
Spiekermann, G., Steele-MacInnis, M., Kowalski, P. M., Schmidt, C., Jahn, S. (2012)
Vibrational properties of silica species in MgO-SiO_2 glasses obtained from ab initio molecular dynamics
Chemical Geology, in press, doi: 10.1016/j.chemgeo.2012.08.020

Chapter 2

Vibrational modes of silica species in SiO_2-H_2O liquids and glasses

Published as :
Spiekermann, **G**., Steele-MacInnis, M., Schmidt, C., Jahn, S. (2012)
Vibrational mode frequencies of silica species in SiO_2-H_2O liquids and glasses from ab initio molecular dynamics
Journal of Chemical Physics, Vol. 136, pp. 154501, doi: 10.1063/1.3703667

2.1 Abstract

Vibrational spectroscopy techniques are commonly used to probe the atomic-scale structure of silica species in aqueous solution and hydrous silica glasses. However, unequivocal assignment of individual spectroscopic features to specific vibrational modes is challenging. In this contribution, we establish a connection between experimentally observed vibrational bands and ab initio molecular dynamics (MD) of silica species in solution and in hydrous silica glass. Using the mode-projection approach, we decompose the vibrations of silica species into subspectra resulting from several fundamental structural subunits: The SiO_4 tetrahedron of symmetry T_d, the bridging oxygen (BO) Si-O-Si of symmetry C_{2v}, the geminal oxygen O-Si-O of symmetry C_{2v}, the individual Si-OH stretching and the specific ethane-like symmetric stretching contribution of the $H_6Si_2O_7$ dimer. This allows us to study relevant vibrations of these subunits in any degree of polymerization, from the Q^0 monomer up to the fully polymerized Q^4 tetrahedra. Demonstrating the potential of this approach for supplementing the interpretation of experimental spectra, we compare the calculated frequencies to those extracted from experimental Raman spectra of hydrous silica glasses and silica species in aqeous solution. We discuss observed features such as the double-peaked contribution of the Q^2 tetrahedral symmetric stretch, the individual Si-OH stretching vibrations, the origin of the experimentally observed band at $970\,cm^{-1}$ and the ethane-like vibrational contribution of the $H_6Si_2O_7$ dimer at $870\,cm^{-1}$.

2.2 Introduction

Silicate-bearing aqueous fluids and water-bearing silicate melts play a fundamental role in a wide variety of geologic processes. The structural properties of silica in the presence of H_2O are also of fundamental importance in several scientific and technological areas such as zeolite research and optical glass manufacturing. For these reasons, it is important to understand how the structural properties change with compositions ranging from pure silica to hydrous silica and from dilute silica in aqueous fluids to more concentrated silica solutions.

Much of the current information on the speciation and structure of silica in fluids and in hydrous glasses has come from Raman spectroscopy in the frequency range of 400 to $1200\,cm^{-1}$, which is dominated by quasi-localized vibrational motions of the silica network (McMillan, 1984; Zotov and Keppler, 2002; Mibe et al., 2008; Mysen, 2009, 2010). A large data set of Raman spectra related to silica species in aqueous fluids at various concentrations is now available (Fortnum and Edwards, 1956; Earley et al., 1959; Alvarez and Sparks, 1985; Dutta and Shieh, 1985a,b; Hosaka and Taki, 1990; Gout et al., 1999, 2000). The hydrothermal diamond-anvil cell technique (Bassett et al., 1993), in conjunction with Raman spectroscopy, has enabled direct probing of a fluid's vibrational frequencies at high pressures and temperatures. These methods have been applied to silica in predominantly aqueous fluids (Zotov and Keppler, 2000, 2002; Mibe et al., 2008; Mysen, 2009, 2010; Hunt et al., 2011) and water-bearing silicate melts (Kohn, 2000; Mibe et al., 2008; Mysen, 2009, 2010). Changes in the structure of fused silica glass and binary Na_2O-SiO_2 glasses and melts caused by addition of water have also been investigated by Raman spectroscopy and discussed in terms of silica speciation (Stolen and Walrafen, 1976; Krol and van Lierop, 1984; McMillan and Remmele Jr., 1986; McMillan et al., 1992; Nesbitt et al., 2011; Chemtob et al., 2012).

Nevertheless, many aspects of the interpretation of Raman spectra of these materials remain uncertain. Ambiguities in the band assignments are mainly the result of the large number of potential species and their different vibrational modes that may be responsible for the observed Raman bands. The possible species include $Si(OH)_4$ monomers, low-order oligomers (dimers, trimers, etc.), more highly polymerized networks of Q^n-species (n denoting the number of oxygen atoms in one tetrahedron shared with neighboring tetrahedra) and deprotonated (charged) species (Alvarez and Sparks, 1985; Dutta and Shieh, 1985a,b; Mibe et al., 2008; Mysen, 2009, 2010; Hunt et al., 2011; Zotov and Keppler, 2002). Band

assignments are usually based either on qualitative assessment of how spectra change with changing fluid composition, and/or on the results of computational studies of small silicate molecules (see below). Among the Raman bands of silica species in aqueous fluid, the one with the most certain assignment is at about 770 cm^{-1}, which is explained by the tetrahedral symmetric stretch of a monomer (Zotov and Keppler, 2000; Hunt et al., 2011; Mysen, 2009; Dutta and Shieh, 1985b; Lasaga and Gibbs, 1988; De Almeida and O'Malley, 1991). The agreement on the vibrational frequencies of other monomer modes is fairly good. The case of the dimer is already more ambiguous. All studies agree in its contribution to a band at about 630 cm^{-1} caused by the bridging oxygen vibration, but differ in the frequency of a second band varying from 850 to 915 to 1015 cm^{-1} (Dutta and Shieh, 1985b; Lasaga and Gibbs, 1988; Zotov and Keppler, 2000; Hunt et al., 2011). Questions remain also about intermediate degrees of polymerization. For instance, the spectral contributions identified for Q^2-species differ markedly between individual studies (Malfait et al., 2007; Zakaznova-Herzog et al., 2007; Mysen, 2009, 2010). Silica rings composed of several SiO_4 tetrahedra (mostly 4 to 6) are important intermediate-range structures, not only in dry silica, but also of silica in solution (Knight et al., 2006). Their specific Raman-intense vibrational contribution consists of collective bridging oxygen motions that are referred to as "ring breathing" (Barrio et al., 1993). Their vibrational frequencies are around 600 cm^{-1} and below, a frequency region that is dominated by broad, blurred bands in Raman spectra of silica in solution. Therefore, ring structures are not commonly assigned to Raman bands of silica in aqueous solutions, although NMR measurements detect silica ring structures in these fluids (Kubicki and Sykes, 2004; Knight et al., 2006).

There are several computational methods to support the interpretation of vibrational spectra from glasses, melts or silica species in solution. We mention them briefly to motivate the approach presented in this study. They mostly aim to calculate complete Raman spectra of a model system, whereas we aim to study the distinct vibrational contributions of different silica species.

Most commonly, the methodological basis is normal mode analysis (NMA) which explicitly calculates the vibrational modes at zero Kelvin, making use of the harmonic approximation. NMA can be carried out either on clusters or bulk models in periodic boundary conditions. On the basis of the atomic displacement vectors resulting from NMA, several methods have the aim to calculate complete Raman spectra of the modelled system from the polarizability changes related to each mode. For example, the Raman-scattering cross sections are calculated fully ab initio for each vibrational mode of an isolated H_4SiO_4 or $H_3SiO_4^-$ monomer (De Almeida and O'Malley, 1991, 1993; Kubicki et al., 1995; Sefcik and Goddard, 2001), $H_6Si_2O_7$ dimers and $H_8Si_3O_{10}$ trimers (Lasaga and Gibbs, 1988; Kubicki and Sykes, 1993; Hunt et al., 2011). In practice, this approach is limited in the size of the silica clusters such that silica species beyond Q^2 have rarely been investigated with gas-phase NMA (Kubicki and Sykes, 1995). Recent advances in the perturbational treatment of polarization within the framework of density-functional theory have allowed calculation of the polarizability tensor of a system within periodic boundary conditions (Putrino and Parrinello, 2002) and its variation for finite displacements of the atoms (Umari et al., 2001). This method, applied to bulk NMA displacement vectors, allows for the calculation of Raman spectra of bulk disordered silica systems (Umari et al., 2003; Giacomazzi and Pasquarello, 2007) in very good agreement with experiment.

A classical approach to calculate polarizability changes of a system due to its vibrations is the parameterized bond-polarizability model. The bond-polarizability model is parameterized based on the polarizability of silica species in crystals (Zotov et al., 1999; Ispas et al., 2005), on ab initio polarizabilities (Liang et al., 2006; Heaton and Madden, 2008; Giacomazzi et al., 2009) or on other electro-optical models (Bornhauser and Bougeard, 2001). As the above mentioned methods, it can be applied to the atomic displacement vectors of the eigenmodes from NMA (Giacomazzi et al., 2009). However, it can also be applied to the atomic velocity vectors of a molecular dynamics trajectory (Liang et al., 2006; Bornhauser and Bougeard, 2001). Contrary to the methods above, the bond-polarizability model is suited to disentangle the Raman contributions of different silica Q^n-speciations in partially depolymerized glasses or melts (Zotov et al., 1999). However, to our knowledge, there is no bond-polarizability model for silica

species in hydrous environment.
The goal of our study is to assist the experimental assignment of Raman bands to quasi-local vibrational modes of silica species. Therefore, we need to know the frequencies of vibrational modes with presumably high Raman intensity of distinct silica species. This can not be achieved with the above mentioned methods for silica species of intermediate or high degree of polymerization: If NMA is applied to small clusters as mentioned above, the vibrational character of the modes can be evualuated visually from the atomic displacement vectors of each mode, but in bulk material, this is complicated because of the mixed character of the bulk vibrational eigenmodes.
The approach that is followed in this study is the projection of atomic velocity vectors from ab initio MD runs onto the directions of molecular normal-mode-like motions derived from theoretical spectroscopy. To our knowledge, the first application of this approach were the quasi-normal modes of the water molecule (Bopp, 1986; Kalinichev and Heinzinger, 1995). Taraskin and Elliott (1997) projected force vectors of bulk classical-potential SiO_2 onto quasi-normal modes of a tetrahedral molecule, to decompose the vibrational density into separate subspectra of different, spatially quasi-localized origin. Wilson and Madden (1996) projected atomic velocity vectors from a classical molecular dynamics run of SiO_2 onto the same quasi-normal modes and obtained the partial vibrational density by Fourier transformation of the velocity autocorrelation function. Sarnthein et al. (1997) used this projection to discover the high frequency doublet of silica to result from two different tetrahedral vibrations as opposed to result from LO-TO-splitting. Pavlatou et al. (1997) applied the same scheme to a network-forming molten salt in which the polyhedra do not form a complete network. Ribeiro et al. (1998a,b, 1999) demonstrated by mode projections in the case of $ZnCl_2$ how the idealized high-frequency quasi-local molecular modes and the idealized low-frequency propagating modes in a network forming liquid are not completely independent of one another. However, the decoupling increases with increasing bond strength (Ribeiro et al., 1999). Therefore, the high bond strength of the Si-O bond supports the applicability of local mode projections in silica systems.
Comparison of vibrational subspectra to experimental Raman spectra of silicate glasses and melts is justified by the fact that the first-order Raman scattering shifts of the photon energies directly provide the vibrational frequencies of the scattering species (see e.g. Umari et al. 2001 and Veithen et al. 2005). This contrasts with infrared spectroscopy, in which the complex response to a plane wave radiation field may cause a shift between vibrational frequencies and observed IR absorption bands (see e.g. Balan et al. 2001).
This study extends the mode-projection approach to the partially depolymerized network in the SiO_2-H_2O. We present vibrational subspectra from ab initio MD of given silica species. This is reached with the application of the mode-projection approach to molecular subunits comprising 1) silica tetrahedra of any degree of polymerization including the non-polymerized monomer as a benchmark, 2) bridging oxygen atoms to any degree of polymerization, 3) individual Si-OH stretching, 4) O-Si-O vibrations on Q^2-species, and 5) the special ethane-like case of the dimer. The frequencies of these quasi-local modes are compared to the frequencies obtained from Raman spectra and may therefore assist in band assignment. By using bulk MD and extending the mode-projection method, two important limitations of the gas-phase NMA (Hunt et al., 2011; Tossell, 2005) are overcome. Firstly, we can model any degree of polymerization. Secondly, silica species in solvation can be modeled at high temperatures (Myneni, 2002), including full anharmonicity.

2.3 Methods

Molecular dynamics simulations

For the calculation of trajectories, we used density functional theory (Kohn and Sham, 1965) in the plane wave pseudopotential approach, as implemented in the CPMD code (Marx and Hutter, 2000). The

exchange-correlation functional was PBE (Perdew et al., 1996), which performs well in hydrous silicates and which has been used in previous studies of the SiO_2-H_2O system (Pöhlmann et al., 2004; Demichelis et al., 2010). Exchange-correlation functionals of the GGA type seem to be generally superior over LDA in disordered network-forming systems (Hamann, 1996, 1997; Massobrio et al., 1999; Van Ginhoven et al., 2005). We used Martins-Troullier type pseudopotentials (Troullier and Martins, 1991). The Kohn-Sham wavefunctions were expanded at the Γ-point only with a plane wave cutoff energy of 80 Ry. Dependence of forces on k-point sampling was negligibly small (below 1%). Tests against higher cutoff energies showed that with the pseudopotentials used, all forces were within about 1% deviation from converged value. This rather high cutoff ensures high reliability of the modeled properties and structures. We used Car-Parrinello (CP) molecular dynamics (Car and Parrinello, 1985) with a ficticious electronic mass of 400 a.u. and a time step of 4 a.u. (0.097 fs). We found this setting to reproduce the Born-Oppenheimer forces very accurately even after long CP runs. Wavefunctions evolving with combinations of larger mass and time step introduce a non-negligible effect on dynamics and thus on vibrational frequencies (Grossman et al., 2004; Schwegler et al., 2004; Kuo et al., 2004). The CP fictitious kinetic energy of the wavefunctions was thermostatted. The atomic positions and velocities were recorded every 40 a.u. The stress tensor of the MD runs at 80 Ry plane-wave cutoff was unconverged with respect to the basis set and therefore required correction. We calculated this correction term from single configurations and a converged plane-wave cutoff of 140 Ry. The difference in stress tensor was added as correction to the pressure of the MD run (de Koker et al., 2008).
We performed several simulation runs, modeling different degrees of polymerization (Table 4.1). Each run was 50 ps of simulated time, and comprised the silica species plus 25-27 explicitly treated water molecules with periodic boundary conditions (except run POLY, with nominally 16 H_2O and 16 SiO_2 in a metastable single-phase state). Excluding the gas-phase runs, the total number of atoms in each of the bulk runs was between 90 and 100. The temperature was 300 K or 1000 K, and it was controlled by Nosé-Hoover-chains for each degree of freedom (Martyna et al., 1992). The runs were carried out in the NVT (canonical) ensemble, where volume and temperature were kept constant. The density was adjusted such that the average pressure at 1000 K would be close to 0.5 GPa. For a discussion of the validity of the mode-projection approach at extreme temperatures see Section 2.3.

Table 2.1: Overview of the simulation runs. The calculated pressure is about 0.5 GPa for all bulk cells.

run label	composition and species	temperature (K)	density (g/cm^3)
Monomers:			
MON-300K	H_4SiO_4 + 27 H_2O	300	0.95
MON-1000K	H_4SiO_4 + 27 H_2O	1000	0.95
Dimers:			
DIM-1000K	$H_6Si_2O_7$ + 25 H_2O	1000	1.02
DIM-GASMD-300K	$H_6Si_2O_7$	300	–
Linear trimer:			
TRIM	$H_8Si_3O_{10}$ + 23 H_2O	1000	1.09
Higher polymers:			
POLY	16 H_2O + 16 SiO_2 nominally	1000	1.88

Decomposition of the vibrational spectrum

Experimental vibrational spectra of silica species in solution, in a glass or in a melt in the frequency range between about 400 cm^{-1} and 1200 cm^{-1} contain contributions from quasi-local vibrational modes that reflect the local environment. These contributions are commonly evaluated (e.g. in Raman spectroscopy) in terms of the degree of polymerization. They arise from quasi-normal-modes of mainly two natural

structural subunits of the silicate network, the SiO_4 tetrahedron and the Si-O-Si bridging oxygen (BO) (Fig. 4.1). Through all stages of polymerization (i.e., all possible Q^n-species of a tetrahedron), the character of their vibrational motions remains the same (normal-mode-like), but the frequencies shift.
In the computational analysis of MD trajectories, the spectral density (i.e., the power spectrum) of a group of atoms is calculated from the Fourier transform of their velocity autocorrelation function (VACF)

$$F(\omega) = \int_0^{t_{max}} cos(\omega t) dt \langle v_k(t) \cdot v_k(0) \rangle, \tag{2.1}$$

where $F(\omega)$ is the spectral density and ω is the angular frequency, and chevrons indicate the ensemble average (Allen and Tildesley, 1987). The details of equation 4.1 in this contribution are $t_{max} = 1$ ps (which yields a good compromise between usage of data and sharpness of the resulting spectrum), normalisation of the VACF to unity at $t = 0$ prior to Fourier transformation and a von-Hann-window function to reduce edge effects. Finally, the spectral density $F(\omega)$ is squared and smoothed via convolution with a Gaussian of $\sigma = 20\,\mathrm{cm}^{-1}$ to facilitate the extraction of a single peak frequency.
If the complete, unprojected particle velocity vectors are used in equation 4.1, then the resulting spectral density is the complete vibrational density of states (VDOS), including translational, rotational and low-frequency long-range acoustic-like contributions (full VDOS, Fig. 3.4).
The mode-projection approach allows us to separate out each normal-mode-like quasi-local contribution of small, specific groups of atoms from the complete vibrational density. For this, the atomic velocity vectors are decomposed into different components before equation 4.1 is applied. In a first step, the atoms are grouped together according to the structural subunit of interest. In a second step, if the group consists of more than two particles, the translational movement of the group needs to be subtracted from the individual particle velocities, in order to remove non-local, low-frequency motions. This can be done by subtraction of the velocity of the center atom (the silicon in the case of the tetrahedron). Alternatively, the velocity of the center-of-mass of the group can be used. The center atom is used for subtraction throughout this study (for discussion of this choice see Section 2.3). In a third step after subtraction of the center velocity, the particle velocities are further decomposed by projection of atomic motions onto a set quasi-normal modes (QNMs) based strictly on symmetry (Pavlatou et al., 1997; Taraskin and Elliott, 1997). We follow the methods described by Pavlatou et al. (1997) and Taraskin and Elliott (1997) in decomposing the VACF of silicon-bonded oxygen atoms by projecting the vibrations onto sets of vectors representing molecular normal modes of different molecular subunits. These QNMs approximate molecular normal modes, but may differ slightly from the true normal modes in that the particle velocities are relative to the center atom.
Four main symmetries of quasi-normal-mode (QNM) decomposition are used here: 1) The SiO_4 tetrahedron with symmetry T_d, 2) O-Si-O and Si-O-Si subunit vibrations into C_{2v} (H_2O-like) QNMs, 3) the ethane-like decomposition for the case of the $H_6Si_2O_7$ dimer and 4) the individual Si-OH stretching. See Figure 4.1 and Table 4.3 for combinations of modes and geometries.

SiO_4 tetrahedral (T_d) QNMs

A tetrahedral molecule has four normal modes which are in principle all Raman active and most of which are degenerate: ν_1^{TET} (symmetric stretch, A_1), ν_3^{TET} (asymmetric stretch, F_2), ν_2^{TET} (E-bending or symmetric bending, E) and ν_4^{TET} (umbrella-bending or asymmetric bending, F_2). A sketch of the derived quasi-normal modes (QNMs) is given in Fig. 4.1, top row. The individual instantaneous velocity vectors of all four oxygen atoms of a tetrahedron i can be projected onto the ν_1^{TET} symmetric stretch QNM by

$$V^i_{\nu_1^{TET}} = \sum_{j=1}^{4} v^{||}_{i,j}, \tag{2.2}$$

where $v_{ji}^{||}$ is the magnitude of the velocity of oxygen atom j projected onto the normalized displacement vector from oxygen atom j to the silicon of tetrahedron i. Analogously, the first degenerate component of the ν_3^{TET} asymmetric stretch normal mode is described by

$$V_{\nu_3^{TET}}^{i,I} = v_{i,1}^{||} + v_{i,2}^{||} - v_{i,3}^{||} - v_{i,4}^{||}. \tag{2.3}$$

The other two degenerate modes II and III are obtained by exchanging oxygen atom 2 with oxygens 3 and 4, respectively. Other combination do not yield linearly independent modes. In the present study, the degenerate components are logged individually and averaged only after Fourier transform.
One component of the ν_2^{TET} E-bending is obtained from projection

$$\begin{aligned} V_{\nu_2^{TET}}^{i,I} = &(v_{i,1}^{\perp} - v_{i,2}^{\perp}) \cdot (\hat{r}_{i,1} - \hat{r}_{i,2}) \\ &+ (v_{i,3}^{\perp} - v_{i,4}^{\perp}) \cdot (\hat{r}_{i,3} - \hat{r}_{i,4}). \end{aligned} \tag{2.4}$$

where $v_{i,j}^{\perp}$ is the vector component of the velocity of oxygen atom j of tetrahedron i, perpendicular to Si-O, and $\hat{r}_{i,j}$ is the displacement vector from oxygen atom j to the silicon of tetrahedron i. The second component is obtained by interchanging the velocity and displacement vectors of oxygen atom 2 with those of oxygen atom 3.
One component of the ν_4^{TET} umbrella-bending can be computed from

$$V_{\nu_4^{TET}}^{i,I} = (v_{i,2}^{||} - v_{i,3}^{||} - v_{i,4}^{||}) \cdot \hat{r}_{i,1}. \tag{2.5}$$

The other two components can be obtained by interchanging the velocity and displacement vectors of oxygen atom 1 those of oxygen atom 2 and 3, respectively.

Bridging oxygen QNMs (C_{2v})

There are three structural subunits of silica with C_{2v} symmetry: 1) the Si-O-Si bridging oxygen (BO) atoms, 2) the non-bridging oxygen O-Si-O (HO-Si-OH) and 3) the bridging oxygen O-Si-O (Si-O-Si-O-Si). The first is designated by the superscript "BO", the latter two are designated by the superscript "OSiO". Here, we derive the QNM projections for the BO, and the OSiO QNMs are analogous. The C_{2v} normal modes are ν_1^{BO} symmetric stretch (A_1), ν_3^{BO} asymmetric stretch (B_2) and ν_2^{BO} bending (A_1) (Fig. 4.1, for normal modes see e.g. McMillan and Hofmeister 1988 and Taraskin and Elliott 1997).
The ν_1^{BO} symmetric stretch is, analogous to the tetrahedral case, the sum of Si-O parallel projections as

$$V_{\nu_1^{BO}}^{i} = v_{i,1}^{||} + v_{i,2}^{||}, \tag{2.6}$$

the ν_3^{BO} asymmetric stretch is

$$V_{\nu_3^{BO}}^{i} = v_{i,1}^{||} - v_{i,2}^{||}, \tag{2.7}$$

and the ν_2^{BO} bending is

$$V_{\nu_2^{BO}}^{i} = (v_{i,1}^{\perp} - v_{i,2}^{\perp}) \cdot (\hat{r}_{i,1} - \hat{r}_{i,2}). \tag{2.8}$$

Another way of decomposing the bridging-oxygen atom motions are the three orthogonal directions $v_{BO} = v_B + v_R + v_S$, related to bending, rocking and stretching (B-R-S) motions (Taraskin and Elliott, 1997). However, there are redundancies between the C_{2v} and the B-R-S concepts, only the low-frequency rocking contribution is not captured by the C_{2v} BO concept. Therefore we focus on the C_{2v} results. More vibrations of H_2O-like structural subunits are possible, like NBO-Si-NBO wagging, scissoring and twisting. However, these vibrations cannot cannot be derived from C_{2v} (H_2O-like) normal modes and do not play a role in silicates. It is not considered here and mentioned only for completeness.

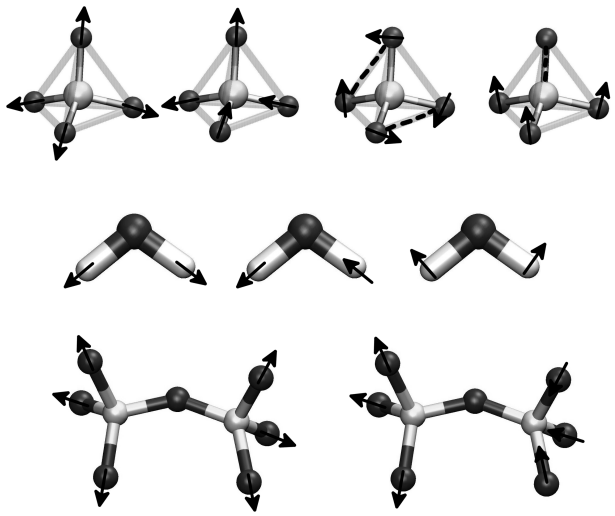

Fig. 2.1: Three sets of quasi-normal modes (QNMs) considered in this study. Top row: QNMs of a tetrahedral molecule of symmetry T_d. From left to right: ν_1^{TET} (symmetric stretch), ν_3^{TET} (asymmetric stretch), ν_2^{TET} (symmetric bending, here and elsewhere referred to as E-bending) and ν_4^{TET} (asymmetric bending, here and elsewhere referred to as umbrella-bending). Arrows indicate the velocity component of interest. Dashed lines in bending modes represent additional projection vectors where a second projection is necessary. Middle row: The C_{2v} QNMs for bridging oxygen Si-O-Si and geminal oxygen O-Si-O parts of Q^2-species. From left to right: ν_1^{BO} symmetric stretch, ν_3^{BO} asymmetric stretch and ν_2^{BO} bending. Bottom row: Two ethane-like QNMs of the Si_2O_7 dimer: ν_1^{DIM} symmetric stretch and ν_3^{DIM} asymmetric stretch. The structures were drawn using the *VMD* software package (Humphrey et al., 1996).

$H_6Si_2O_7$ dimer ethane-like QNMs

The $H_6Si_2O_7$ dimer shows vibrational motions that cannot be reduced to Q^1 tetrahedral motions alone (Tossell, 2005; Lasaga and Gibbs, 1988). There is coupling of stretching vibrations across the two tetrahedra, which is similar to two normal modes of the C_2H_6 ethane molecule. Therefore, the ethane-like ν_1^{DIM} symmetric stretch QNM is computed from the contributions of the six non-bridging oxygen atoms (see Fig. 4.1)

$$V_{\nu_1^{DIM}}^{1+2} = \sum_{j=1}^{3} v_{1,j}^{||} + \sum_{j=1}^{3} v_{2,j}^{||}, \tag{2.9}$$

and the ν_3^{DIM} asymmetric stretch is

$$V_{\nu_3^{DIM}}^{1+2} = \sum_{j=1}^{3} v_{1,j}^{||} - \sum_{j=1}^{3} v_{2,j}^{||}. \tag{2.10}$$

The individual Si-OH stretching

The Si-OH stretching of hydrogen-terminated, non-bridging oxygen atoms is recorded as the projection of instantaneous oxygen velocity onto the Si-O translation vector. It will be evaluated separately for Q^0- to Q^3-species. The hydrogen atoms are not considered explicitly, as is discussed in the following Subsection.

The validity of the silica mode-projection approach

The mode-projection approach and the above described projection sets exploit the fact that the high-frequency vibrations of the silica species in any degree of polymerization are normal-mode-like and quasi-localized. The mode-projection approach requires the choice of a center of a structure of interest for two reasons. Firstly, the translational motion of the structure as a whole needs to subtracted, as described above. Secondly, a center is needed for the construction of the displacement vectors that form the projection basis. The choice of the silicon atom as reference center of the QNM is justified because the velocity of each oxygen atom represents part of a vibration of the Si-O bond. An alternative choice, the center-of-mass of the tetrahedron, can also be used as the center of the projection. The resulting spectral density distribution is very similar (see Fig. 2.2) and the spectral density peak frequencies are almost identical. This similarity of results from different sets of projection vectors implicitly demonstrates that the tetrahedral distortion at high temperatures does not significantly affect the resulting peak frequencies. The projection on the displacement vectors of an undistorted, ideal tetrahedron would not give different results. Throughout this contribution, we use the silicon atom as reference center of the QNMs.
The QNMs are not strictly speaking orthogonal to each other. Their projections overlap. In the case of the tetrahedral QNMs, this is a result from the fact that the motion of the silicon in its oxygen cage is neglected in the QNMs (Fig. 3.4). In the case of ν_1^{BO} and ν_1^{DIM}, this results from the similarity of the atomic motions. As a consequence, the QNM projection does not exclude that some normal-mode-like motions are recorded not only by one QNM, but in a weaker degree also by a second one. In other words, the definition of our QNM projections leads to a geometrically not completely decoupled recording of atomic velocity components. This produces (artificial and usually weak) "ghost" spectral density, as in the ν_3^{TET} and ν_4^{TET} in Fig. 2.2. The exchange of the reference center from the silicon atom to the center-of-mass flips the "ghost" spectral density from ν_3^{TET} to ν_4^{TET}. This shows that the reason for this artifact is the neglect of the motion of the silicon atom, whose own "cage rattling" spectral density is shown in grey. This transfer of spectral densities does not cause complications in the interpretation of subspectra. We point to this effect wherever it occurs.
In this study, we restrict ourselves to the analysis of the vibrations of the oxygen and silicon atoms. The motions of the hydrogen atoms are not explicitly considered. This is justified as follows. It is well known that the spectroscopically important frequency range of 400-1100 cm^{-1} is dominated by the Si-O stretching and bending motions of different silica species. O-H stretching motions occur at $>3000\,cm^{-1}$ (e.g., Zotov and Keppler 2000). SiOH bending motions occur at about $1200\,cm^{-1}$ (McIntosh et al., 2011), see Chapter 3. As structural environment, the hydrogen atoms affect the frequency of Si-O vibrations implicitly. Because of low mass, the hydrogen atomic positions and their velocities do not have to be included explicitly in the analysis of the quasi-normal modes of silica structural subunits. All the effects of bonded hydrogen on the Si-O vibrations of the tetrahedral units are implicitly included in our calculations because they are included in the MD simulations. Our procedure is only very weakly sensitive to variations in the representation of the hydrogen bonding caused by different exchange-correlation functionals. At 1000 K and below, as in the present study, no Si-O bonds are broken on the timescale of our MD runs. Only occasionally, a hydrogen atoms of a hydroxy site is exchanged with one of the surrounding water molecules. This has no measureable effect on the spectral density of any QNM.
The high vibrational bandwidths in all Figures result from a combination of two effects. Firstly, the structure is disordered. This creates a bandwidth due to the damping of vibrational modes. Also, it causes a variation of the exact structural environment between every individual tetrahedron. At the stage of averaging the results for every Q^n species, this introduces band broadening. Secondly and mainly, the high width at half maximum of about $200\,cm^{-1}$ is an artifact resulting from limited ensemble averaging. Longer MD runs or larger cells would produce sharper subspectra, however, it is computationally too demanding.
Based on the comparison of power spectra from different time segments of a MD trajectory, the error of the present peak frequencies is estimated to be between $10\,cm^{-1}$ and $30\,cm^{-1}$, depending on 1) the

degree of spread of the power spectrum of a specific quasi-normal mode and 2) on the character of the vibrational motion. High-frequency, "stiff" tetrahedral stretching vibrations have a smaller error. The Si-O-Si modes have a larger error due to the additional structural degree of freedom of the Si-O-Si bending angle which significantly affects all vibrational frequencies of the bridging oxygen, see e.g. Hunt et al. (2011).

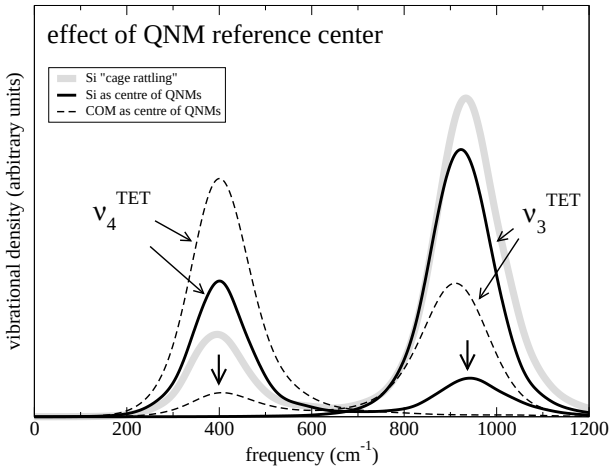

Fig. 2.2: For ν_3^{TET} and ν_4^{TET}, the difference in spectral density is demonstrated caused by using either the silicon atom or the tetrahedral center-of-mass (COM) as projection reference center. Silicon as reference center introduces an artifical high-frequency contribution to ν_4^{TET} (right arrow) as discussed in Section 2.3. The center-of-mass as reference center causes an artificial low-frequency contribution to ν_3^{TET} (left arrow). This frequency overlap results from the silicon atom "cage rattling" motions (grey). Throughout this study the silicon is used as reference center. Spectra are scaled by 1.039.

2.4 Results

There is a large amount of information resulting from the application of the different sets of QNMs to the different structural subunits. We restrict ourselves to a few stretching modes that appear to us of greatest importance for Raman spectra of dissolved silica and we give particular emphasis to those modes that are subject to some ambiguity in terms of band assignment. We present frequencies of peaks in spectral density, focusing on five major findings: 1) the neutral monomer as a benchmark of the technique, 2) the evolution of the tetrahedral stretches with increasing degree of polymerization and the special case of Q^2-species, 3) the single Si-OH stretching on tetrahedra of increasing degree of polymerization and the origin of the Raman band at 970 cm^{-1} in hydrous silica, 4) the evolution of the BO stretching modes with increasing polymerization and 5) the dimer with two unique modes.
In this Section, all depicted spectra and extracted frequencies are scaled by 1.039 to account for the systematic error of the ab initio method used here. In Section 2.5 the derivation of this scaling factor is discussed. We evaluate the spectral densities in terms of their peak frequencies. In Table 4.4 both scaled and unscaled spectral density peak frequencies of stretching QNMs are listed.

The tetrahedral QNMs of the H_4SiO_4 monomer

The H_4SiO_4 monomer is a test case for the mode-projection approach, because a several computational studies have calculated the NMA frequencies to which our results can be compared (see Section 5.2).

Table 2.2: Quasi-normal modes (QNMs) discussed in this study. Other QNMs were also derived, but are not considered further because they are less relevant to Raman band assigments in experimental studies.

Mode:	applied to:	abbreviation:	in Figure:
single oxygen mode:			
single Si-O stretch	any oxygen atom	–	2.7
tetrahedral QNMs (T_d):			
symmetric stretch (A_1)	any Q^n-species	ν_1^{TET}	3.4,2.4,2.6
asymmetric stretch (F_2)	any Q^n-species	ν_3^{TET}	3.4,2.5
E-bending (E)	any Q^n-species	ν_2^{TET}	3.4
umbrella-bending (F_2)	any Q^n-species	ν_4^{TET}	3.4
BO QNMs (H_2O-like, C_{2v}):			
Si-O-Si symmetric stretch (A_1)	any bridging oxygen	ν_1^{BO}	2.8
Si-O-Si asymmetric stretch (B_2)	any bridging oxygen	ν_3^{BO}	2.9
Si-O-Si bending (A_1)	any bridging oxygen	ν_2^{BO}	–
Q^2 BO and NBO (C_{2v}):			
O-Si-O symmetric stretch (A_1)	Q^2 BO/NBO pair	ν_1^{OSiO}	2.6
O-Si-O asymmetric stretch (B_2)	Q^2 BO/NBO pair	ν_3^{OSiO}	2.6
O-Si-O bending (A_1)	Q^2 BO/NBO pair	ν_2^{OSiO}	–
ethane-like QNMs:			
symmetric stretch (A_1)	dimer	ν_1^{DIM}	2.10
asymmetric stretch (B_2)	dimer	ν_3^{DIM}	2.10

In Fig. 3.4, the spectral densities of the four tetrahedral QNMs of the H_4SiO_4 monomer are shown for 300 K and 1000 K. All QNMs show a weak decreasing trend in frequency upon increasing temperature, as is expected from theory and experiment (see e.g. Zotov and Keppler 2000). The ν_1^{TET} is at 774 cm^{-1} for 300 K and at 762 cm^{-1} for 1000 K. These frequencies match experimental ones very closely because both frequencies were used for the derivation of the scaling factor of 1.039 (Section 2.5). At 1000 K, ν_3^{TET} is at 920 cm^{-1}, ν_2^{TET} at 291 cm^{-1} and ν_4^{TET} at 405 cm^{-1}. The weak high-frequency peak of ν_4^{TET} at about 935 cm^{-1} is an artifical contribution as discussed in Section 2.3. Also in Fig. 3.4, we plot literature data for comparison. These explicitly calculated frequencies from NMA represent very Raman intense normal modes of the monomer.

Tetrahedral symmetric stretching of higher Q^n-species

Higher-order silicate polymers exhibit a polymerization-driven systematic trend in the frequencies of most vibrational modes, which is reflected in the QNM results. This shift is especially important for the very Raman intense ν_1^{TET} mode. The spectral density peak frequency shifts from 761 cm^{-1} (Q^0) via 793 cm^{-1} (Q^1) and 1103 cm^{-1} (Q^3) to 1149 cm^{-1} (Q^4) (Fig. 2.4, inset in Fig. 2.5 and Table 4.4). The broad contribution of the Q^2 ν_1^{TET} will be discussed below. All calculated spectra of Q^n-species shown in Fig. 2.4 are averaged over several tetrahedra of the same degree of polymerization, namely, 2 tetrahedra for Q^0, 2 for Q^1, 6 each for Q^2 and Q^3, and 3 tetrahedra for Q^4. This improves the counting statistics of the peak shapes and positions.

The ν_3^{TET} also possesses a high Raman intensity in the case of the H_4SiO_4, as the literature data in Fig. 3.4 show. It also shows a polymerization-driven shift to higher frequencies. The ν_3^{TET} peak frequency of Q^0 is 920 cm^{-1}, for Q^1 942 cm^{-1}, for Q^2 970 cm^{-1}, for Q^3 1015 cm^{-1} and for Q^4 it is 1062 cm^{-1} (Fig. 2.5 and inset in Fig. 2.5). The latter value is in excellent agreement to the intense experimental band at 1060 cm^{-1} in pure dry silica glass which originates from the Q^4 ν_3^{TET} (Sarnthein et al., 1997). There is a frequency crossover of ν_1^{TET} and ν_3^{TET} with increasing polymerization (inset in Fig. 2.5). The ν_3^{TET} has a higher peak frequency than the ν_1^{TET} for low polymerized Q^0- and Q^1-species, but lower a lower peak

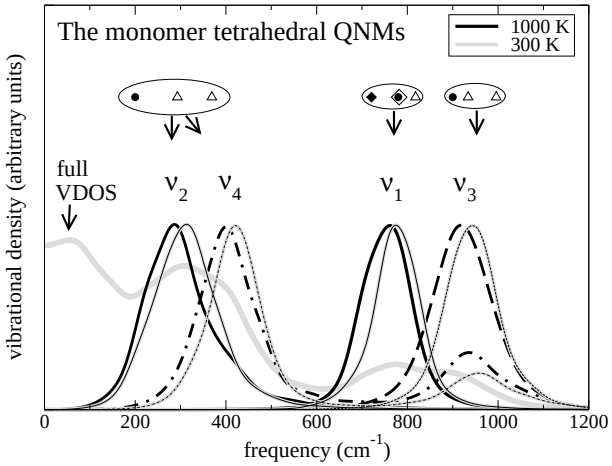

Fig. 2.3: Spectral density of the four tetrahedral QNMs of the silicate monomer (1000 K and 300 K). For QNM abbreviations see Table 4.3. The full VDOS is plotted for comparison. All spectral densities are scaled by 1.039 (see Section 2.5). Symbols represent literature data of monomer vibrational frequencies with Raman activity higher than 1% of that of the ν_1^{TET} symmetric stretch near 770 cm^{-1}. Empty diamond: Zotov and Keppler (2000) (bond polarizability model). Filled diamond: Tossell (2005) (MP2). Circles: Lasaga and Gibbs (1988) (Hartree-Fock). Triangles: De Almeida and O'Malley (1991) (Hartree-Fock).

frequency than the ν_1^{TET} for higher polymerized Q^3- and Q^4-species (Figs. 2.4 and 2.5). The Q^2 shows a double character.

The double character of Q^2 is reflected in its ν_1^{TET} double peak at 888 cm^{-1} and 1081 cm^{-1} (Fig. 2.6). The third ν_1^{TET} contribution at 701 cm^{-1} is an artifact of ν_1^{BO} as discussed in Section 2.3. All six Q^2-species used in the averaging show almost identical behavior. The two peaks of the Q^2 ν_1^{TET} can be explained by the motions of the smaller O-Si-O subunits (Fig. 2.6). The 888 cm^{-1} contribution arises from the ν_1^{OSiO} of the non-bridging NBO-Si-NBO, the 1081 cm^{-1} contribution stems from the analogous bridging oxygen BO-Si-BO ν_1^{OSiO}.

Single Si-OH stretching

The spectral densities of single non-bridging Si-OH stretching are shown for several Q^n-species in Fig. 2.7. Almost independent of the degree of polymerization of the respective tetrahedron, the peak frequency is between 915 cm^{-1} for Q^0-species and 925 cm^{-1} for Q^3-species (Table 4.4). This finding is important for hydrous silica glasses, because commonly a band at 970 cm^{-1} has been assigned to Si-OH stretching (Stolen and Walrafen, 1976; Krol and van Lierop, 1984; McMillan and Remmele Jr., 1986).

The bridging oxygen QNMs

The different degrees of polymerization of bridging oxygen (BO) atoms are described by the Q^n-Q^m notation which indicates the degree of polymerization of the adjacent two tetrahedra. The Q^n-Q^m-specific subspectra in Figures 2.8 and 2.9 are mostly averages over several BO atoms. The number of BO atoms used for every Q^n-Q^m combination are 1 for Q^1-Q^1, 2 for Q^1-Q^2, 7 for Q^2-Q^3, 5 for Q^2-Q^4, 3 for Q^3-Q^3, 5 for Q^3-Q^4 and 1 for Q^4-Q^4. The Si-O-Si ν_1^{BO} peak frequency in Fig. 2.8 is at about 620 cm^{-1} for the lowest possible degree of polymerization (i.e. Q^1-Q^1). For Q^1-Q^2 it is at about 680 cm^{-1}. For all higher polymerized bridging oxygens the peak frequency is around 780 cm^{-1}. The second peak in the spectral density of Q^1-Q^1 at 880 cm^{-1} (and to a lesser extent, for Q^1-Q^2) is an artifact as discussed in Section 2.3.

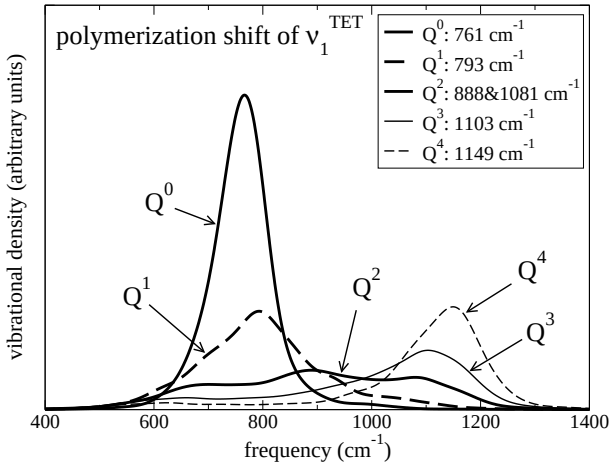

Fig. 2.4: The polymerization-driven ν_1^{TET} frequency shift from 762 cm^{-1} for Q^0-species to 1149 cm^{-1} for Q^4-species. Spectral densities are scaled by 1.039.

The Si-O-Si ν_3^{BO} is centered between 1050 cm^{-1} and 1060 cm^{-1}, with only a slight trend towards higher frequencies upon increasing polymerization (Fig. 2.9). This study focuses on the high-frequency silica stretching modes, therefore we do not consider the ν_2^{BO} bending here.

The $H_6Si_2O_7$ dimer QNMs

Two runs have been carried out for the dimer, changing temperature and bulk/gas-phase (Table 4.1). The ν_1^{TET} of the two individual Q^1 tetrahedra is at 793 cm^{-1}, as has been discussed in Section 2.4. The ethane-like ν_1^{DIM} shows a relatively narrow peak at about 870 cm^{-1} (Fig. 2.10). The same mode in the gas-phase run at 300 K was observed at 845 cm^{-1} (Table 4.4). The peak of the ν_3^{DIM} is at 783 cm^{-1} at 1000 K and at 785 cm^{-1} at 300 K. Counter-intuitively, the ν_1^{DIM} is higher in frequency than the ν_3^{DIM}.

2.5 Discussion

Benchmarking and scaling: The H_4SiO_4 monomer

The ν_1^{TET} is by far the most Raman-intense mode of the silicic-acid monomer and its assignment is well established (Fig. 2.11 and citations in Section 5.2). Therefore, we use this mode for the derivation of a scaling factor to account for the systematic error of the ab initio calculations used here and to align the calculated frequencies with the values measured in experiment (Tossell, 2005). The frequency agreement of our results of about 745 cm^{-1} (300 K) and 733 cm^{-1} (1000 K) to published NMA results (Tossell, 2005; McIntosh et al., 2011; De Almeida and O'Malley, 1991, 1993; Kubicki et al., 1995; Sefcik and Goddard, 2001; Zotov and Keppler, 2000; Lasaga and Gibbs, 1988) is good (Fig. 3.4 and Table 4.4). The experimental frequency of the ν_1^{TET} occurs at about 775$\pm$10 cm^{-1} (Schmidt and Watenphul, 2010). It is weakly temperature dependent: 770 cm^{-1} at 300 K and 765 cm^{-1} at 1000 K (Zotov and Keppler, 2000). From these two experimental frequencies and the results of the monomer MD runs, the frequency ratios give scaling factors of 1.044 and 1.033 for 300 K and 1000 K (Table 4.4). These factors are in good agreement to common frequency scaling factors (Tossell, 2005). We used the averaged scaling factor of 1.039 throughout this study.

For benchmarking, Figure 3.4 shows computed frequencies of modes with high Raman activity from the gas-phase cluster modeling literature (Zotov and Keppler, 2000; Lasaga and Gibbs, 1988; De Almeida and O'Malley, 1991). These modes have a Raman intensity of at least 1% of that of the most

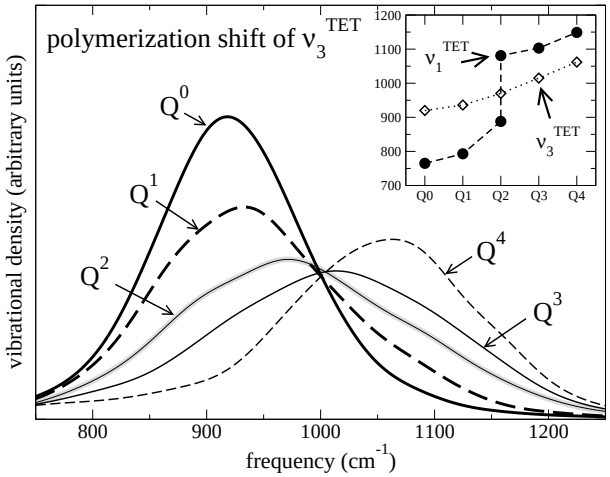

Fig. 2.5: The polymerization-driven frequency shift of the ν_3^{TET} asymmetric stretch from Q^0- to Q^4-species. Spectral densities are scaled by 1.039. Inset: The frequency shift of ν_1^{TET} and ν_3^{TET} with increasing Q^n-speciation. Note the cross-over of the ν_3^{TET} and ν_1^{TET} at Q^2-species.

intense mode. These results were calculated using various reliable techniques up to Hartree-Fock level. The scatter between these results represents differences produced by different theoretical approaches (Hartree-Fock, MP2 and classical potential; Fig. 3.4). The spectral densities of the four tetrahedral QNMs used here covers the Raman scattering vibrations of the complete H_4SiO_4 monomer in the spectral region of interest up to 1200 cm^{-1} (Fig. 3.4). This gives us confidence in the mode-projected VACF approach: The application of tetrahedral QNMs to the H_4SiO_4 monomer produces spectral density peaks in all the frequency regions where there are known Raman-spectroscopically important modes of the H_4SiO_4 monomer (Fig. 3.4).

Comparison to experimental results

Because the aim of our study is to assist band assignment, we show our results in comparison to the work of Zotov and Keppler (2000) and Mysen and Virgo (1986) (Fig. 2.11). The most important QNM peak frequency results are indicated. These are likely the most Raman intense modes in the frequency range between 600 cm^{-1} and 1200 cm^{-1}, but we do not claim completeness. However, our findings have the potential to explain important features of Raman spectra of the system SiO_2-H_2O.

Behavior of ν_1^{TET} and ν_3^{TET} with increasing polymerization

The ν_1^{TET} is a strong Raman scatterer in silica species. From all possible Q^n-species together, it is probably responsible for the largest part of Raman intensity between 770 cm^{-1} and 1150 cm^{-1} (see e.g. McMillan 1984, also Fig. 2.11). Its vibrational contribution remains localized in frequency range during increasing polymerization (Fig. 2.4). The Q^0 ν_1^{TET} has been used by us to derive the scaling factor of 1.039 (Section 2.5, Table 4.4). The Q^1 ν_1^{TET} is at 793 cm^{-1}. This is very close to the frequency of Q^0. Experimental studies assign a band centered at 850 cm^{-1} (Fig. 2.11) to Q^1-species (Mysen 2009, for similar assignment in potassium silicate melt see Malfait et al. 2007). This apparent contradiction is resolved below (Section 2.5). However, the Q^1 ν_1^{TET} at about 793 cm^{-1} points to an asymmetry of the Q^0 770 cm^{-1} band which can be observed in Figure 2.11 (see also Dutta and Shieh 1985b and Zotov and Keppler 2000). Q^3- and Q^4-species have been assigned to Raman intensity between 1100 cm^{-1} to 1150 cm^{-1} in silica glass or sodium silicate glasses (McMillan, 1984; Malfait et al., 2008, 2007; Mysen, 2009, 2010). Our results of 1103 cm^{-1} for Q^3 and 1149 cm^{-1} for Q^4 are in good agreement with these

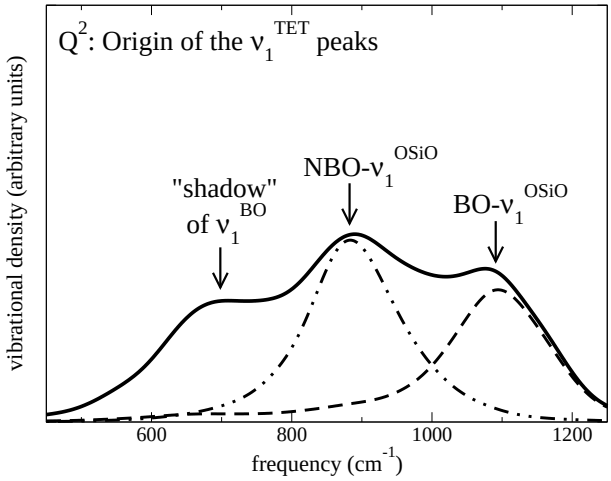

Fig. 2.6: The two high-frequency peaks of the Q^2 ν_1^{TET} originates from the vibrations of the O-Si-O units of the Q^2-species, namely the non-bridging NBO-Si-NBO ν_1^{OSiO} and the bridging oxygen BO-Si-BO ν_1^{OSiO}. The peak at 701 cm^{-1} is an artifact due to transmission of ν_1^{BO} vibrations into Q^2 ν_1^{TET}, as discussed in Section 2.3. All spectra are scaled by 1.039.

assignments. The frequency difference between the high-frequency peak of Q^2 at 1081 cm^{-1} and the Q^3 at 1103 cm^{-1} is quite small, which will make their distinction in experiment difficult, unless the lower-frequency peak of Q^2 at 888 cm^{-1} is also taken into consideration (Table 4.4). In Figure 2.11, the extension of the high-frequency shoulder to 1100 cm^{-1} and beyond with increasing silica content can be explained by an increase in Q^2-species.

The spectral density of the ν_1^{TET} of polymerized tetrahedra is narrowest when oxygen atoms of the Q^n-species are either all non-bridging (Q^0) or when they are all bridging (Q^4), but wider for intermediate Q^n-species. The Q^2-species show the broadest spectral density (Fig. 2.4), with two distinct peaks (Fig. 2.6). This double peak and its intermediate character between low and high degree of polymerization (inset in Fig. 2.5) may be the reason for the still debated assignment of peaks to Q^2-species (Malfait et al., 2007; Mysen, 2009). In Raman spectra of a potassium silicate melt, Malfait et al. (2007) assigned two peaks at 920 cm^{-1} and 1070 cm^{-1} to Q^2-species, based on correlated intensities. Our two peaks at 888 cm^{-1} and 1081 cm^{-1} are in good agreement with this. These results 1) give further evidence for the observation that Q^2-species produce a double peak (Malfait et al., 2007; Zotov et al., 1999), and 2) show that the two experimentally found Q^2 band are probably caused by a double peak of the ν_1^{TET}.

Our result of the ν_3^{TET} of Q^0-species at 920 cm^{-1} is in close agreement to an experimental band at 925 cm^{-1} in the lowest silica concentration (Fig. 2.11). The relative significance of this band decreases with increasing silica concentration. However, this may be a result of increasing Raman intensity around that band rather than a real decrease of the 925 cm^{-1} band (Fig. 2.11). A direct tracing of the ν_3^{TET} with increasing degree of polymerization is not possible in the experimental spectra, because it is too weak.

Single non-bridging oxygen Si-OH stretching and the origin of the 970 cm^{-1} band in hydrous silica

In hydrous silica glass, there is a band at 970 cm^{-1}, which is usually interpreted as arising from a defect structure and commonly assigned to Si-OH stretching of Q^3-species (Stolen and Walrafen, 1976; Krol and van Lierop, 1984; McMillan and Remmele Jr., 1986). A weak band at 910-915 cm^{-1} is also present (Stolen and Walrafen, 1976; Krol and van Lierop, 1984; McMillan and Remmele Jr., 1986), that has been assigned only once, to an SiOH vibration of two geminal silanol groups (i.e., to Q^2-species) (Krol and

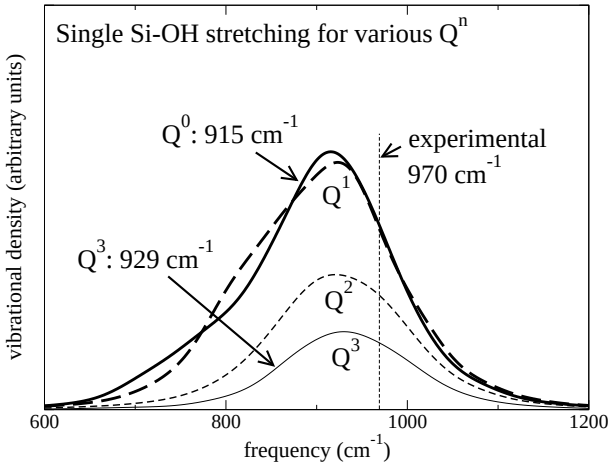

Fig. 2.7: The single non-bridging oxygen Si-OH stretching for different degrees of polymerization of the tetrahedron. Spectra are scaled by 1.039.

van Lierop, 1984). Our results show that the individual SiOH stretching is at about 930 cm^{-1} for Q^3 and at about 920 cm^{-1} for Q^2 (Table 4.4). This suggests that the individual SiOH stretching vibrations may not be the reason for the band at 970 cm^{-1}. Also, the Q^3 ν_1^{TET} at about 1100 cm^{-1} and ν_3^{TET} at about 1015 cm^{-1} are not near the 970 cm^{-1} band. Therefore, we suggest that they are also less likely the reason for this band. NMR is a sensitive probe for Q^n-species in silica glass (Farnan et al., 1987; Kubicki and Sykes, 2004; Chemtob et al., 2012). It has been shown by a recent NMR study that, besides Q^3-species, also a significant amount of Q^2-species can be present in hydrous silica glass (Chemtob et al., 2012). We observe the ν_3^{TET} of Q^2-species at 970 cm^{-1} (Table 4.4). However, the origin of the 970 cm^{-1} band cannot be decided on the basis of this point, and further investigation is needed.

The BO stretching vibrations

The ν_1^{BO} is strongly dependent on the degree of polymerization of the two adjacent tetrahedra (Fig. 2.8). The weakest state of polymerization of a BO is Q^1-Q^1, whose ν_1^{BO} shows a peak frequency at 620 cm^{-1}. The second peak of the Q^1-Q^1 at about 845 cm^{-1} is an artifact of the ν_1^{DIM} as discussed in Section 2.3. There is a polymerization-driven shift from 618 cm^{-1} to peaks between 780 cm^{-1} and 830 cm^{-1} (Fig. 2.9). These results agree with several experimental observations. Firstly, the experimental peaks around 600 cm^{-1} vanish with increasing polymerization. In pure SiO_2, there is only a peak in that frequency range resulting from small silica rings (McMillan, 1984; Ivanda et al., 2003; Giacomazzi and Pasquarello, 2007; Umari et al., 2003). Secondly, in several experimental studies the peak at about 630 cm^{-1} was interpreted as resulting from Si-O-Si vibrations of weakly polymerized species (Mysen, 2009; Dutta and Shieh, 1985b; McMillan and Remmele Jr., 1986). The Raman band around 800 cm^{-1} present in pure silica may rather be explained by the bridging oxygen asymmetric stretch than tetrahedral stretching (Ivanda et al., 2003). Here again, the mode-projection technique gives a consistent picture of the evolution of frequencies with changing molecular structure.

The frequency of the peak center of ν_3^{BO} is at about 1070 cm^{-1} which is in good agreement to experimental observations (Mysen, 2009, 2010). It falls into the frequency region of the Q^3 and Q^4 ν_1^{TET}. Contrary to ν_1^{BO}, the ν_3^{BO} does not show significant shifts with higher degree of polymerization. The ν_3^{BO} has a high Raman intensity on the case of the $H_6Si_2O_7$ dimer. It is likely that this mode keeps an important Raman intensity with increasing degree of polymerization. The presence of this mode in the same frequency range of 1100 cm^{-1} to 1150 cm^{-1}, where most commonly only the Q^3- and Q^4-species

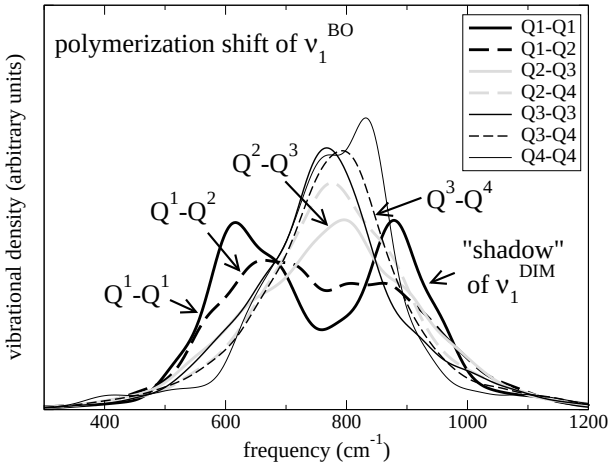

Fig. 2.8: The bridging oxygen ν_1^{BO} for various degrees of polymerization. All spectra are scaled by 1.039. Note the frequency shift with increasing polymerization from 620 cm^{-1} for Q^1-Q^1 to about 780 cm^{-1} for Q^1-Q^1 and even higher degrees of polymerization.

are fitted, could have an important consequence: The degree of polymerization could be overestimated if all Raman intensity in this frequency region is explained by Q^3- and Q^4-species, but not by ν_3^{BO} as well (see also Chapter 4).
The ν_3^{BO} and the Q^4 ν_3^{TET} peak frequencies are both between 1060 cm^{-1} and 1070 cm^{-1} (Figs. 2.9 and 2.5). The ν_3^{BO} peak frequency is polymerization-independent, whereas the ν_3^{TET} shifts with increasing polymerization. It reaches the ν_3^{BO} peak frequency of about 1060 cm^{-1} in the case of Q^4-species, when every oxygen is a bridging oxygen. Therefore, the 1060 cm^{-1} band in pure silica, which has been assigned to ν_3^{TET} (Sarnthein et al., 1997), can as well be assigned to ν_3^{BO}.

The $H_6Si_2O_7$ dimer

The Q^1-species in aqueous fluid have been assigned to an experimentally observed peak at 850 cm^{-1} (McMillan, 1984; Mysen, 2009). Our results are in agreement with this assignment, and furthermore the calculations provide insight into which specific molecular vibrations are responsible for this band. The 850 cm^{-1} band does not appear to result from ν_1^{TET}. We observe the ν_1^{TET} of the Q^1 (Table 4.4) at about 790 cm^{-1}, and the reproducibility across several simulations lends confidence to this value. The two Q^1 of a dimer do show an ethane-like coupling (ν_1^{DIM}, Table 4.4) at about 870 cm^{-1} at 1000 K and at about 850 cm^{-1} in the gas-phase at 300 K. This is in good agreement with hybrid DFT calculations that predict very similar frequencies (Tossell, 2005). Thus, an experimentally observed peak at 850 cm^{-1} can be explained by the ethane-like ν_1^{DIM} mode of the dimer. A more detailed study on the vibrational properties of the dimer is in preparation.

2.6 Conclusions

In this study, new evidence is given to support common band assignments of silica in aqueous fluids and hydrous glasses: 1) Q^3 and Q^4 ν_1^{TET} have peaks around 1100 cm^{-1} and 1150 cm^{-1}, respectively; 2) the contribution of bridging oxygen ν_3^{BO} to bands with frequencies around 1070 cm^{-1}; and 3) the ν_1^{BO} in weakly polymerized species shows a peak around 600 cm^{-1}.
We find evidence for the assignment of several spectral features that have been hitherto ambiguous: 1) the Q^1 ν_1^{TET} shows a peak frequency of about 790 cm^{-1} which in experiments might be hidden by the strong

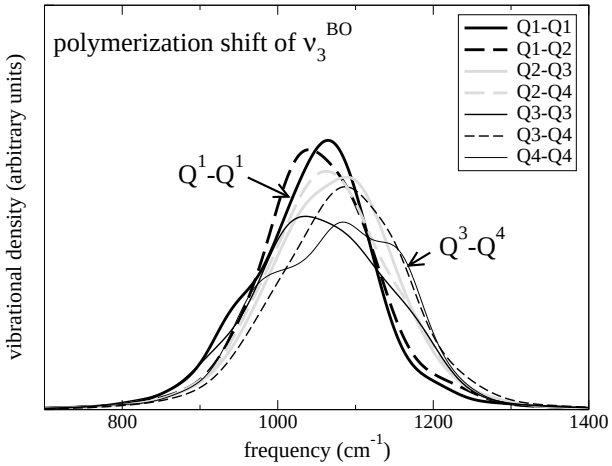

Fig. 2.9: The bridging oxygen ν_3^{BO} for various degrees of polymerization. All spectra are scaled by 1.039.

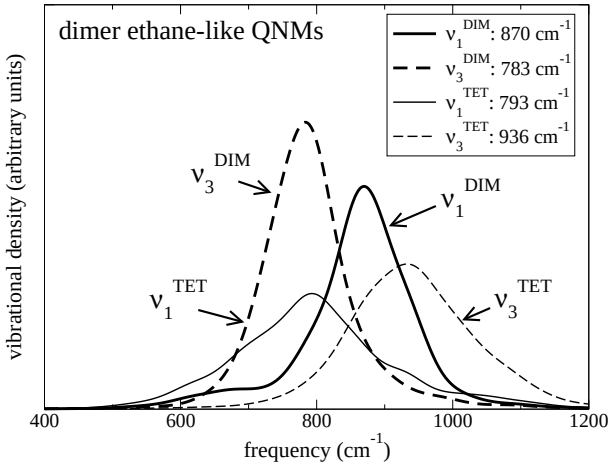

Fig. 2.10: The dimer ethane-like ν_1^{DIM} and ν_3^{DIM}, and two tetrahedral QNMs for comparison. Spectra are scaled by 1.039.

770 cm^{-1} band of the Q^0-species; 2) the Q^2 ν_1^{TET} exhibits a double-cusp band caused by its intermediate character between low and high degree of polymerization; 3) the dimer shows a peak between 870 cm^{-1} and 850 cm^{-1} resulting from the ethane-like ν_1^{DIM}, 3) the ν_1^{BO} shows a peak around 600 cm^{-1} only in the case of a degree of polymerization less than Q^2-Q^3, and 4) the 970 cm^{-1} band may possibly not result from individual Si-OH stretching (which we find at about 920 cm^{-1}).

The technique used here is comprehensive, i.e. any species can be considered, including charged species. It can be applied to other subsets of quasi-normal modes, e.g. octahedral ones, or larger structures such as silica rings. In doing so, it may provide insight into the origin of vibrational bands in pure silica glass, whose Raman spectrum is quite different from Raman spectra of polymerized silica species in solutions and glasses. Other, non-localized modes could be considered as well. The precision of this technique is only limited by the length of the molecular dynamics runs and the accuracy of the underlying framework of potential energy calculation. The species- and mode-selective subspectra presented here can be a reliable basis for the application of experimental analysis techniques like the principal component analysis.

Table 2.3: Overview over the frequency results of tetrahedral and dimer stretching QNMs. The two monomer symmetric stretch results have been used to derive an averaged scaling factor (SF) of 1.039. For mode abbreviations see Table 4.3. The uncertainty is estimated to be about 10 to 30 cm^{-1} (see Section 2.3)

species, mode and run:	see Figure:	unscaled freq.: (cm^{-1})	scaled freq.: (cm^{-1})	annotations:
ν_1^{TET}**:**				
Q^0, from MON-1000K	3.4	733	765 (SF 1.044)	Exp: 765, Zotov&Keppler 2002
Q^0, from MON-300K		745	770 (SF 1.033)	Exp: 770, Zotov&Keppler 2002
Q^1, from DIM-1000K and TRIM	2.4,2.10	763	793	close to Q^0 ν_1^{TET}
Q^2, from POLY (av of 6)	2.6	855+1040	888+1081	
Q^3, from POLY (av of 3)	2.4	1062	1103	
Q^4, from run POLY (1 only)	2.4	1106	1149	
ν_3^{TET}**:**				
Q^0, from MON-1000K	3.4	885	920	
Q^0, from MON-300K	3.4	907	942	
Q^1, from DIM-1000K and TRIM	2.5,2.10	901	936	
Q^2, from POLY (av of 6)	2.5	934	970	
Q^3, from POLY (av of 6)	2.5	977	1015	
Q^4, from POLY (av of 3)	2.5	1023	1062	
single NBO Si-OH stretch:				
Q^0 (Q^3)	2.7	881 (894)	915 (929)	
Dimer QNMs:				
ν_1^{DIM}, 1000 K (gas at 300 K)	2.10	837 (813)	870 (845)	(Tossell, 2005)
ν_3^{DIM}, 1000 K (gas at 300 K)	2.10	754 (756)	783 (785)	

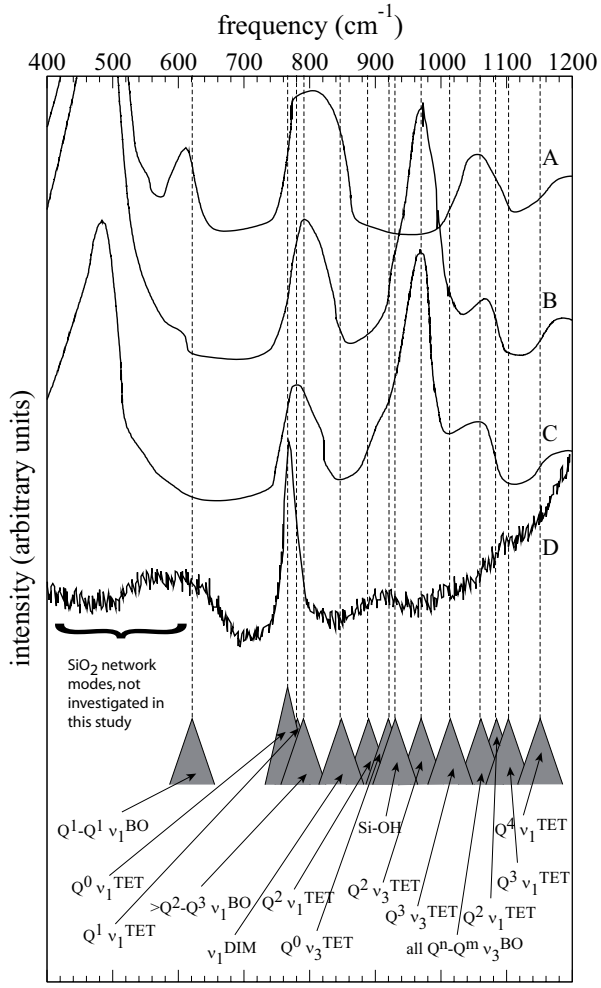

Fig. 2.11: Upper part: Four experimental Raman spectra of the system SiO_2-H_2O. Lower part: Selected species- and mode-specific frequencies determined in the present study, scaled by 1.039. Spectrum (A): pure SiO_2 glass (Mysen and Virgo, 1986). Spectrum (B) and (C): SiO_2 with 10wt% H_2O and 5wt% H_2O, respectively (Mysen and Virgo, 1986). Spectrum (D): Silica in aqueous solution at 900 ∘C and 1.4 GPa (Zotov and Keppler, 2000). Note that the intensity shoulder from about 1000 cm^{-1} is due to the diamond anvil cell.

Chapter 3

Vibrational mode frequencies of small silica species in aqueous environment

Published in a similar version as :
Spiekermann, **G**., Steele-MacInnis, M., Kowalski, P. M., Schmidt, C., Jahn, S. (2012)
Vibrational mode frequencies of H_4SiO_4, D_4SiO_4, $H_6Si_2O_7$, and $H_6Si_3O_9$ in aqueous environment, obtained from ab initio molecular dynamics
Journal of Chemical Physics, Vol. 137, pp. 164506, doi: 10.1063/1.4761824

3.1 Abstract

We report the vibrational properties of H_4SiO_4, D_4SiO_4, $H_6Si_2O_7$ and $H_6Si_3O_9$ in aqueous solution at 300 K and 1000 K, obtained from the combination of ab initio molecular dynamics (MD) and a mode-decomposition approach. This combination yields vibrational subspectra for selected vibrational modes at finite temperatures. We also performed NMA on numerous configurations from the same MD run to sample the effect of the variable molecular environment. We found good agreement between both approaches. The strongest impact of temperature is on the SiOH bending mode δSiOH which is at about 1145 cm^{-1} in solution at 300 K, opposed to about 930 cm^{-1} in solution at 1000 K. The frequency of the δSiOH vibration depends on environment, shifting from 1145 cm^{-1} in solution to about 845 cm^{-1} in the gas-phase. We found both in the mode-decomposition approach and in multiple-configuration NMA that the $H_6Si_2O_7$ dimer shows a vibrational mode at about 790 cm^{-1} which we consider to be responsible for a hitherto unexplained shoulder of the monomer Raman band at 770 cm^{-1} in dilute silica solutions. Our results demonstrate the importance of temperature and environment in calculations that aim to support interpretation of experimental Raman spectra of dissolved silica.

3.2 Introduction

The speciation and solubility of silica in aqueous solution is of interest in geosciences, zeolite research and other research areas (Feuston and Garofalini, 1990; Pereira et al., 1998; Sefcik and Goddard, 2001; Tossell, 2005; Gerya et al., 2005; Trinh et al., 2006; Mora-Fonz et al., 2007; Newton and Manning, 2008; Trinh et al., 2009; Dolejš and Manning, 2010). Raman spectroscopy is a sensitive probe of the silica speciation, also at elevated pressures and temperatures, where other techniques like nuclear magnetic resonance (NMR) cannot be applied. Therefore, much of the currently available information on the structure of silica in fluids has come from Raman vibrational spectroscopy (Fortnum and Edwards, 1956; Earley et al., 1959; Alvarez and Sparks, 1985; Dutta and Shieh, 1985a,b; Hosaka and Taki, 1990; Gout et al., 1999, 2000; Zotov and Keppler, 2002; McIntosh et al., 2011; Hunt et al., 2011). Assignments of individual Raman bands of silica in dilute aqueous solution requires precise knowledge of the species- and mode-specific vibrational frequencies. However, at present the species- and mode-specific frequencies are only partly known, such that interpretations of Raman spectra are generally qualitative to semi-quantitative. There is general agreement that the frequency range of 200 to 1200 cm^{-1} reflects quasi-localized, normal-mode-like vibrations of the Si-O_H bonds in hydrous silica species (where the subscript H indicates hydrogen bound to the oxygen participating in the vibration of the Si-O- bond). In Raman studies of silica-bearing systems, mostly bands in the high-frequency part above 600 cm^{-1} are generally interpreted structurally (McMillan, 1984; Mysen and Richet, 2005). These bands mostly arise from Si-O_H stretching vibrations of SiO_4^{4-} tetrahedra and from Si-O-Si bridging oxygen (BO) atoms and are mostly sharper than the Raman bands at lower wavenumbers which arise from bending vibrations.
Normal mode analysis (NMA) is the most frequently used computational method to assist experimental band assignment. Vibrational frequencies are calculated explicitly at zero Kelvin in the harmonic approximation. The environment is commonly neglected (Lasaga and Gibbs, 1988; Zotov and Keppler, 2000; De Almeida and O'Malley, 1991). In recent years there has been a growing effort to develop methods to include the effects of molecular environment either implicitly or explicitly (Tomasi et al., 2005; Hunt et al., 2011; McIntosh et al., 2011), because the structural environment of a molecule in solution can significantly influence the frequencies of the vibrational modes of the molecule. For example, compared to gas-phase NMA, the implicit inclusion of an aqueous environment in NMA lowers the frequencies of H_4SiO_4 monomer tetrahedral-antisymmetric-stretch-like vibrations by a few tens of wavenumbers (McIntosh et al., 2011). The influence of molecular environment on the SiOH bending mode δSiOH is even stronger. NMA studies that neglected the frequency shifting effect of environment assumed vibrational coupling of δSiOH and tetrahedral stretching modes (Lasaga and Gibbs, 1988). However, the

frequency of δSiOH increases by a few hundred wavenumbers when aqueous environment is considered implicitly (McIntosh et al., 2011). Here, dynamical calculations at finite temperatures give insight into the temperature dependence of the δSiOH.

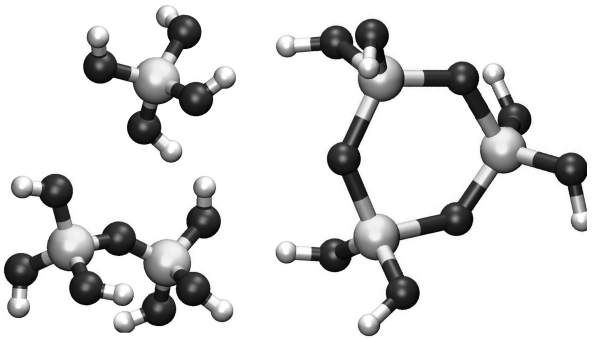

Fig. 3.1: The H_4SiO_4 monomer, $H_6Si_2O_7$ dimer and $H_6Si_3O_9$ ring trimer. Figure was drawn with *VMD* (Humphrey et al., 1996).

There are numerous ab initio Raman spectra of small silica species, mostly calculated in the gas-phase (Lasaga, 1982; Hess et al., 1986; De Almeida and O'Malley, 1991, 1993; Kubicki and Sykes, 1993; Tossell, 2005; Hunt et al., 2011; McIntosh et al., 2011). However, calculated spectra vary for the $H_6Si_2O_7$ dimer and larger species (Fig. 3.1). One reason for this is that in NMA the external and internal degrees of freedom of a species, including for example the bond angles, are not sampled sufficiently. For example, the internal Si-O-Si bending angle of the $H_6Si_2O_7$ dimer, to which vibrational frequencies of the dimer are sensitive, may vary significantly (Hunt et al., 2011). Therefore, the vibrational properties of species such as the $H_6Si_2O_7$ dimer are not yet fully understood (Tossell, 2005), and it is not entirely clear under which conditions silica in dilute solutions forms $H_6Si_2O_7$ dimers or higher polymers such as threefold or larger silica rings (Alvarez and Sparks, 1985; Dutta and Shieh, 1985b; Tossell, 2005; Mora-Fonz et al., 2007; Trinh et al., 2009). The different theoretical levels used in various studies optimize the dimer to different Si-O-Si angles between 128° and 170° (Kubicki and Sykes, 1993; Tossell, 2005; Hunt et al., 2011). Dynamical sampling of the vibrational properties of the dimer at finite temperatures could lead towards more statistically converged spectra.

In this study, we investigate the vibrational properties of the H_4SiO_4 and D_4SiO_4 monomers, the $H_6Si_2O_7$ dimer and the $H_6Si_3O_9$ ring trimer. This work is an extension of previous studies that focused on polymerization-driven changes in tetrahedral modes of the SiO_4^{4-} in a silica network in aqueous solution, hydrous silica glass and magnesiosilicate glass (Chapter 2 and 4). Here, our goal is to derive mode-specific frequencies of small silica species, and the dependence of the frequencies on temperature and environment. We investigate the frequencies of tetrahedral and bridging oxygen vibrational modes by the combination of ab initio MD and a mode-projection technique which yields a decomposition of the complete vibrational density of states into mode-specific subspectra. We investigate the influence of distortion on BO and tetrahedral modes of the $H_6Si_3O_9$ ring trimer. Also, we extend this approach to a detailed analysis of the SiOH bending mode. The mode-decomposition approach allows for the dynamic calculation of the vibrational properties, which is especially advantageous for estimation of the dependence of the vibrational frequencies on temperature and changes in the solvent environment. This is especially important in the case of the SiOH bending vibration, which is sensitive to both environment and temperature. We compare the mode-decomposition results to normal-mode analysis (NMA) to show the general consistency between the two methods for vibrational modes that are only weakly dependent on temperature.

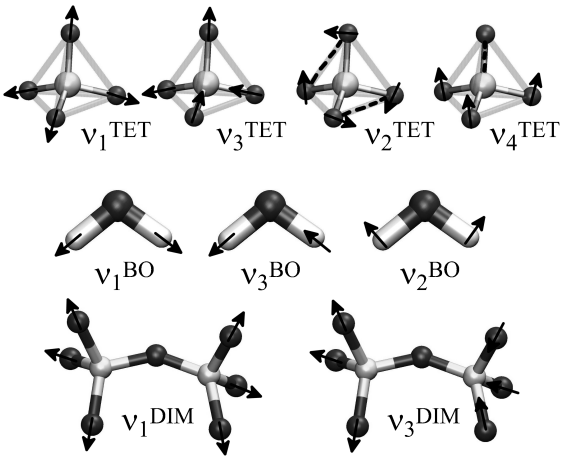

Fig. 3.2: Three groups of quasi-normal modes (QNMs) used in this study (Table 4.3). Arrows indicate the velocity component of interest, i.e. the first projection. Dashed lines in bending modes represent additional projection vectors where a second projection is necessary (see Chapter 2). Parts of the Figures were drawn with *VMD* (Humphrey et al., 1996), modified from Chapter 2.

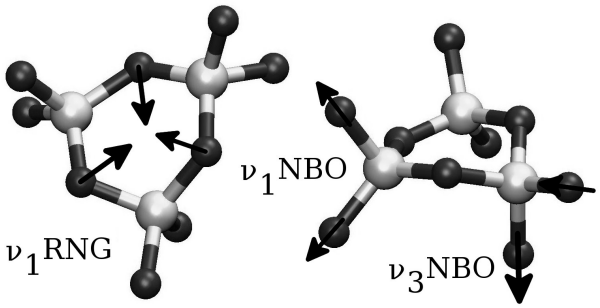

Fig. 3.3: The ring trimer modes of ring breathing ν_1^{RNG} and geminal non-bridging oxygen (NBO) ν_1^{NBO} symmetric and ν_3^{NBO} antisymmetric stretch.

3.3 Methods

Molecular dynamics simulations and normal mode analysis

For the calculation of MD trajectories, we employed the same technical setup as described in Chapter 2, i.e. density functional theory (Kohn and Sham, 1965) in the plane wave pseudopotential approach, as implemented in the CPMD code (Marx and Hutter, 2000), with the PBE exchange-correlation functional (Perdew et al., 1996) and Martins-Troullier type pseudopotentials (Troullier and Martins, 1991). The Kohn-Sham wavefunctions were expanded at the Γ-point with a plane wave cutoff energy of 80 Ry. Car-Parrinello molecular dynamics (Car and Parrinello, 1985) was used with a ficticious electronic mass of 400 a.u. and a time step of 4 a.u. (0.097 fs). Atomic positions and velocities were recorded every 40 a.u. We conducted several MD runs of monomers, dimers and ring trimers in the gas-phase and in aqueous solution at constant volume, varying temperature (300 K and 1000 K) and environment (Table 4.1). Each run duration was 75 ps. All silica species in the solution runs were surrounded by 24-27 water molecules within periodic boundary conditions. The total number of atoms in each of the solution runs was between

Table 3.1: Quasi-normal modes (QNMs) discussed in this study (Figs. 4.1 and 3.3). See Chapter 2 for other QNMs in higher polymerized silica species.

Mode:	symmetry:	abbreviation:
tetrahedral QNMs:	T_d	
symmetric stretch	A_1	ν_1^{TET}
antisymmetric stretch	F_2	ν_3^{TET}
E-bending	E	ν_2^{TET}
umbrella-bending	F_2	ν_4^{TET}
SiOH/SiOD bending QNMs:	treated as	
SiOH/SiOD bending	C_{2v}	δSiOH/δSiOD
bridging oxygen QNMs:	C_{2v}	
Si-O-Si symmetric stretch	A_1	ν_1^{BO}
Si-O-Si antisymmetric stretch	B_2	ν_3^{BO}
Si-O-Si bending	A_1	ν_2^{BO}
ethane-like QNMs:	D_{3d}/D_{3h}	
symmetric stretch	A_1	ν_1^{DIM}
antisymmetric stretch	B_2	ν_3^{DIM}
O-Si-O QNMs for non-bridging oxygens:	C_{2v}	
symmetric stretch	A_1	ν_1^{NBO}
antisymmetric stretch	B_2	ν_3^{NBO}
ring breathing QNM:	treated as	
symmetric breathing	C_{3v}	ν_1^{RNG}

90 and 100. Temperature was controlled by a Nosé-Hoover thermostat (Martyna et al., 1992). All Si-O and O-H bonds persisted throughout all MD runs, at both temperatures of 300 K and 1000 K.
For the monomer and the dimer, we performed gas-phase normal mode analysis (NMA) at 140 Ry plane wave cutoff after geometric relaxation. For the NMA of the monomer and dimer in solution, 200 equally separated configurations were chosen from each of the trajectories of the H_4SiO_4 monomer and the $H_6Si_2O_7$ dimer in solvation at 1000 K. All silicon, oxygen and hydrogen atoms belonging to the investigated species were geometrically relaxed within their frozen-in environment. Then NMA was carried out at 80 Ry plane wave cutoff which is the same cutoff as employed in the molecular dynamics runs. Convergence was tested with a 140 Ry cutoff, and NMA frequencies between 400 cm^{-1} and 1000 cm^{-1} were found to vary by about $\pm 10\,cm^{-1}$ or less. Finite displacement of all atoms of the molecular unit and subsequent diagonalization of the dynamical matrix yielded the frequencies as eigenvalues. Good sampling of "in situ" NMA was achieved by compiling the 200 frequency results into a single frequency histogram with a bin width of $10\,cm^{-1}$.

The mode-projection approach

Spectral decomposition of the complete vibrational density of states is achieved by the mode-projection approach. This method is described in Chapter 2. Raman bands in the frequency region of 200 to $1200\,cm^{-1}$ arise from normal-mode-like, quasi-localized vibrations of specific structural subunits of the silica species. These structural subunits are mainly the SiO_4^{4-} tetrahedron of symmetry T_d, and the Si-O-Si bridging oxygen (BO) of symmetry C_{2v} (H_2O-like, Fig. 4.1). The vibrations of these structural subunits of the silica species are similar, in terms of directions and symmetry of motion, to the normal

Table 3.2: Overview of simulation runs.

run label	gas-phase or in solution	T (K)	composition and species	density (g/cm^3)
monomers:				
M-B-300K	in solution	300	H_4SiO_4 + 27 H_2O	0.95
M-B-700K	in solution	700	H_4SiO_4 + 27 H_2O	0.95
M-B-1000K	in solution	1000	H_4SiO_4 + 27 H_2O	0.95
M-B-300K-D	in solution	300	D_4SiO_4 + 27 H_2O	0.95
M-B-300K-dense	in solution	300	H_4SiO_4 + 27 H_2O	1.04
M-G-300K	gas-phase	300	H_4SiO_4 (gas-phase)	–
M-G-1000K	gas-phase	1000	H_4SiO_4 (gas-phase)	–
dimers:				
D-B-300K	in solution	300	$H_6Si_2O_7$ + 25 H_2O	1.02
D-B-1000K	in solution	1000	$H_6Si_2O_7$ + 25 H_2O	1.02
D-G-300K	gas-phase	300	$H_6Si_2O_7$ (gas-phase)	–
D-G-1000K	gas-phase	1000	$H_6Si_2O_7$ (gas-phase)	–
ring trimers:				
T-B-300K	in solution	300	$H_6Si_3O_9$ + 24 H_2O	1.09
T-B-1000K	in solution	1000	$H_6Si_3O_9$ + 24 H_2O	1.09

modes of the respective isolated molecules. This is irrespective of the surroundings and degree of polymerization of a molecular subunit, for example a SiO_4^{4-} tetrahedron. The vibrational frequencies are the only unknowns, and the frequencies depend on the environment and degree of polymerization (see Chapter 2 and 4).

The power spectrum of a group of atoms is calculated via the Fourier transform of the effective velocity autocorrelation function (VACF)

$$F(\omega) = \int_0^{t_{max}} cos(\omega t) dt \langle v_{QNM}(t) \cdot v_{QNM}(0) \rangle, \tag{3.1}$$

where $F(\omega)$ is the spectral density, ω is the angular frequency, and chevrons indicate the ensemble average (Allen and Tildesley, 1987). v_{QNM} is an effective scalar velocity which is calculated by summing the magnitudes of the projected oxygen velocity vectors according to the tetrahedral QNMs, or the projected silicon velocity vectors according to the bridging oxygen QNMs (Fig. 4.1 and Table 4.3). If the unprojected, complete atomic velocity vectors were used in equation 4.1, the resulting spectrum then would include all vibrational contributions, including translational, rotational and low-frequency long-range acoustic-like vibrations. The spectroscopically relevant normal-mode-like vibrations of the individual structural subunits cannot easily be extracted from such a full vibrational density of states. Instead, we use a method that extracts the normal-mode-like vibrations individually. Extraction is achieved by the projection of the atomic velocity vectors of a structural subunit on quasi-normal modes (QNMs) that are almost identical to the molecular normal modes, but do not consider the motions of the central atom of a given unit (Fig. 4.1). This has no effect on the peak frequency of the vibrational subspectra (see Chapter 2). Mode-wise decomposition of the structurally grouped atomic velocity vectors, autocorrelation and Fourier transform give vibrational subspectra for every QNM of a structural subunit.

The dimer is characterized by ethane-like intertetrahedral symmetric and antisymmetric stretch of its O_3Si-O-SiO_3 part, in addition to the Raman active vibrations of the two tetrahedra and the bridging oxygen group (Table 4.3). The ring trimer possesses a ring breathing mode ν_1^{RNG} (Fig. 3.3) which is similar to a coupled symmetric stretch of the three bridging oxygen atoms. The two non-bridging oxygen atoms at each of the three tetrahedra possess water-like symmetric and antisymmetric stretching modes ν_1^{NBO} and ν_3^{NBO}. The SiOH bending δSiOH is necessary to characterize the vibrational properties

of the monomer and the dimer in the frequency range up to 1200 cm^{-1}. It is recorded from the oscillation of the Si-O-H bending angle (McIntosh et al., 2011). The O-H stretching is beyond 3000 cm^{-1} and not part of this study.
The resulting QNM-wise subspectra are evaluated in terms of their peak frequency. The absolute spectral density of a QNM should not be compared between different QNMs, because the calculation is different for every QNM, involving projections, addition and subtractions (Chapter 2). However, spectra of the same QNM but different simulation runs can be compared to one another. Comparison of the peak height reveals changes in the vibrational intensity with changing conditions. The width of the subspectra presented here results from the finite simulation time. For smoothing, spectra were convoluted with a Gaussian with σ=20 cm^{-1}. We estimate the error of the frequency to be about 10 cm^{-1} for the tetrahedral and ethane-like stretching modes, based on the scatter of spectra calculated from different segments of the trajectory. For the Si-O-Si modes, this error is about 20 cm^{-1}, because the Si-O-Si vibrational frequencies are sensitive to the Si-O-Si bending angle that varies slowly in time with respect to the MD trajectory length.

Frequency scaling

In a previous study we derived a scaling factor of 1.039 to account for the systematic error of ab initio MD with the technical details described above (Chapter 2). This factor was calculated from the comparison of the ν_1^{TET} spectrum to experimental values. The factor is in good agreement to common low-frequency scaling factors for PBE (Merrick et al., 2007). All following spectra and extracted frequencies in this study are scaled by this factor. In this study we focus on stretching modes because of their importance in Raman spectroscopy of silica species.

3.4 Results

Tetrahedral modes of the H_4SiO_4 monomer

Table 3.3: Overview over tetrahedral QNMs and δSiOH/δSiOD peak frequencies from various monomer runs. Frequencies (cm^{-1}) are scaled by 1.039.

run conditions	QNMs and frequencies		
	ν_1^{TET}	ν_3^{TET}	δSiOH/δSiOD
solution, 300 K, 1.04 g/cm^3	778	954	1175
solution, 300 K, 0.96 g/cm^3	770	940	1145
solution, 700 K	756	910	1005
solution, 1000 K	765	923	930
gas, 300 K	757	970	845
gas, 1000 K	753	953	864
solution, 300 K, D_4SiO_4	750	950	830

The spectra of the four tetrahedral QNMs of the monomer at 1000 K have been shown in an earlier study (Chapter 2). We include those results in part A of Fig. 3.4 and in Table 3.3 for comparison to results at different temperature and in the gas phase, and to NMA frequencies in part B and C. The peak frequencies of stretching modes are 765 cm^{-1} for ν_1^{TET} and 923 cm^{-1} for ν_3^{TET} (Table 3.3). Single-oxygen Si-O_H stretching vibrations have the same spectrum and peak frequency as ν_3^{TET} (see also Chapter 2).
Part B of Fig. 3.4 shows the scaled histogram of NMA frequencies from the 200 different configurations of the H_4SiO_4 in solution run at 1000 K. The QNM spectra peaks match well with the peak frequencies of the NMA frequency histogram to within 10 to 20 cm^{-1}. The NMA frequencies below 250 cm^{-1}

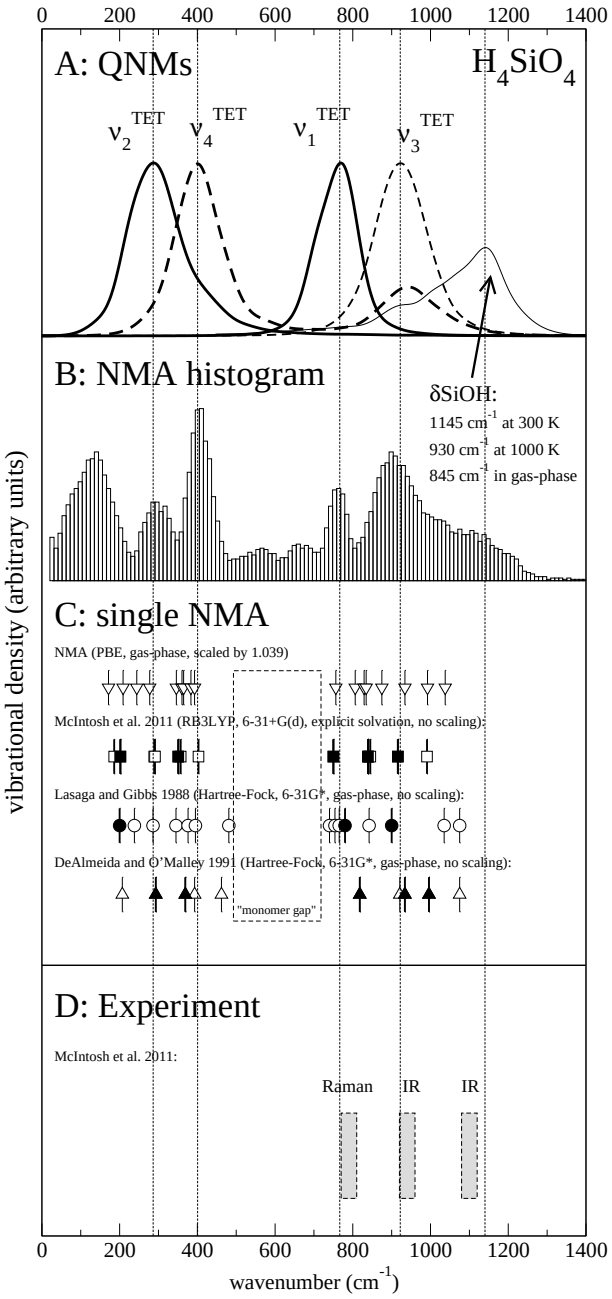

Fig. 3.4: A: Spectral density distributions of the four tetrahedral QNMs at 1000 K. B: Frequency histogram of NMA frequencies from in situ NMA of the same monomer from 200 snapshots of the run. C: NMA frequencies from the present study, and literature computational ab initio Raman frequencies from NMA below 1200 cm^{-1}. Full symbols represent modes with Raman activity of at least 1% of that of the tetrahedral symmetric stretch near 770 cm^{-1}. The dashed box indicates the wavenumber region where the monomer does not have a vibrational mode in any computational study.

represent external modes that result from monomer rotations and translations, which are not recorded by the tetrahedral QNMs. The NMA histogram shows a widely spread shoulder centered around 1140 cm^{-1}. This results from the mode with a strong δSiOH contribution. In part A, the δSiOH is plotted for 300 K, because at 1000 K the δSiOH would be shifted into the tetrahedral antisymmetric stretching range

around 925 cm^{-1}. This point will be discussed below. However, together with the δSiOH spectrum, the tetrahedral QNM modes completely cover the NMA frequencies in relevant range for silica species of 250-1200 cm^{-1}.
In part C of Fig. 3.4 scaled gas-phase NMA frequencies from the present study are plotted, together with other literature NMA frequencies for the monomer (Lasaga and Gibbs, 1988; De Almeida and O'Malley, 1991; Hunt et al., 2011). Lasaga and Gibbs (1988) as well as De Almeida and O'Malley (1991) employed gas-phase Hartree-Fock, whereas Hunt et al. (2011) employed hybrid-DFT with aqueous solvent environment. These differences explain the scatter of the literature frequencies. In the literature studies also the Raman intensities of the NMA modes were calculated. We highlight those modes with filled symbols whose Raman intensity is at least 1% of that of the most Raman intense mode in each study.
The tetrahedral stretching QNMs of the D_4SiO_4 at 300 K yield similar frequencies as the D_4SiO_4 monomer (Table 3.3). The temperature shift of the tetrahedral QNM peak frequencies in the range of 300 K to 1000 K is about -10 cm^{-1} for ν_1^{TET} and about -20 cm^{-1} for the ν_3^{TET}, which gives reasonable temperature dependencies between -0.014 $cm^{-1}K^{-1}$ and -0.028 $cm^{-1}K^{-1}$ (Table 3.3). The runs for different temperatures were carried out at constant volume. For this reason, the influence of increasing temperature and pressure cannot be entirely distinguished from one another. This explains the wavenumber increase of the ν_1^{TET} between 700 K and 1000 K. Experiments in hydrothermal diamond anvil cells (HDAC) are also commonly carried out isochorically with a similar simultaneous increase of temperature and pressure. The inclusion of environment increases the wavenumber of the ν_1^{TET} by about 10 cm^{-1} and the ν_3^{TET} by 30 cm^{-1}. Higher pressure also increases the tetrahedral QNMs wavenumbers (Table 3.3), in agreement with experimental observation (Zotov and Keppler, 2002; Schmidt and Watenphul, 2010).

The δSiOH/δSiOD of H_4SiO_4 and D_4SiO_4

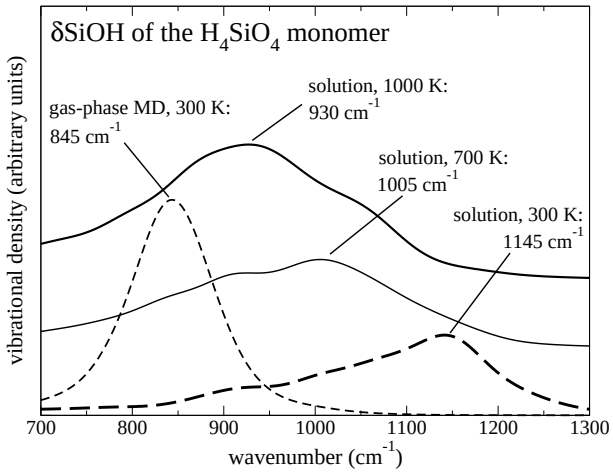

Fig. 3.5: The δSiOH QNM spectra at different conditions as indicated. The gas-phase spectrum has been downscaled by a factor of 4.0 for comparison. Spectra of 700 K and 1000 K are shifted upward for visualization.

We investigated the vibrational frequencies of the δSiOH/δSiOD vibrations of the H_4SiO_4 and D_4SiO_4 monomers (Fig. 3.5), which have been recently studied experimentally (McIntosh et al., 2011). The peak frequency of δSiOH in aqueous solution is at about 1145 cm^{-1} for 300 K, at 1005 cm^{-1} for 700 K and at 930 cm^{-1} for 1000 K. This corresponds to a wavenumber decrease of about 200 cm^{-1} due to temperature increase from 300 K to 1000 K. The contribution of the simultaneous pressure increase cannot be estimated independently, but pressure rather increases than decreases the frequency of the δSiOH, as

the comparison of the results at densities of 0.95 g/cm^{-3} and 1.04 g/cm^{-3} show (Table 3.3). The peak frequency of 930 cm^{-1} at 1000 K is close to the peak of ν_3^{TET} at 923 cm^{-1}, indicating that coupling of δSiOH to tetrahedral modes is promoted at high temperatures. The peak for the δSiOH vibrations is centered at 845 cm^{-1} in the gas-phase MD run at 300 K (Figs. 3.5 and 3.6). The proximity of δSiOH to the tetrahedral ν_1^{TET} and ν_3^{TET} shows that in the gas-phase the δSiOH couples to these tetrahedral modes (Fig. 3.6). The wavenumber of the δSiOH increases by about 300 cm^{-1} to 1145 cm^{-1} if the aqueous environment is included at 300 K. As a consequence, there can be no coupling between δSiOH and tetrahedral stretching modes in solution at ambient conditions (McIntosh et al., 2011), although high temperatures render the coupling possible. The δSiOD frequency in solution at 300 K is at 830 cm^{-1}. This is in reasonable agreement with recent experimental result of 800 cm^{-1} (McIntosh et al., 2011).

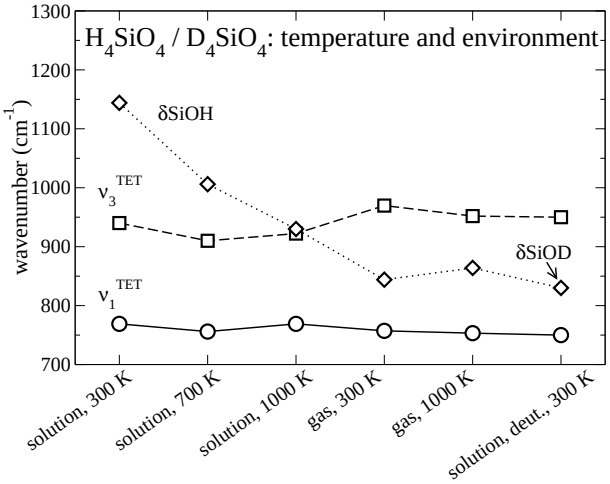

Fig. 3.6: Overview of the H_4SiO_4 peak frequencies of the two tetrahedral stretching modes ν_1^{TET} and ν_3^{TET} and the δSiOH/δSiOD, with changing temperature and environment.

Vibrational properties of the $H_6Si_2O_7$ dimer

We compare the tetrahedral, bridging oxygen and ethane-like stretching QNMs of the dimer (Chapter 2) to NMA results (Fig. 3.7). The symmetric stretch ν_1^{TET} of the two dimer Q^1 tetrahedra for 1000 K is at 790 cm^{-1}, the ν_3^{TET} is at 946 cm^{-1} (part A of Fig. 3.7 and Table 3.4). Both frequencies differ only weakly from the respective tetrahedral QNM frequencies of the monomer. The ν_1^{BO} vibration is at about 620 cm^{-1}. The subordinate peak at 880 cm^{-1} is an artifactorial "shadow" of the ν_1^{DIM} mode, resulting from the similarity of motion of both modes for the Si-O-Si sub-unit of the dimer (part A in Fig. 3.7, see Chapter 2 for a discussion of this artifact). The bridging oxygen antisymmetric stretch ν_3^{BO} is at 1114 cm^{-1} for 300 K. The ethane-like ν_1^{DIM} of the neutral dimer is at 900 cm^{-1}, and the ν_3^{DIM} is at 785 cm^{-1}. This is almost identical to the peak frequency of ν_1^{TET}. The SiO_3 symmetric stretching (NH_3-like) of each of the terminal ends of the dimer is identical to ν_1^{TET}.

The dimer NMA frequency histogram for frequencies above 400 cm^{-1} shows several pronounced peaks and shoulders (part B of Fig. 3.7). All QNM peak frequencies except the ν_1^{DIM} match with NMA peaks to within 20 cm^{-1}. The dimer symmetric stretch ν_1^{DIM} agrees with a weak shoulder at about 870 cm^{-1}. The agreement of QNM and NMA peaks reflects the fact that the normal modes of the dimer can be decomposed into quasi-normal modes of tetrahedral, bridging oxygen and ethane-like character. Literature NMA frequencies are plotted in part C of Figure 3.7. They agree well in the frequencies of the most intense band around 610 cm^{-1}, but differ in the frequencies of other Raman intense stretching modes between 840 cm^{-1} and 1040 cm^{-1}. Several dimer modes are sensitive to the Si-O-Si bending

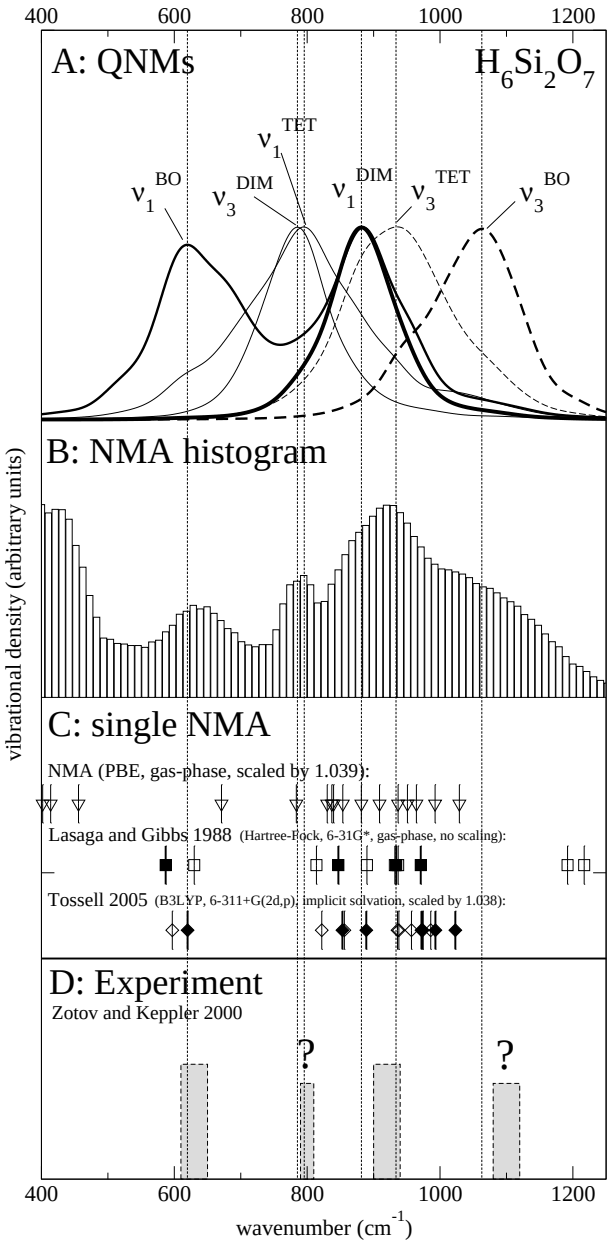

Fig. 3.7: A: The stretching QNM spectra of the dimer at 1000 K. B: NMA frequency histogram of the dimer. C: Raman frequencies of the dimer above 500 cm^{-1} from literature ab initio calculations, full symbols represent Raman modes that have at least 1% intensity of the most intense band at about 600 to 620 cm^{-1}. D: Experimental band assignment after Zotov and Keppler (2000).

angle. This explains the scattering width of the ν_3^{BO}-like NMA modes centered around 1060 cm^{-1}. It also explains part of the scatter of literature frequencies.

The effect of temperature on the dimer QNMs is in the order of -10 cm^{-1} to -20 cm^{-1}, with an unknown influence of the simultaneous pressure increase. The effect of environment is slightly greater, up to 30 cm^{-1} (Fig. 3.8 and Table 3.4). An exception to that is the ν_3^{BO} that decreases in wavenumber by 50 cm^{-1} upon temperature increase from 300 K to 1000 K.

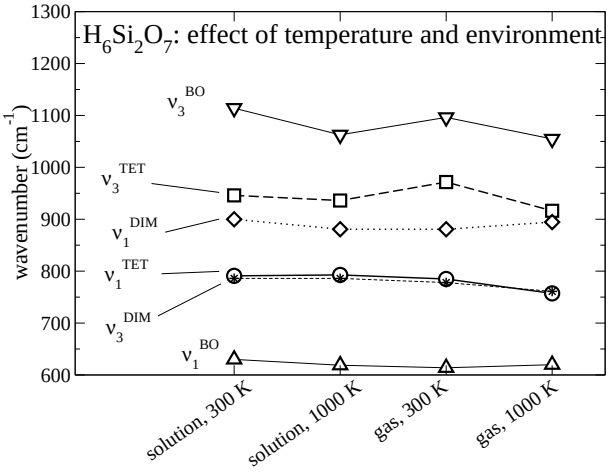

Fig. 3.8: Overview of the effect of temperature and environment on the dimer frequencies of the tetrahedral ν_1^{TET} and ν_3^{TET}, the bridging oxygen ν_1^{BO} and ν_3^{BO} and the ethane-like ν_1^{DIM} and ν_3^{DIM} QNMs.

Table 3.4: Overview over the dimer stretching QNM peak frequencies for various run conditions. Frequencies (in cm^{-1}) are scaled by 1.039.

run conditions	QNMs and frequencies					
	ν_1^{TET}	ν_3^{TET}	ν_1^{DIM}	ν_3^{DIM}	ν_1^{BO}	ν_3^{BO}
solution, 300 K	790	946	900	785	630	1114
solution, 1000 K	793	936	880	785	619	1062
gas, 300 K	785	972	868	778	614	1096
gas, 1000 K	757	916	895	760	620	1055

The $H_6Si_3O_9$ ring trimer

Finally, we investigate the tetrahedral, BO and terminal HO-Si-OH stretching modes of the ring trimer, and also the ring breathing, which is very similar to the ν_1^{BO}. The torsion of the tetrahedra enforces several QNMs into a hybrid, mutually mixed state, with significant vibrational transfer between modes. For instance, the ν_1^{TET} shows its genuine peak at 920 cm^{-1} (Fig. 3.9), but an additional peak at 720 cm^{-1} which is the domain of Si-O-Si bending vibrations. The ν_1^{BO} itself shows transfer from the ν_1^{TET} and from the lower-frequency ring breathing mode at 585 cm^{-1}. The ν_3^{TET} is at 955 cm^{-1}. This is slightly lower than the earlier found value of 970 cm^{-1} for unstrained Q^2-species (Chapter 2). The ν_3^{BO} is at 970 cm^{-1}, as compared to about 1100 cm^{-1} in the dimer and to 1050 cm^{-1} in the linear trimer. This wavenumber increase of ν_3^{BO} in the threefold ring is in agreement with other NMA-derived Raman spectra (Hunt et al., 2011). The stretching modes of the two geminal non-bridging oxygen atoms at each tetrahedron have the specific symmetric and antisymmetric stretching modes that are at 917 cm^{-1} and 940 cm^{-1}, respectively (Fig. 3.9).

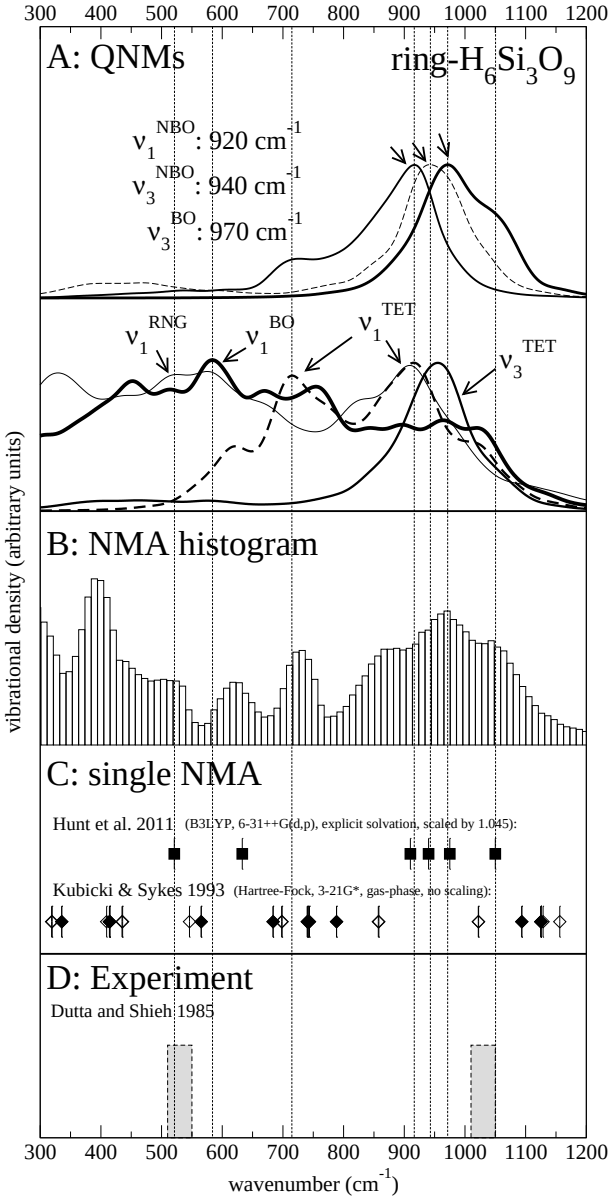

Fig. 3.9: Top: Terminal HO-Si-OH symmetric stretch (ν_1^{NBO}) and antisymmetric stretch (ν_3^{NBO}) and ν_3^{BO} of the $H_6Si_3O_9$ ring trimer. Bottom: ν_1^{TET}, ν_3^{TET} and ν_1^{BO} of the ring trimer. ν_1^{TET} and ν_1^{BO} are mutually mixed and influenced by a ring breathing mode.

3.5 Discussion

Monomer tetrahedral modes

The monomer tetrahedral stretching QNM peak frequencies in Fig. 3.4 and Table 3.3 are in good agreement to the NMA results and to common experimental band assignment of ν_1^{TET} and ν_3^{TET} (Freund, 1973; Dutta and Shieh, 1985b; McIntosh et al., 2011). The QNM approach yields only one peak frequency for the ν_3^{TET}. It thereby overcomes the situation that single-configuration NMA commonly yields several modes with a predominantly ν_3^{TET} character, with a considerable spread in frequency of about 200 cm^{-1} which is not reflected in experiments (Fig. 3.4). Calculated temperature dependencies of the tetrahedral stretching QNMs of -0.028 $cm^{-1}K^{-1}$ or less are in good agreement to the experimentally

determined isochoric value of -0.02 to -0.03 $cm^{-1}K^{-1}$ for ν_1^{TET} (Zotov and Keppler, 2002).

Monomer δSiOH/δSiOD modes

The δSiOH and δSiOD of 1145 cm^{-1} and 830 cm^{-1} at 300 K agree well with recent experimental infrared assignments of 1100 cm^{-1} and 800 cm^{-1}, respectively (McIntosh et al., 2011). The inclusion of aqueous environment at 300 K increases the δSiOH frequency from 845 cm^{-1} in the gas-phase MD to about 1145 cm^{-1} in water (Table 3.4 and Fig. 3.5). Based on the similarity of the gas-phase NMA δSiOH frequencies to tetrahedral stretching modes of the monomer, it had been assumed that there is coupling of δSiOH and SiO_H stretching vibrations (Lasaga and Gibbs, 1988; McIntosh et al., 2011). As reported recently (McIntosh et al., 2011), our results indicate that there is no coupling between SiO_H stretching and δSiOH in aqueous environment at ambient conditions.
This situation changes at elevated temperatures. The δSiOH vibrations decrease in wavenumber from 1145 cm^{-1} at 300 K to 940 cm^{-1} at 1000 K (Fig. 3.5 and Table 3.4), which is equal to the ν_3^{TET} at 940 cm^{-1}. Therefore, the coupling between δSiOH vibrations and tetrahedral stretching modes is promoted at higher temperatures. This temperature shift of the δSiOH could be detectable in experiment, unless changes in speciation at elevated temperatures, away from the neutral monomer, overprint the signal from δSiOH. The δSiOH produces only a weak IR signal and virtually no Raman signal (McIntosh et al., 2011). The computational investigation of the temperature-dependence of the δSiOH requires dynamical handling as in the QNM approach. Single-configuration or even multiple-configuration NMA histograms, as employed here, cannot detect the high-temperature wavenumber decrease. The resulting frequency would be that of low-temperature runs because of the necessary geometric relaxation prior to NMA. This is true even if the multiple-configuration NMA is carried out on MD trajectories at e.g. 1000 K.
The effect of temperature and environment on the δSiOH frequency as just described are significantly stronger than the influence of the choice of the exchange-correlation functional and the neglect of dispersion forces (Demichelis et al., 2010). The agreement of the calculated δSiOH frequencies with experiment and hybrid-DFT calculations is surprisingly good (Tossell, 2005; McIntosh et al., 2011; Hunt et al., 2011).

Vibrational properties of the $H_6Si_2O_7$ dimer

The dimer possesses the structural degree of freedom of Si-O-Si bending angle, which partly explains the large scatter of different frequency results from several NMA studies (part C in Fig. 3.7) (Lasaga and Gibbs, 1988; Zotov and Keppler, 2000, 2002; Tossell, 2005; Hunt et al., 2011). The occupancy of the Si-O-Si angle needs to be sampled sufficiently, because the frequencies of several vibrational modes of the dimer depend on the Si-O-Si bending angle (Kubicki and Sykes, 1993; Hunt et al., 2011). Sufficient sampling is achieved by the dynamical calculation at finite temperature. The approach to decompose the vibrations of the dimer into tetrahedral, BO and ethane-like QNMs was successful in matching own NMA data and literature data of calculated vibrations with a high Raman activity. The contribution of the ν_1^{BO} at about 600 cm^{-1} to 620 cm^{-1} and its high Raman intensity is a consistent result of our and other studies (Lasaga and Gibbs, 1988; Zotov and Keppler, 2000, 2002; Tossell, 2005; Hunt et al., 2011). The comparison of QNM results to NMA, including Raman intensities, suggests several interesting conclusions.
The frequency of the dimer (Q^1) ν_1^{TET} vibration at 793 cm^{-1} is close to the same mode of the monomer at 770 cm^{-1}. The importance of this mode for Raman spectra can be observed in the case of wadsleyite with its basic silicate structure of $Si_2O_7^{6-}$ and its Raman intense band at 778 cm^{-1} (Kleppe et al., 2006). The Raman intensity of the Q^1 ν_1^{TET} in fluids is not known. However, it is commonly assumed that ν_1^{TET} maintains the high Raman intensity throughout the different degrees of polymerization (McMillan, 1984; Mysen and Richet, 2005). We suggest that the dimer mode is the reason for an experimentally observed

shift of the monomer 770 cm^{-1} band towards higher wavenumbers, which occurs with polymerization of basic solutions (Alvarez and Sparks, 1985; Dutta and Shieh, 1985b). Also in Raman spectra (Zotov and Keppler, 2000) there is a shoulder at 800 cm^{-1} to the main peak at about 770 cm^{-1} (Fig. 3.7). This shoulder emerges simultaneously with other bands assigned to the dimer, but it was not previously addressed.

The dimer-specific ν_1^{DIM} is at 880 cm^{-1} for 1000 K. This frequency matches well with a Raman intense, but poorly characterized vibration between 850 cm^{-1} and 890 cm^{-1}, which has been previously observed in scaled hybrid-DFT NMA (Tossell, 2005; Hunt et al., 2011) and classical calculations (Zotov and Keppler, 2000). The ν_3^{DIM} at 778 cm^{-1} for 1000 K is very close to the monomer and dimer ν_1^{TET} (Table 3.4). The Raman intensity of ν_3^{DIM} is not known, but in addition to the dimer ν_1^{TET} it is the second mode that might also contribute to the Raman band at 770 cm^{-1} that is commonly assigned to monomers only.

The ν_3^{BO} frequency occurs at about 1062 cm^{-1}, which is in good agreement to experimental assignments of a Raman intense experimental band between 1050 cm^{-1} and 1100 cm^{-1} (Freund, 1973; Zotov and Keppler, 2002; Tossell, 2005; Hunt et al., 2011). In modeling the ν_3^{BO} frequency is very sensitive to the Si-O-Si bending angle of the geometrically optimized dimer (Hunt et al., 2011). This explains why this vibrational state does not always appear to be "filled" in different NMA settings in the literature (Hunt et al., 2011). In fact, none of the literature NMA studies in Fig. 3.7 shows a Raman intense frequency above 1030 cm^{-1}, except one where the Si-O-Si angle is only 133°, as opposed to commonly greater than 160° (Hunt et al., 2011). We attribute this to the insufficient sampling of gas-phase NMA with respect to the dynamically treated dimer.

Vibrational properties of the $H_6Si_3O_9$ ring trimer

The ring trimer deserves attention, because is an energetically favorable species (Tossell, 2005), and a few experimental studies invoke the ring trimer for interpreting Raman spectra (Dutta and Shieh, 1985b; Hunt et al., 2011). However, the vibrational properties of the ring trimer are poorly understood. The tetrahedral and BO QNMs, that show remarkable changes are compared to the dimer. In addition to these modes, we investigated the pair of non-bridging oxygen (NBO) of each tetrahedron with the H_2O-like C_{2v} set of QNMs, as described above for BO.

The most remarkable observation is that the ν_1^{TET}, ν_3^{TET}, ν_1^{NBO} and ν_3^{NBO} peak frequencies of the ring trimer Q^2 tetrahedra are all distributed between 917 cm^{-1} and 955 cm^{-1}. We do not have information on the Raman intensity of the ν_1^{NBO} and ν_3^{NBO}. However, considering the equivalent modes of the water molecule, both can be assumed to contribute to Raman bands (Murphy, 1978). The ν_3^{BO} peak frequency is at 970 cm^{-1}, considerably lower than above 1050 cm^{-1} for the dimer. This shows that bridging oxygen can be present without a contribution in the region above 1050 cm^{-1} where the ν_3^{BO} is commonly located. The QNM spectra show mutual contributions to an amount that is not observed in the monomer and dimer. We attribute this to the strain of the Si-O-Si angle that leaves the bridging oxygen less "freedom" to act as BO without interference to its simultaneous role as part of two tetrahedral QNMs.

The ring breathing at 585 cm^{-1} is in close agreement to the 606 cm^{-1} feature in silica glass that is commonly assigned to threefold silica rings (Galeener, 1979; Barrio et al., 1993; Giacomazzi et al., 2009). The spectrum spans the complete spectral range up to the domain of ν_1^{TET}, which is due to the mode overlap that is further increased by the strain of the tetrahedra. The ring breathing is contains a stretching and a bending component. The QNM projection is not well suited for bending modes because of their low frequency and the sensitivity of bending frequencies to small changes in configuration. Other approaches may be more useful for the direct determination of the frequencies of bending modes (Martinez et al., 2006).

3.6 Conclusions

We calculated the vibrational properties of the H_4SiO_4 and D_4SiO_4 monomers, the $H_6Si_2O_7$ dimer and the $H_6Si_3O_9$ ring trimer, using a combination of ab initio MD and the mode-projection approach. The dynamical decomposition of the vibrational motions of species results in subspectra with distinct structural and modal origin.

We also calculated NMA frequency histograms for these species from a few hundreds of MD trajectory configurations. The comparison to literature data of single-configuration NMA showed that such multiple-configuration NMA is useful for the determination of the dynamical occupation of vibrational states. The agreement between QNM and NMA results is good for vibrational modes whose temperature dependence is weak, such as the SiO_4^{4-} tetrahedral modes.

We found that there are vibrational frequencies of the dimer (Q^1) of ν_1^{TET} in character at 790 cm^{-1}. This is near to the Raman band at about 770 cm^{-1} which is commonly assigned to the monomer ν_1^{TET} only, but which shows a hitherto unexplained shoulder at about 800 cm^{-1} (Dutta and Shieh, 1985b; Alvarez and Sparks, 1985; Zotov and Keppler, 2000). The dimer ν_1^{TET} is assumed to be a Raman intense mode (Zotov and Keppler, 2000; McMillan, 1984; Mysen, 2009). We therefore suggest that the 770 cm^{-1} Raman band originates not only from the H_4SiO_4 monomer, but partly also from the dimer.

One of the advantages of the mode-decomposition approach over NMA is that the temperature dependence of vibrational frequencies can be observed directly. We found the δSiOH mode sensitive to temperature. The δSiOH mode is at about 1150 cm^{-1} at ambient conditions. There is no coupling of δSiOH to tetrahedral stretching modes. However, the SiOH decreases in wavenumber by about 300 cm^{-1} when temperature is increased to 1000 K, which promotes coupling with the ν_3^{TET} mode. The NMA δSiOH frequencies from gas-phase calculations are 300 cm^{-1} lower than NMA with solvation environment. In the gas-phase case, the δSiOH modes and their Raman contribution falls into the region of tetrahedral stretching. For this reason, comparison of gas-phase NMA frequencies and Raman intensities of hydrous silica species in the range of 800 cm^{-1} to 1000 cm^{-1} to experiment may be misleading.

Chapter 4

Vibrational properties of silica species in MgO-SiO_2 glasses

Published in a similar version as :
Spiekermann, **G**., Steele-MacInnis, M., Kowalski, P. M., Schmidt, C., Jahn, S. (2012)
Vibrational properties of silica species in MgO-SiO_2 glasses obtained from ab initio molecular dynamics
Chemical Geology, in press, doi: 10.1016/j.chemgeo.2012.08.020

4.1 Abstract

We report the vibrational properties of silica species in magnesio-silicate glasses, obtained from ab initio molecular dynamics. The mode-projection method employed in this study decomposes the vibrational density of states of silica species into subspectra resulting from normal-mode-like vibrations of mainly two fundamental structural subunits: the SiO_4^{4-} tetrahedron and the Si-O-Si bridging oxygen (BO). This decomposition reveals the mode-specific frequency shifts as a function of tetrahedral polymerization. The method is validated by application to crystalline Mg_2SiO_4 at 300 K, and by comparison to results obtained from normal mode analysis (NMA). Our main findings are: (1) The frequency of the spectroscopically important tetrahedral symmetric stretching mode ν_1^{TET} of Q^1- to Q^4-species is in general lower than commonly assumed. The Q^2-species shows a double instead of a single peak. (2) The BO asymmetric stretching mode ν_3^{BO} contributes to the vibrational density in the region 900-1200 cm^{-1}. If this contribution is not considered in the fitting of Raman intensity in the high-frequency region between 800 cm^{-1} and 1200 cm^{-1} and spectra are explained by tetrahedral contributions of Q^n-species only, then the degree of polymerization of a glass is likely to be overestimated. (3) The $Si_2O_7^{6-}$ dimer, which is an important structural unit in silica-poor MgO-SiO_2 glasses, possesses a specific ethane-like symmetric stretching vibration at about 935 cm^{-1}.

4.2 Introduction

Knowledge about the molecular structure of MgO-SiO_2 glasses is important for geosciences because the system MgO-SiO_2 is the simplest (binary) approximation to model the composition of the Earth's mantle, and ultramafic and mafic liquids. MgO-SiO_2 glasses are also simple analogs for technologically important glasses that commonly involve several network-forming, network-modifying and/or intermediate cation components (Neuville and Mysen, 1996; Neuville et al., 2008; Henderson et al., 2009; Neuville et al., 2010). For these reasons, the structural properties of MgO-SiO_2 glasses and melts have been investigated extensively (Wasserman et al., 1993a,b; Kohara et al., 2004; Voronko et al., 2006; Lacks et al., 2007; Mysen, 2008; Adjaoud et al., 2008; Sen and Tangeman, 2008; de Koker et al., 2008; Kalampounias et al., 2009; Nasikas et al., 2011); also see Mysen and Richet 2005, and references therein). The most common techniques used in experimental investigation of molecular structure of glasses are x-ray diffraction, nuclear magnetic resonance (NMR), x-ray absorption techniques (EXAFS and XANES) and vibrational spectroscopy (McMillan, 1984; McMillan et al., 1992; Kroeker and Stebbins, 2000; Wilding et al., 2004; Mysen and Richet, 2005; Wilding et al., 2008). Among these techniques, vibrational spectroscopy is especially useful for in situ investigation at high pressures and temperatures.

The fundamental structural units of MgO-SiO_2 glasses are SiO_4^{4-} tetrahedra and four- to sixfold coordinated magnesium (Mysen and Richet, 2005). The SiO_4^{4-} tetrahedra are connected to each other in a state of polymerization that depends on the compositional and thermal history of the glass. The state of polymerization of a glass (represented by Q^n species distribution, where Q^n represents a tetrahedron with n BO, see Mysen and Richet 2005) is of particular interest. Polymerization significantly influences glass properties, e.g. viscosity and entropy of mixing (Mysen and Richet, 2005). However, polymerization of MgO-SiO_2 melts and glasses is not entirely understood from a theoretical or observational standpoint. For example, in experimental studies of Mg_2SiO_4 glass under similar conditions, Nasikas et al. (2011) did not report any polymerization of silica, while Kalampounias et al. (2009) reported significant polymerization up to Q^3.

Besides NMR, Raman spectroscopy is a technique that is especially sensitive to the state of polymerization of a silicate glass. The sensitivity of Raman spectroscopy to polymerization results from that fact that each observable vibrational frequency originates from a specific molecular subunit in a specific molecular environment. For instance, the SiO_4 tetrahedra in different Q^n species have similar vibrational motions, but the vibrations occur at different frequencies depending on the degree of polymerization

(McMillan, 1984). For example, the 870 cm^{-1} band has been assigned to the symmetric stretching vibration v_1^{TET} of Q^0 tetrahedra, those at 900 cm^{-1} and 1060 cm^{-1} to v_1^{TET} of Q^1 (McMillan, 1984) and Q^3 (Kalampounias et al., 2009), respectively. Other tetrahedral vibrational modes also shift in frequency with changing polymerization. Similarly, the vibrational frequencies of the bridging oxygen (BO) atoms reflect the degree of polymerization.

Assignment of spectroscopic features (e.g., Raman bands) to the associated vibrational modes of particular molecular subunits is often complicated by lack of direct evidence linking the spectroscopic data to atomic-scale structural data. In such situations, an interpretation of the molecular glass structure based on Raman measurements may be ambiguous. For example, there have been widely varying structural interpretations of MgO-SiO_2 glasses based on Raman spectroscopy (Kalampounias et al., 2009; Nasikas et al., 2011). Nasikas et al. (2011) report a new spectroscopic feature at 900 cm^{-1} that has yet to be unequivocally assigned to vibrational modes. These questions pose a significant challenge in experimental spectroscopy of MgO-SiO_2 liquids and glasses. Molecular computations of the vibrational frequencies of structural subunits may assist in the assignment of spectroscopic bands. In the present study we develop an efficient computational method to allow insight into the structurally localized origin of vibrational frequencies for a broad range of structures of MgO-SiO_2 liquids and glasses.

Various methods can be used to calculate vibrational properties of structurally disordered matter such as silicate glasses. Traditionally, ab initio gas-phase normal-mode analysis (NMA) allows to calculate (1) the vibrational frequencies of each normal mode of small silicate molecules at zero Kelvin and (2) their Raman scattering intensities (Lasaga and Gibbs, 1988; Kubicki and Sykes, 1993; Tossell, 2005). The lack of structural environment in gas-phase NMA may be accounted for by including polarizable continuum models (Tomasi et al., 2005). In practice, NMA establishes a direct link between vibrational frequency and structural origin only in small clusters of low degree of polymerization.

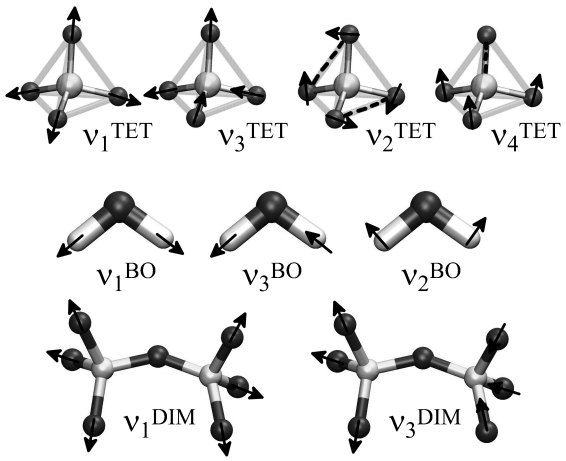

Fig. 4.1: The quasi-normal modes (QNMs) considered in this study. Top row: QNMs of a tetrahedral molecule of symmetry T_d. From left to right: v_1^{TET} (symmetric stretch), v_3^{TET} (asymmetric stretch), v_2^{TET} (symmetric bending, here and elsewhere referred to as "E-bending") and v_4^{TET} (asymmetric bending, here and elsewhere referred to as "umbrella"-bending). Arrows indicate the velocity component of interest. Dashed lines in bending modes represent additional projection vectors where a second projection is necessary (Chapter 2). Middle row: The bridging oxygen (BO, symmetry C_{2v}) QNMs. From left to right: Symmetric stretch (v_1^{BO}), asymmetric stretch (v_3^{BO}) and bending (v_2^{BO}). Bottom row: Two ethane-like QNMs of the Si_2O_7 dimer: v_1^{DIM} and v_3^{DIM}. Parts of the Figures were drawn using the *VMD* software package (Humphrey et al., 1996)

Raman spectra of bulk silicate glasses can be calculated by two fully ab initio methods. For the first method, the polarizability tensor is calculated by the application of a finite electric field to a bulk cell molecular dynamics (MD) run (Putrino and Parrinello, 2002; Giacomazzi et al., 2009). The autocorrelation of its time-series and subsequent Fourier transform yield a Raman spectrum. The second method is to calculate a Raman spectrum using a perturbational approach (Umari et al., 2001; Giacomazzi et al., 2009). In this case, the variation of the polarizability tensor is calculated for finite displacement of all atoms. Both ab initio methods yield a Raman spectrum of a complete structural model, but cannot isolate the specific vibrations of the molecular species in the model. Therefore, these methods are not designed to extract the direct relationship between vibrational frequency and its structural-modal origin.

Raman spectra can also be calculated using a classical approach, by implementing a bond polarizability (BP) model (for a recent review see e.g. Bougeard and Smirnov 2009). The BP model "assembles" a change-in-polarizability tensor of a complete cell by considering deviations of pairwise bond displacement vectors from their bond equilibrium vectors. It can be applied to MD runs or NMA eigenvectors. This method has been applied to calculate Raman spectra of silica polymorphs (Umari et al., 2001; Liang et al., 2006; Bougeard and Smirnov, 2009) and silica glass (Zotov et al., 1999; Giacomazzi et al., 2009). With the BP model, it is also possible to study the partial Raman spectra of individual silica Q^n species in a partially broken silicate network such as Na_2O-SiO_2 NS4 glass (Zotov et al., 1999). However, to our knowledge, it has not yet been applied to weakly polymerized glasses, and the available BP model parameterizations do not seem to yield satisfactory results.

The mode-projection velocity auto-correlation function (VACF) method is well suited to assist band assignment in silicate glasses. This method decomposes the complete vibrational density of states of a glass into vibrational subspectra resulting from characteristic vibrations of well-defined structural subunits such as the tetrahedra. The spectral decomposition of a vibrational spectrum into its different structural and modal origins requires an appropriate selection mechanism. This is achieved by projecting single-particle vectors (either atomic velocities from MD or displacement vectors from bulk NMA) onto the vectors representing the normal-mode-like motion of atoms within the structural subunits, for example the ${SiO_4}^{4-}$ tetrahedron. The mode-projection method has been applied to molecular water (Bopp, 1986; Kalinichev and Heinzinger, 1995), network forming salts (Pavlatou et al., 1997), fully polymerized silica (Wilson and Madden, 1996; Taraskin and Elliott, 1997; Sarnthein et al., 1997) and recently to silica species in aqueous fluids (Chapter 2). Comparison of the resulting subspectra peak frequencies to experimental bands provides a reliable basis for assignment of spectroscopic features to molecular species. This approach exploits the fact that (1) Raman scattering frequencies represent directly the vibrational frequencies of the sample (Umari et al., 2001, 2003; Veithen et al., 2005; Giacomazzi et al., 2009), and (2) vibrations of the silica species in any degree of polymerization are normal-mode-like, i.e., similar to the vibrations of the isolated species, but shifted in frequency. The mode-projection method has the important drawback that it cannot compute relative Raman scattering intensities. However, in this study we focus on modal vibration whose importance in Raman scattering has been demonstrated for small silica clusters (for tetrahedral modes see Lasaga and Gibbs 1988; De Almeida and O'Malley 1991; Zotov and Keppler 2000; Hunt et al. 2011; McIntosh et al. 2011, for Si-O-Si contributions see Lasaga and Gibbs 1988; Zotov and Keppler 2000; Hunt et al. 2011).

In this study, we investigate several MgO-SiO_2 glass models. The structure of our glass models is validated against recent x-ray structure factors (Wilding et al., 2004, 2008). Vibrational subspectra are presented for Q^0 (i.e., ${SiO_4}^{4-}$ monomers) to Q^4 tetrahedral species, for the ${Si_2O_7}^{6-}$ dimer, and for BO atoms in any degree of polymerization. The method successfully reproduces vibrational frequencies of well-known modes (e.g., the symmetric stretch of the silica monomer). Based on the present results, new conclusions can be drawn for band assignment in MgO-SiO_2 glasses.

Table 4.1: Overview of the simulation runs. The densities were calculated from on the basis of experimental data (Lange and Carmichael, 1987). Number of atoms indicated in parenthesis.

structure	T (K)	cell (Å)	mol. V (cm^3/mol)	nom.[1] Q^n	av.[2] Q^n
forsterite (112)	300	9.5x10.3x11.9	43.8	0.0	0.0
glassy Mg_2SiO_4 (112)	1000	11.1x11.1x11.1	52.3	0.0	0.60
glassy $MgSiO_3$ (160)	1000	12.7x12.7x12.7	38.9	2.0	2.29
glassy $MgSi_2O_5$ (144)	1000	12.7x12.7x12.7	68.5	3.0	3.04

[1] nominal average Q^n number, based on stoichiometry
[2] actual average Q^n number in the MD simulation

4.3 Methods

Ab initio molecular dynamics

We used density functional theory (Kohn and Sham, 1965) in the plane wave pseudopotential approach, as implemented in the *Car-Parrinello Molecular Dynamics (CPMD)* code (Marx and Hutter, 2000), with the Perdew-Burke-Ernzerhof (PBE) exchange-correlation functional (Perdew et al., 1996) and Martins-Troullier type pseudopotentials to describe the core electrons (Troullier and Martins, 1991). The Kohn-Sham wavefunctions were expanded at the Γ-point with a cutoff energy of 80 Ry. We determined that the dependence of forces on k-point sampling is below 1% and therefore negligible. For the molecular dynamics simulations we used Car-Parrinello molecular dynamics (Car and Parrinello, 1985) with a ficticious electronic mass of 400 atomic units (a.u.) and a time step of 4 a.u. (0.097 fs).
To model MgO-SiO_2 glasses, we performed simulation runs on Mg_2SiO_4, $MgSiO_3$ and $MgSi_2O_5$ glass (Table 4.1). This included several tetrahedra in each of the possible Q^n speciations (Q^0 to Q^4). The vibrational properties investigated here are quasi-localized in space and therefore not sensitive to any finite size effect related to our model sizes of 112 to 160 atoms. The temperature of glass simulations was 1000 K. In addition, we modeled crystalline forsterite (Mg_2SiO_4) at 300 K to benchmark our method against a known structure. The simulations were performed at constant molar volumes based on experimental values ((Lange and Carmichael, 1987); Table 4.1).
To obtain good representations of the glasses, we first ran classical MD simulations for 50 ps at 3000 K using the classical advanced ionic model (AIM; (Jahn and Madden, 2007)). Subsequently, we quenched the melts instantaneously from 3000 K and ran MD simulations for additional 200 ps at 1000 K. Then we performed the ab initio MD runs of 30 ps each.

Table 4.2: Structural description of the three glassy simulation runs in terms of Q^n-species distribution. Values in parenthesis indicate the number of Q^n-species considered for the evaluation of vibrational subspectra.

composition	Q^0	Q^1	Q^2	Q^3	Q^4
Mg_2SiO_4	0.44(7)	0.50(8)	0.06(1)	–	–
$MgSiO_3$	–	0.20(5)	0.39(12)	0.33(9)	0.08(1)
$MgSi_2O_5$	–	–	0.20(6)	0.56(17)	0.24(5)

Decomposition of the vibrational spectrum

The mode-projection method is based on the observation that the high-frequency quasi-localized vibrational motions of structural subunits of silica networks remain normal-mode-like throughout the different degrees of polymerization, although the frequencies of these vibrations change with the degree of polymerization. Therefore, to uncover these frequency changes in different environments, the mode-projection method distributes the vibrational density of states among the various quasi-normal vibrational

modes (quasi-normal modes, QNMs). In doing so, the particle motion projection decomposes the complete vibrational spectrum into well-defined subspectra. We follow the general outline of Pavlatou et al. (1997) and Taraskin and Elliott (1997), and the detailed description of the methods is given in Chapter 2. The power spectrum of a group of atoms is calculated via the Fourier transform of their velocity autocorrelation function (VACF)

$$F(\omega) = \int_0^{t_{max}} cos(\omega t) dt \langle v_k(t) \cdot v_k(0) \rangle, \tag{4.1}$$

where $F(\omega)$ is the spectral density and ω is the angular frequency, and chevrons indicate the ensemble average (Allen and Tildesley, 1987). Without the mode-projection method, the spectrum resulting from equation 4.1 would be the complete vibrational density of states, including translational, rotational and low-frequency long-range acoustic-like contributions. However, these contributions do not give spectral information that can be interpreted in terms of a state of polymerization of a glass. Instead, the high-frequency, quasi-localized vibrations of the molecular subunits directly reflect the degree of polymerization. Therefore, the spectroscopically distinct contributions of the local environment (e.g. the type of Q^n-species) must be isolated from the complete vibrational density of states. Projection of atomic motions onto QNMs isolates the spectroscopically distinct contributions, because the quasi-local vibrations behave like the molecular normal-modes based strictly on symmetry (Sen and Thorpe, 1977; Pavlatou et al., 1997; Taraskin and Elliott, 1997). A $SiO_4{}^{4-}$ tetrahedron has T_d symmetry and nine normal modes that can be grouped into four modes with degeneracies: (1) symmetric stretch (ν_1^{TET}), (2) asymmetric stretch (ν_3^{TET}), (3) E-bending (ν_2^{TET}, also named symmetric bending) and (4) "umbrella"-bending (ν_4^{TET}, also called asymmetric bending). The QNMs used in the projection approximate the four Raman-active normal modes, thus making isolation of quasi-local vibrations computationally tractable (Fig. 4.1, top row, and Table 4.3) (Pavlatou et al., 1997; Taraskin and Elliott, 1997), see also Chapter 2.

In the first step of the mode-decomposition procedure, for each configuration of the MD trajectory, the velocities of individual silicon atoms are subtracted from the velocities of each of the four oxygens of the respective $SiO_4{}^{4-}$ tetrahedron. This eliminates the low-frequency translational contributions. In the second step, the velocity of each of the four oxygens is projected onto the appropriate vector representing the QNM of interest (Fig. 4.1). Once the atomic velocities have been projected onto the appropriate vectors, the projected velocities are summed and/or subtracted in various ways to record the normal-mode-like vibrations (see Chapter 2 for a complete description of the equations used to represent tetrahedral and other normal modes). This procedure is repeated at every timestep of the MD run. The resulting time series of single "mode-projection magnitude" values is subsequently autocorrelated and Fourier transformed using equation 4.1. After repeating this procedure for all considered tetrahedra, the spectral densities of locally identical tetrahedra (i.e. same Q^n-speciation) are grouped together and averaged. The finals result are the four modal "subspectra" for every Q^n-species. The choice of the silicon atom as reference center of the QNM is justified because the velocity of each oxygen atom represents part of a vibration of the Si-O bond. The center-of-mass of the tetrahedron can also be used as the center of the projection, and the results are mostly identical (Fig. 4.2). However, both choices transmit in a minor amount the spectral density of one QNM into the spectral density of another QNM. This occurs through the vibrational rattling of the silicon around the center-of-mass (Fig. 4.2). Henceforward, we use the silicon atom as reference center of the QNMs.

The vibrations of the BO are treated similarly, assuming the oxygen as the center atom of the structural subunit Si-O-Si with C_{2v} symmetry (H_2O-like, Fig. 4.1). This gives three QNMs: Symmetric stretch, asymmetric stretch and bending (Table 4.3) (Taraskin and Elliott, 1997), also in Chapter 2. The C_{2v} concept of the bridging oxygen is insensitive to the torsional motions of the adjacent tetrahedra, which do not affect the vibrational spectra. Other alternative ways to categorize BO vibrations are described in Chapter 2. The $Si_2O_7{}^{6-}$ dimer has a unique mirror symmetry allowing an ethane-like set of QNMs (Fig. 4.1). Among these, we consider only the inter-tetrahedral symmetric stretch and asymmetric stretch

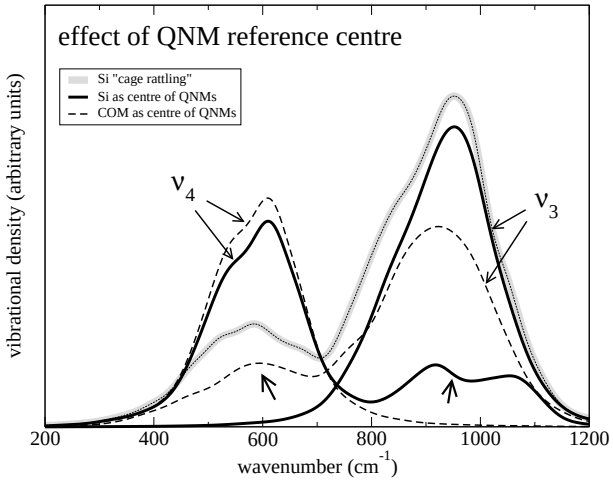

Fig. 4.2: The spectrum of the silicon atom rattling around the center-of-mass of the tetrahedron (grey). For ν_3^{TET} and ν_4^{TET}, we demonstrate the difference in spectral density caused by using either the silicon or the tetrahedral center-of-mass (COM) for the projection reference center. The choice of silicon as reference center introduces an artificial high-frequency contribution to ν_4^{TET} (right short arrow), whereas the choice of the center-of-mass as reference center causes an artificial low-frequency contribution to ν_3^{TET} (left short arrow). The silicon as reference center is used throughout this study.

(Table 4.3). The C_{2v} symmetry described above for Si-O-Si is also applied to the two O-Si-O pairs on Q^2 tetrahedra, where one pair includes the two BO atoms and the other pair includes the two non-bridging oxygens (NBO).
The resulting spectra of any of the modes described above have a full width at half maximum of more than 150 cm^{-1}. This large width is a consequence of finite sampling time. Also, the raw spectral density, without treatment, is not a smooth curve (Section 3.2, below). For simpler visual inspection, we smooth the spectral densities in all Figures through a convolution with a Gaussian of σ=20 cm^{-1}. In the case of the tetrahedral asymmetric stretch of forsterite at 300 K, the vibrational sampling of all possible states did not reach convergence, thus requiring a Gaussian of σ=40 cm^{-1} for smoothing.

Normal Mode analysis (NMA)

Calculation of NMA frequencies was carried out as follows. 300 configurations from the 30 ps glassy Mg_2SiO_4 MD trajectory were chosen, each separated by 0.1 ps. We relaxed the positions of the atoms of interest (a single SiO_4^{4-}, in a second procedure a single $Si_2O_7^{6-}$), keeping all other atoms fixed. NMA was then carried out for the relaxed monomer (and later dimer). This procedure was repeated for all chosen configurations. We calculated a frequency "density curve" (a histogram with a slot width of 10 cm^{-1}) from all NMA results (bars in Figs. 4.5 and 4.6). By sampling 300 different configurations, this procedure appropriately accounts for the disordered environment around the SiO_4^{4-} monomer and $Si_2O_7^{6-}$ dimer.

4.4 Results

Structural validation

All modeled structures are glassy at 1000 K. Therefore, their structure did not fluctuate significantly during the MD runs. The average degree of polymerization of each run is given in Table 4.1, the Q^n-

Table 4.3: The quasi-normal modes (QNMs) discussed in this study. The symmetry of the structural unit and the mode is indicated in brackets. Other modes exist, but are less important in spectroscopy (see Chapter 2).

Mode:	applied to:	abbreviation:	Figure:
tetrahedral QNMs (T_d):			
symmetric stretch (A_1)	any Q^n-species	ν_1^{TET}	4.7,4.5
asymmetric stretch (F_2)	any Q^n-species	ν_3^{TET}	4.8,4.5
E-bending (E)	any Q^n-species	ν_2^{TET}	4.5
umbrella-bending (F_2)	any Q^n-species	ν_4^{TET}	4.5
ethane-like QNMs (D_{3d} or D_{3d}):			
symmetric stretch (A_1)	dimer	ν_1^{DIM}	4.6
asymmetric stretch (B_2)	dimer	ν_3^{DIM}	4.6
Si-O-Si QNMs (C_{2v}):			
Si-O-Si symmetric stretch (A_1)	bridging oxygen	ν_1^{BO}	4.10
Si-O-Si asymmetric stretch (B_2)	bridging oxygen	ν_3^{BO}	4.11
Q^2 pairwise QNMs (C_{2v}):			
Q2 NBO pair symmetric stretch (A_1)	Q^2 NBO pair	–	4.9
Q2 NBO pair asymmetric stretch (B_2)	Q^2 NBO pair	–	4.9
Q2 BO pair symmetric stretch (A_1)	Q^2 BO pair	–	4.9
Q2 BO pair asymmetric stretch (B_2)	Q^2 BO pair	–	4.9

species distribution is given in Table 4.2. The degree of polymerization of all models is higher than the nominal value based on stoichiometry. This is consistent with the results of several experimental and computational studies (Karki, 2010; Kalampounias et al., 2009; Sen and Tangeman, 2008). Even Q^4-species have been observed in enstatitic melt in previous studies (Karki, 2010). A few edge-sharing tetrahedra (i.e., twofold silica rings) were observed in the $MgSi_2O_5$ model. They formed through the transitionary stage of fivefold coordination. Fivefold silicon was therefore observed in minor amounts as transient species, as has been observed in at least one other ab initio MD study of silica at ambient pressure (Trave et al., 2002). Free O^{2-} atoms (i.e., oxygens with no nearest silicon neighbor) were also present, as has been previously observed experimentally (Kalampounias et al., 2009; Nesbitt et al., 2011), but they are not of interest in the vibrational analysis. This is because the non-directional ionic bonding of free O^{2-} to the surrounding magnesium is very weak, and therefore the resulting vibrational frequencies are significantly lower than (and do not interfere with) the frequencies of the Si-O network. Hereafter, the spectra of structurally identical tetrahedra (in terms of Q^n-speciation) or identical BO atoms (same combination of adjacent Q^n-speciation) from the three different modeled systems (Table 4.1) were grouped and averaged. This "stacking" of results from different tetrahedra of the same Q^n status eliminates random fluctuations of spectral densities. These inevitable random fluctuations arise from structural disorder in the glass, which furnishes each tetrahedron with a different chemical environment (e.g. Si-O-Si bending angles, ring sizes, proximity of magnesium atoms, etc.). The temperature is too low and the MD run lengths too short in order to sample the entire configurational space of a single tetrahedron of each Q^n status. Therefore, the averaging over all tetrahedra of each Q^n-species is an appropriate way to overcome this problem and to work out their Q^n-specific vibrational contribution.
We performed structural validation of two representative MD structures by comparison to experimental data, to determine whether the MD runs are reasonable representations of MgO-SiO_2 glasses. The x-ray weighted structure factor S(Q) was determined from partial structure factors $S_{\alpha\beta}(Q)$,

$$S(Q) = \frac{1}{\sum_\alpha N_\alpha f_\alpha^2(Q)} \sum_{\alpha\beta} \sqrt{N_\alpha N_\beta} f_\alpha(Q) f_\beta(Q) S_{\alpha\beta}(Q), \tag{4.2}$$

where α and β stand for Mg, Si and O, and $N_{\alpha,\beta}$ is the total number of ions of type α and β, respectively. The form factors $f_\alpha(Q)$ of magnesium and silicon are taken from Cromer and Waber (1974), the form

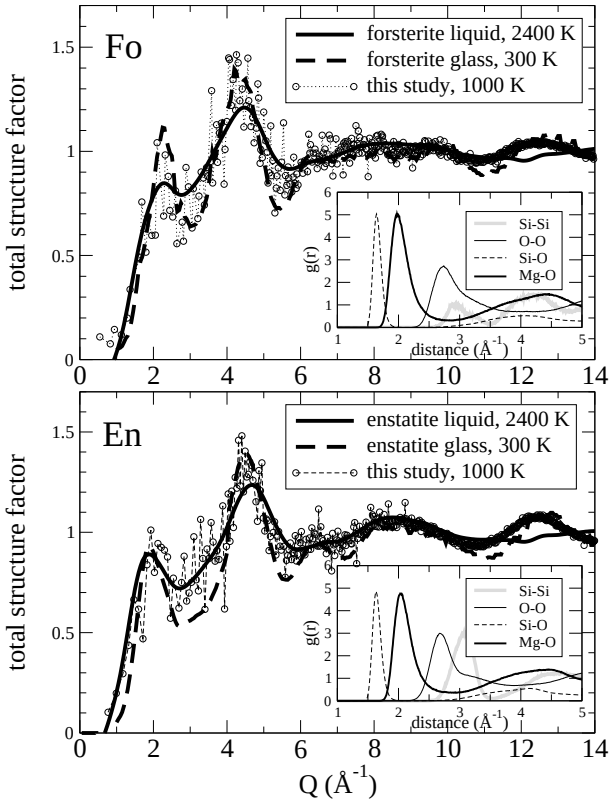

Fig. 4.3: Comparison of calculated total x-ray structure factor S(Q) of Mg_2SiO_4 (above) and $MgSiO_3$ (below) to the experimental data from Wilding et al. (2004) for glass and from Wilding et al. (2008) for liquid. Insets: Pairwise radial distribution functions g(r). The one for Si-O has been downscaled by a factor of 3 in both insets.

factor of oxygen is from Tokonami (1965).

In Fig. 4.3, the calculated total x-ray structure factors S(Q) from the ab initio MD simulations are compared to experimental structure factors of Mg_2SiO_4 and $MgSiO_3$ glasses at 300 K (Wilding et al., 2004) and liquids at 2400 K (Wilding et al., 2008). The structure factors of silicate melts are not very sensitive to temperature changes (Fig. 4.3; see also Wilding et al. 2008). The results are in good agreement with experimental structure factors. The calculated structure factor of Mg_2SiO_4 is intermediate between the experimental glass and liquid structure factors where they differ most (at Q=3.0 Å^{-1} and Q=5.5 Å^{-1}). In the case of $MgSiO_3$, our structure factor is closer to the liquid state than to the glass. This is as expected because molecular models of polymerized silicate glasses often have a very high fictive temperature and result in “frozen-in" liquid-like structure different from that of a glass (see e.g. Drabold 2009). This behavior is only revealed by structure factors. The radial distribution functions (RDF) are plotted in the insets in Fig. 4.3. Their maxima reflect the mean pair distance of 2.00A for Mg-O in forsterite glass; 2.05A for Mg-O in enstatite glass; and 1.64A for Si-O in both forsterite and enstatite glass. These values are consistent with experimental values at room temperature of 2.1 Å and 1.6 Å for a forsterite glass from Kohara et al. (2004), and of 2.0 Å and 1.64 Å for glasses between Mg_2SiO_4 and $MgSiO_3$ from Wilding et al. (2010). Vuilleumier et al. (2009) obtained from ab initio MD of an enstatite melt the values of 2.0 Å and 1.64 Å. For all three glasses, we calculated the magnesium coordination number by counting the oxygen atoms within a sphere of diameter 2.84 Å around each magnesium, which is the position of the first minimum in the Mg-O radial distribution function. We find the average coordination to be close to 5.0 in all runs, with major magnesium fractions being fourfold and sixfold coordinated. It has

been suggested that the Mg-coordination changes from about 5.0 in Mg_2SiO_4 to about 4.0 in $MgSiO_3$ (Wilding et al., 2004). We do not observe this transition in our simulations.

Benchmarking of QNM subspectra

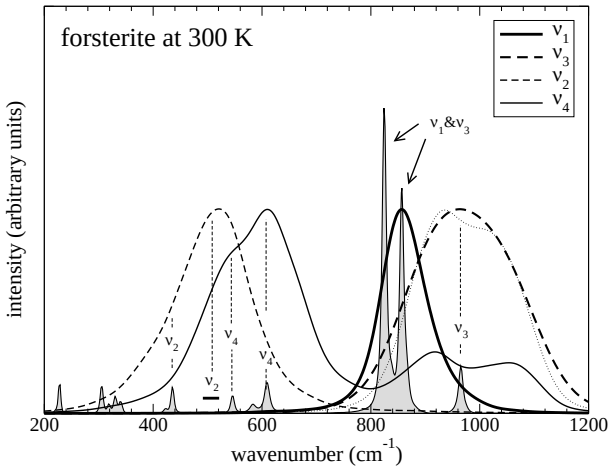

Fig. 4.4: Comparison of the four tetrahedral QNMs ν_1^{TET} to ν_4^{TET} to an unpolarized Raman spectrum of crystalline Mg_2SiO_4 (spectrum X050080 from Downs 2006, parallel to c-axis). The assignment of Raman bands follows the assignment by Chopelas (1991), Noel et al. (2006) and McKeown et al. (2010). All tetrahedral QNM subspectra peak frequencies are in good agreement with experimental bands. The calculated ν_2^{TET} spectrum shows a maximum that does not agree with Raman bands, but it agrees well with vibrational frequencies in the ν_2^{TET} densely populated region around 525 cm^{-1} (Noel et al., 2006). Note that ν_3^{TET} has been convoluted with a Gaussian of σ=40 cm^{-1} instead of the usually employed σ=20 cm^{-1} to account for unconverged results due to improper occupation of vibrational states at 300 K. Its convolution with a Gaussian of σ=20 cm^{-1} is shown by the thin dotted line.

We benchmark and test the predictive power of the mode-projection method in two ways. Firstly, we apply the method to crystalline forsterite at 300 K and compare the results to an experimental Raman spectrum of synthetic forsterite. Secondly, we compare our QNM results for Q^0 monomers and Q^1-Q^1 dimers to NMA results of the same structures. We scaled the spectrum height of the QNMs to unity in all Figures where the results of different QNMs are plotted together. This is because the method of calculation is different for every mode and therefore spectral densities of different QNMs cannot be compared to each other. However, the spectral intensity of identical QNMs can be compared between different degrees of polymerization, e.g. the spectral densities of ν_2^{TET} can be compared between Q^0 and Q^1.

The results of the application of our method to forsterite at 300 K are the tetrahedral ν_1^{TET} to ν_4^{TET} subspectra compared to unpolarized experimental Raman bands of forsterite (Fig. 4.4, spectrum X050080 from Downs 2006, parallel to c-axis). The assignment of modes to the experimental Raman spectrum follows Chopelas (1991) and McKeown et al. (2010). Forsterite shows three tetrahedral stretching bands at 826 cm^{-1}, 857 cm^{-1} and 966 cm^{-1} (Chopelas, 1991; Voronko et al., 2006; McKeown et al., 2010). The band at 966 cm^{-1} is unanimously assigned to ν_3^{TET}, whereas the other two are mixed in character of ν_1^{TET} and ν_3^{TET}. There are slight differences in the literature about which vibrational character is the dominating one in the 826 cm^{-1}, 857 cm^{-1} bands (Iishi, 1978; Chopelas, 1991; Kolesov and Geiger, 2004; Voronko et al., 2006; McKeown et al., 2010). In agreement with the computational results of McKeown et al. (2010), we consider that the band at 857 cm^{-1} is the band that is most ν_1^{TET} in character.

A scaling factor for all vibrational frequencies is necessary to account for the systematic error of the density functional theory (DFT), as is employed in this Chapter and in Chapter 2. For the derivation of this scaling factor, we consider two experimental bands: The predominantly ν_1^{TET} at 857 cm^{-1} and the ν_3^{TET} at 966 cm^{-1}. The peak frequency of our ν_1^{TET} QNM is at 814 cm^{-1} (Table 4.4). The ν_3^{TET} QNM spectrum shows a double peak (thin dotted line in Fig. 4.4) which is a result of incomplete sampling of vibrational states due to low temperature and finite MD run length. To overcome that deficiency, we apply a Gaussian of σ=40 cm^{-1} in the convolution. Its peak frequency is 916 cm^{-1} (Table 4.4). To scale both QNM peak frequencies to match the experimental band frequencies (Table 4.4), a scaling factor of 1.053 is required. We consider this agreement as an indication for the correctness of this factor. Frequency-lowering anharmonic effects and frequency-increasing environment probably counterbalance, such that the magnitude of the factor is in good agreement with the recommended PBE scaling factors for vibrational frequencies below 1500 cm^{-1} (Merrick et al., 2007). This scaling factor is applied to all results, including to the NMA results in Figs. 4.5 and 4.6.

The asymmetric bending vibration ν_4^{TET} ("umbrella" bending) shows a main peak at 612 cm^{-1} and a minor peak at about 542 cm^{-1}. They are in agreement with experimental Raman bands assignment of ν_4^{TET} at 608 cm^{-1} and 545 cm^{-1} (Chopelas, 1991). The calculated ν_2^{TET} spectrum has a peak at 522 cm^{-1}. There is no corresponding experimental Raman band. However, the region around 525 cm^{-1} in forsterite is densely populated by vibrational modes, as has been shown by an ab initio NMA study (Noel et al., 2006). A shoulder of the ν_2^{TET} spectrum at about 400 cm^{-1} agrees with a ν_2^{TET}-assigned Raman band at 410 cm^{-1}. The mode-projection method thus accurately reproduces the vibrational frequencies of crystalline forsterite, including the low-frequency bending modes ν_2^{TET} and ν_4^{TET}.

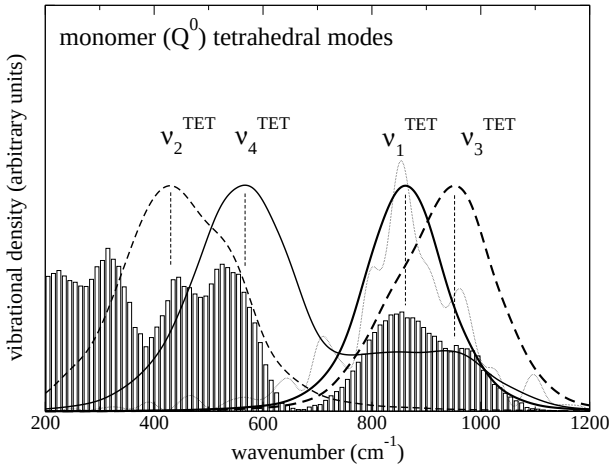

Fig. 4.5: The monomer vibrations result in four tetrahedral QNM subspectra (ν_1^{TET} to ν_4^{TET}). They are compared to the NMA frequency histogram. The thin dotted line near the ν_1^{TET} is the raw spectrum of a single Q^0 monomer before convolution. This demonstrates the coherence between the individual subspectra and their average over all Q^0.

We next compare the QNM spectral densities of the SiO_4^{4-} monomer and the $Si_2O_7^{6-}$ dimer in forsterite glass to frequencies that were explicitly calculated using normal mode analysis (NMA, see Subsection 4.3) (Figs. 4.5 and 4.6). The SiO_4^{4-} monomer NMA histogram above 400 cm^{-1} shows four peaks that reflect the four tetrahedral normal modes (Fig. 4.5). NMA frequencies below 400 cm^{-1} are "external modes" resulting from SiO_4^{4-} tetrahedral rotations and translations (Noel et al., 2006; McKeown et al., 2010). They are not captured in the mode-projection model and are therefore not considered further. The four NMA peaks are matched by the peak frequencies of the four QNM subspectra. The red-shift between QNM peaks and NMA histogram peaks results from the fact that QNMs are calculated dynamically at

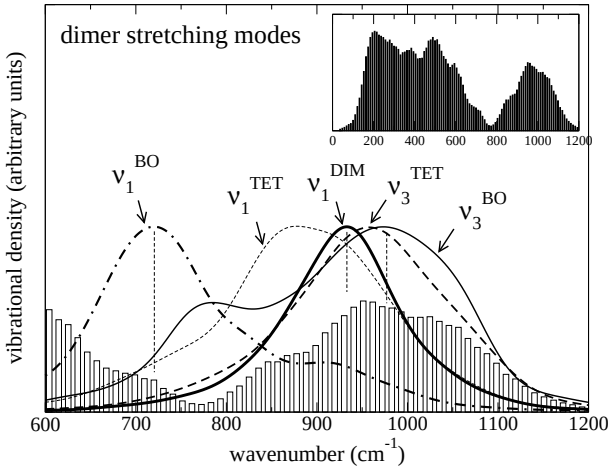

Fig. 4.6: The high-frequency part of the dimer NMA histogram and four QNMs found in the $Si_2O_7{}^{6-}$ dimer that match the NMA frequency density. Note that three modes give high spectral density in the same frequency region between approximately 900 and 1050 cm^{-1}. The inset shows the dimer NMA histogram for the complete frequency range of 0 to 1200 cm^{-1}.

1000 K, whereas the NMA is zero-Kelvin-like. The stretching vibrations ν_1^{TET} and ν_3^{TET} in the NMA histogram overlap significantly. This is a consequence of the disordered ionic environment of the SiO_4^{4-} monomer. The ν_4^{TET} shows a high-frequency contribution in the region of the ν_1^{TET} and ν_3^{TET} stretching QNMs. This is an artifact resulting from the quasi-normal mode approximation neglecting the motion of the central atom (in this case silicon). The motions of the silicon atom are a "rattling" around the center-of-mass of the tetrahedron, as a result of the four normal modes. Thus the silicon "rattling" vibrations (grey in Fig. 4.2) are transmitted into the ν_4^{TET} QNM (Fig. 4.2 and Subsection 4.3).
The $Si_2O_7{}^{6-}$ dimer shows a NMA frequency distribution (Fig. 4.6) which reflects its flexible structure due to variability of the Si-O-Si bonding angle (see e.g. Hunt et al. 2011). The NMA reproduces the experimentally observed gap around 770 cm^{-1} that is present in all Raman spectra of weakly polymerized MgO-SiO_2 glasses (see e.g. Kalampounias et al. 2009). A NMA histogram shoulder between 680 cm^{-1} and 720 cm^{-1} is commonly attributed to bridging oxygen vibrations (Kalampounias et al., 2009; Nasikas et al., 2011). The ν_1^{BO} plots around 720 cm^{-1} and is therefore in good agreement with this assignment. The wide histogram peak around 1000 cm^{-1}, extending from 800 to 1100 cm^{-1}, is matched by four QNMs: Ethane-like ν_1^{DIM}, tetrahedral ν_1^{TET} and ν_3^{TET} and the ν_3^{BO}. The ν_1^{TET} peak is very broad. On the high-frequency branch, this is due to "QNM overlap" (as described in Fig. 4.2) between ν_1^{TET} and ν_1^{DIM} (see Fig. 4.1). The second peak of the ν_3^{BO} spectrum at 780 cm^{-1} is likely caused by a similar overlap from the ν_1^{TET} vibrations. Note that the peak heights between different QNMs should not be compared (see Subsection 4.3). Differences between NMA and QNM frequency results are minor and are explained by relaxation to zero-Kelvin for NMA. Overall, the NMA-to-QNM comparison shows that the decomposition by the mode-projection technique accurately records vibrational frequencies of molecular structures in disordered environment.

Tetrahedral subspectra as a function of Q^n-speciation

The vibrational frequency of the ν_1^{TET} QNM peak increases systematically as the degree of polymerization increases from Q^0 to Q^4 (Fig. 4.7). The ν_1^{TET} shifts from 863 cm^{-1} (Q^0) to 885 cm^{-1} (Q^1), to a double peak of 960 cm^{-1} and 1037 cm^{-1} (Q^2), to 1032 cm^{-1} (Q^3) and to 1080 cm^{-1} (Q^4) (Table 4.4). The reason for this shift is the change in the potential well around the oxygen atoms when they change from non-bridging to bridging oxygen atoms. The origin of the double peak of the Q^2 species can be

understood after studying the ν_3^{TET} QNM and will be discussed below.

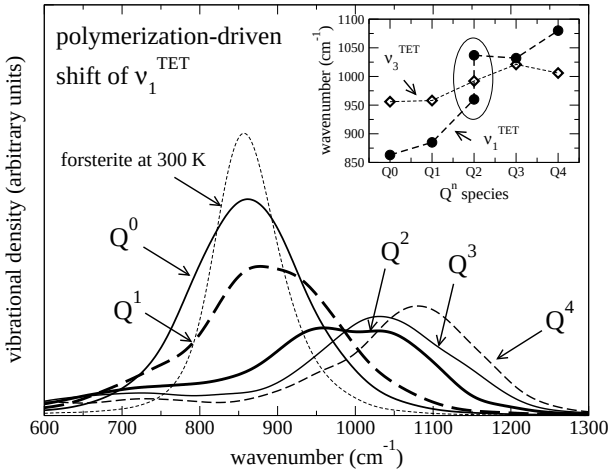

Fig. 4.7: The tetrahedral symmetric stretch (ν_1^{TET}) shifts with increasing polymerization from 863 cm^{-1} (Q^0) to 1080 cm^{-1} for Q^4. The forsterite ν_1^{TET} spectral density has been down-scaled by 0.5 for better visualization. The inset shows the polymerization-driven frequency shift of ν_1^{TET} and ν_3^{TET} from Q^0 to Q^4. The error is estimated to be less than 20 cm^{-1}.

The tetrahedral asymmetric stretching mode ν_3^{TET} shows a similar trend upon increasing polymerization (Fig. 4.8). The peak frequency of Q^0 is 956 cm^{-1}, for Q^1 958 cm^{-1}, for Q^2 992 cm^{-1}, for Q^3 1021 cm^{-1} and for Q^4 it is 1006 cm^{-1}. We estimate the error to be less than 20 cm^{-1} (Section 4.3). There is a frequency crossover of ν_1^{TET} and ν_3^{TET} with increasing polymerization (inset in Fig. 4.7). In the case of Q^0 the ν_3^{TET} is higher than the ν_1^{TET} by 90 cm^{-1}, whereas for Q^4 the ν_3^{TET} is lower than the ν_1^{TET} by almost 80 cm^{-1} (Table 4.4). This frequency crossover explains the origin of the double peak of the Q^2 ν_1^{TET} QNM. In Q^2 tetrahedra, the ν_3^{TET} and the ν_1^{TET} have approximately the same spectrum (Fig. 4.9). The Q^2 ν_1^{TET} and ν_3^{TET} are governed by the non-bridging oxygen (NBO) NBO-Si-NBO pair (C_{2v}) symmetric stretch and asymmetric stretch vibrations. The pair of Q^2 bridging oxygens BO-Si-BO couples to these Q^2 NBO-Si-NBO pair modes, such that the asymmetric stretch of the NBO-Si-NBO pair contributes to the Q^2 tetrahedral ν_1^{TET} spectrum (Fig. 4.9). This leads to the ν_1^{TET} double peak of Q^2 species.

The $Si_2O_7^{6-}$ dimer

The $Si_2O_7^{6-}$ dimer consists of two Q^1 tetrahedra which produce a spectrum of tetrahedral modes, among them the Raman intense ν_1^{TET} at 885 cm^{-1}. But the dimer also shows ethane-like intertetrahedral vibrations (Fig. 4.1), each with specific peak spectral densities (Fig. 4.6). The ν_1^{DIM} is at 935 cm^{-1}, the ν_3^{DIM} at 857 cm^{-1}. It has been shown elsewhere that the dimer ν_1^{DIM} possesses a significant Raman intensity in hydrous environment at high pressures and temperatures (Zotov and Keppler, 2000). The result of 935 cm^{-1} for this QNM agrees well with an experimental band around 940 cm^{-1} in silica-poor MgO-SiO_2 glasses (McMillan, 1984; Kalampounias et al., 2009; Voronko et al., 2006).

The subspectra of bridging oxygens

Figures 4.10 and 4.11 show the ν_1^{BO} and ν_3^{BO} for a wide range of degree of polymerization of the adjacent two tetrahedra. Both QNMs show a polymerization-dependence of the spectrum. However, these spectra are not fully converged and should not be interpreted quantitatively. This is because the Si-O-Si bending degree of freedom strongly influences the frequency of the Si-O-Si vibrations. The glassy structure and

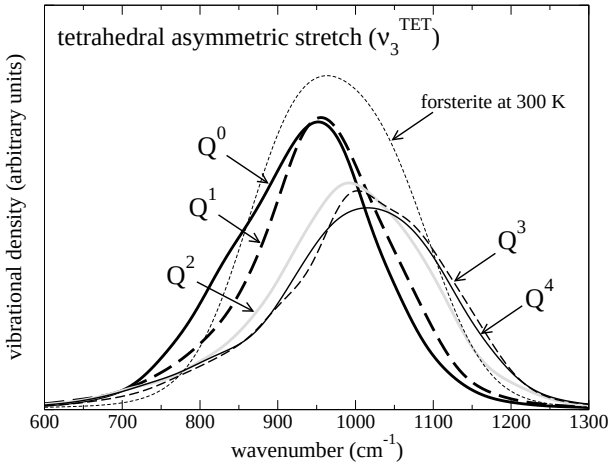

Fig. 4.8: The tetrahedral asymmetric stretch (ν_3^{TET}) shows a systematic trend to higher frequencies when going from Q^0 to Q^4. For peak frequencies see Table 4.4. The result from forsterite at 300 K is shown for comparison.

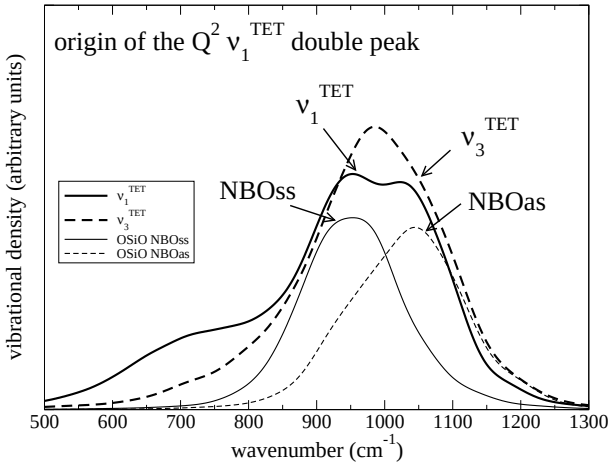

Fig. 4.9: The tetrahedral symmetric stretch and asymmetric stretch of the Q^2 tetrahedra show about the same spectrum. It is explained by the Q^2 NBO-Si-NBO pair modes (symmetric and asymmetric stretch), to which the Q^2 BO-Si-BO pair modes couple.

the limited size of the models do not allow sufficient sampling of all vibrations at the possible Si-O-Si bending states. However, the results can be interpreted qualitatively. With increasing polymerization, the ν_1^{BO} peak shifts from 720 cm^{-1} to lower frequencies for intermediate degrees of polymerization, and then to higher frequencies for high degrees of polymerization. The polymerization-driven frequency increase is more clear for the ν_3^{BO}. With increasing polymerization, the spectrum peak shifts from about 980 cm^{-1} for Q^1-Q^1 to 1040 cm^{-1} for Q^2-Q^2 to about 1100 cm^{-1} for Q^2-Q^4 and Q^3-Q^4. The inset of Fig. 4.10 shows the dependence of the ν_1^{BO} spectrum on the ring size. Whereas the spectra for threefold and fourfold rings are almost identical, the peak shifts remarkably in the highly strained twofold rings, i.e. edge-sharing tetrahedra. The number of twofold rings used for this calculation is three, and therefore results are indicative, although not fully converged.

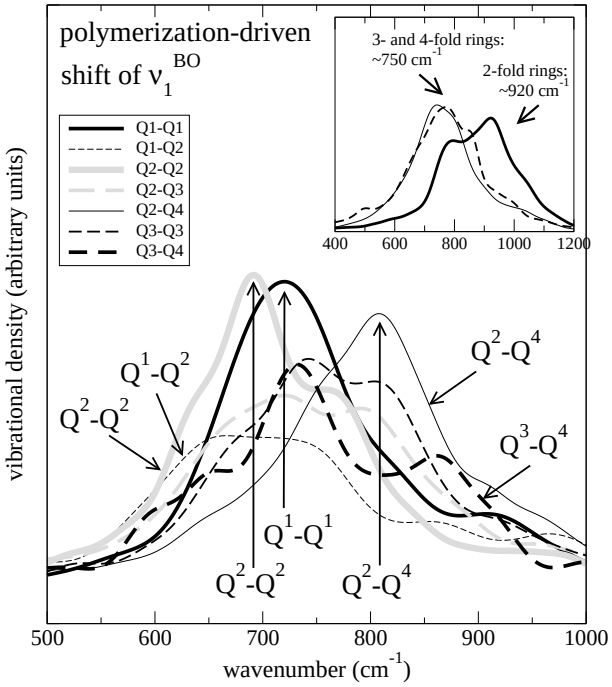

Fig. 4.10: The BO symmetric stretch (ν_1^{BO}) for different degrees of polymerization. The peak frequency generally shifts to higher frequencies with increasing degree of polymerization of the adjacent tetrahedra. However, the frequency of Q^2-Q^2 is lower than for Q^1-Q^1, which indicates a reverse trend at low degree of polymerization. These spectral densities are not fully converged with respect to simulation run length because of the Si-O-Si bending angle degree of freedom. They should therefore be interpreted qualitatively only. Inset: Spectra of ν_1^{BO}, sorted according to the ring size that the BO form part of. Twofold rings refer to edge-sharing tetrahedra.

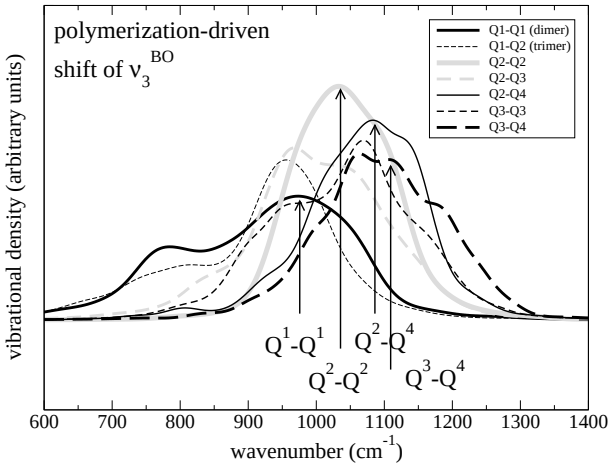

Fig. 4.11: The BO asymmetric stretch (ν_3^{BO}) for different degrees of polymerization. The peak frequency generally shifts to higher frequencies with increasing degree of polymerization of the adjacent tetrahedra. These spectral densities are not converged with respect to simulation run length because of the Si-O-Si bending angle degree of freedom. They should therefore be interpreted qualitatively only.

Table 4.4: Overview over the peak frequencies. Temperature was 1000 K except for crystalline forsterite. A scaling factor of 1.053 is applied in column 3 (see text). Literature data refer to 300 K.

mode and structural subunit:	unscaled frequency: (cm^{-1})	scaled frequency: (cm^{-1})	literature:[1] (cm^{-1})
ν_1^{TET} of Q^n:			
Q^0 (forsterite)	814	857	857[2], 856[56]
Q^0	820	863	863[2], 870[3], 850[4]
Q^1	840	885	930[3], 900[4]
Q^2	912+985	960+1037	990[3], 950-1000[4]
Q^3	980	1032	1060[3], 1050-1100[4]
Q^4	1026	1080	1200[3]
ν_3^{TET} of Q^n:			
Q^0 (forsterite)	916	965	965[5]
Q^0	908	956	–
Q^1	910	958	–
Q^2	942	992	–
Q^3	970	1021	–
Q^4	955	1006	–
dimer modes:			
ν_1^{DIM}	888	935	930 (Q^1)[3]
ν_3^{DIM}	814	857	–

[1] The tetrahedral stretching mode of forsterite at 857 cm^{-1} is mixed in character of ν_1^{TET} and ν_3^{TET}, but predominantly ν_1^{TET} (McKeown et al., 2010; Chopelas, 1991)
[2] Voronko et al. (2006)
[3] Kalampounias et al. (2009)
[4] McMillan (1984)
[5] Chopelas (1991)
[6] McKeown et al. (2010)

4.5 Discussion

General remarks

Calculation of averaged spectral densities and evaluation in terms of peak frequencies accounts for the disorder of the glass. There are three main sources of error on the frequencies. (1) The ab initio calculations have a systematic error, which we take into account by the application of the scaling factor of 1.053. (2) The results have an error due to incomplete convergence of the subspectra. We estimate the error to be less than 20 cm^{-1} for Q^0 to Q^4 tetrahedral stretching modes and the monomer (Q^0) bending modes. This estimation is based on reproducibility of the results from different segments of the MD runs. (3) The tetrahedral bending modes in higher Q^n species and especially the Si-O-Si modes have a larger error. This results from the high variability of the Si-O-Si angle which significantly affects vibrational frequencies (Hunt et al., 2011). For these subspectra, we estimate the error from the incomplete sampling of the Si-O-Si configurational space on the spectrum peak frequency to be of up to 50 cm^{-1}. Therefore, we use these results to determine trends in vibrational frequency with polymerization, but we exercise caution in attempting to infer precise vibrational frequencies.

Tetrahedral and ethane-like modes

Our results on the polymerization-driven frequency shift of ν_1^{TET} are best summarized in the inset in Fig. 4.7, and comparison to experimental results is visualized in Fig. 4.12. The result of 863 cm^{-1} for Q^0 in glasses fits well into the range of observed band frequencies (850 cm^{-1}, 863 cm^{-1} and 880 cm^{-1}) that have been assigned to Q^0 in several experimental studies (McMillan, 1984; Voronko et al., 2006;

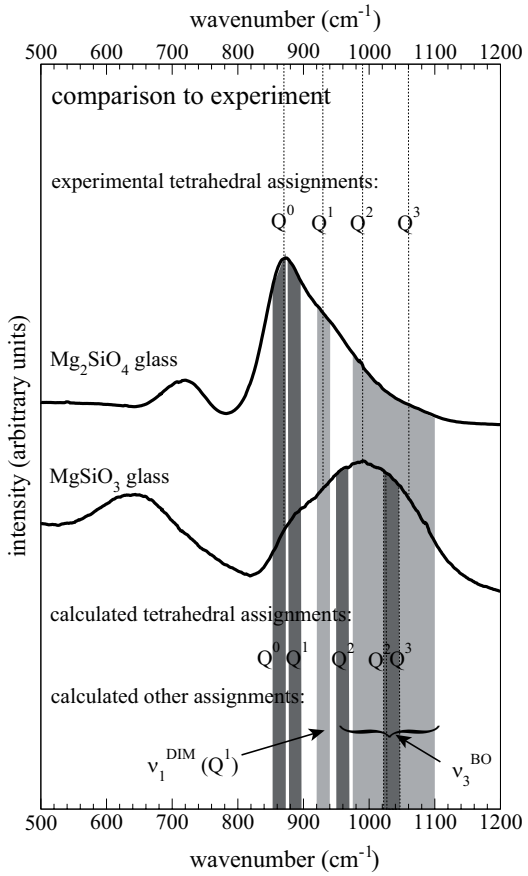

Fig. 4.12: Comparison of the results of the present study (lower part) to experimental Raman spectra of Mg_2SiO_4 and $MgSiO_3$ glasses from Kalampounias et al. (2009) and to experimental band assignment from the same study (upper labels).

Kalampounias et al., 2009) (Table 4.4). The results for the other Q^n species show somewhat larger apparent discrepancy with experimental frequencies commonly assigned to Q^1 to Q^4. The trend indicates that the calculated frequencies are lower than those experimentally assigned. We offer an explanation for this in Subsection 4.5 (Table 4.4, McMillan 1984; Durben et al. 1993; Voronko et al. 2006; Kalampounias et al. 2009; Nasikas et al. 2011).

In experimental studies, two different peaks have been assigned to Q^1: 900 cm^{-1} (McMillan, 1984) and 930 cm^{-1} (Kalampounias et al., 2009). McMillan (1984) assigned the 900 cm^{-1} band to the Q^1 tetrahedral symmetric stretch. Kalampounias et al. (2009) did not indicate a particular mode for their assignment of 930 cm^{-1} to Q^1. The calculated peak frequency of Q^1 ν_1^{TET} is at 890 cm^{-1} (Fig. 4.12). We found the ethane-like Q^1-Q^1 dimer symmetric stretch at 941 cm^{-1}. It is known from computational gas-phase studies that the dimer ethane-like symmetric stretch is of higher Raman intensity than the Q^1 tetrahedral symmetric stretch (Lasaga and Gibbs, 1988; Zotov et al., 1999). The computed peak frequencies of 890 cm^{-1} for Q^1 ν_1^{TET} and 941 cm^{-1} for the ethane-like Q^1-Q^1 symmetric stretch suggest that the above mentioned experimental bands at 900 cm^{-1} (McMillan, 1984) and at 930 cm^{-1} (Kalampounias et al., 2009) are correlated and result from two different modes of the Q^1-Q^1 dimer in silica-poor MgO-SiO_2 glasses.

Calculated frequencies of ν_1^{TET} vibration of Q^2 species are at 960 cm^{-1} and 1037 cm^{-1} for the double-peaked ν_1^{TET} and 999 cm^{-1} for ν_3^{TET} (Table 4.4). These frequencies compare well with the experimental

single-peak assignments of Q^2 to 990 cm^{-1} (Kalampounias et al., 2009) and 950-1000 cm^{-1} (McMillan, 1984). The Q^2 ν_1^{TET} double peak has been observed before in computational studies of sodium silicate glasses (Zotov et al., 1999) and silica species in hydrous environment (Chapter 2), and by an experimental Raman study on sodium silicate glasses (Malfait et al., 2008). The vibrational frequencies vary from from one environment to another, but the qualitative behavior of the Q^2 remains similar. Results in Fig. 4.9 suggest that the two peaks of the ν_1^{TET} QNM originate from different Q^2 NBO pair modes. Therefore, these two peaks do not necessarily possess the same Raman intensity, which is consistent with the asymmetric double-peak assignment of Q^2 proposed by Malfait et al. (2008). The fair agreement between our calculated ν_1^{TET} peak frequencies of 960 cm^{-1} and 1037 cm^{-1} and the experimental assignments of 990 cm^{-1} (Kalampounias et al., 2009) and 950-1000 cm^{-1} (McMillan, 1984) provide additional constraints on and explanation for the debated vibrational contribution of the Q^2 species.
The computed Q^3 ν_1^{TET} peak frequency is in fair agreement with the various experimental band assignments (Table 4.4). However, the Q^4 ν_1^{TET} peak frequency of 1080 cm^{-1} is off by 120 cm^{-1} from the common assignment at 1200 cm^{-1} (Mysen and Richet, 2005). This may be due to the fact that the tetrahedral QMNs are quasi-localized but not truly independent of the further environment. For instance, the adjacent tetrahedra of the Q^4 tetrahedra are not Q^4, but less polymerized. This weakening of the quasi-local approximation is also observed in pure SiO_2 (Taraskin and Elliott, 1997). In addition, as described in Subsection 4.5 (below), the bridging oxygen asymmetric stretch may contribute to the vibrational band observed in the vicinity of 1200 cm^{-1}. If so, the central peak position of the Q^4 symmetric stretch may be somewhat lower than 1200 cm^{-1}, and the apparent position of 1200 cm^{-1} may be influenced by the bridging oxygens between Q^3-Q^4 (and Q^4-Q^4) pairs (Fig. 4.11). Future study focused on the high-frequency vibrations of highly polymerized silicate materials is required to decipher these issues.
From the inset in Fig. 4.7, it is clear that the ν_1^{TET} does not linearly evolve with increasing degree of polymerization, but rather is bimodally distributed between Q^0 and Q^1 on the side of weak or no polymerization and Q^3 and Q^4 on the side of of high degree of polymerization. Q^2-species occupy an hybrid state, showing aspects of both the lower and higher Q^n-like vibrations. The frequency of the tetrahedral asymmetric stretching mode ν_3^{TET} depends much less on the degree of polymerization than the ν_1^{TET}. Its contribution to Raman spectra of silicate glasses is generally not considered in experimental band assignment, despite the fact that it can show considerable Raman intensity in silicate minerals such as forsterite or zircon. Since our results do not provide information on this question, we do not include ν_3^{TET} in Fig. 4.12. However, if the ν_3^{TET} in glasses possesses a non-negligible Raman intensity, its neglect in the process of spectral fitting could result in misinterpretation of the degree of polymerization (see below).

Bridging oxygen modes

The frequencies obtained from the Si-O-Si QNMs are consistent with the observation that the ν_1^{BO} peak (Table 4.3) is in the intermediate-frequency region between 600 and 800 cm^{-1} (McMillan, 1984; Kalampounias et al., 2009; Nasikas et al., 2011). The results indicate that the ν_1^{BO} shifts to lower frequencies from low-degree polymerization (720 cm^{-1} for Q^1-Q^1) to intermediate-degree polymerization (650 cm^{-1} to 750 cm^{-1} for Q^1-Q^2 and 690 cm^{-1} for Q^2-Q^2, Fig. 4.11). This agrees with the experimentally observed shift to lower frequencies between glassy Mg_2SiO_4 (690 cm^{-1}) and $MgSiO_3$ (650 cm^{-1}) (Kalampounias et al., 2009). However, with further increasing to high degrees of polymerization the peak frequencies shift to higher frequencies, up to 810 cm^{-1} for Q^2-Q^4 (Fig. 4.11). The 800 cm^{-1} band in Raman spectra of pure SiO_2 has sometimes been assigned as a tetrahedral mode (e.g. Galeener 1979; Ivanda et al. 2003). In the light of our results of ν_1^{BO}, the assignment of the 800 cm^{-1} band as Si-O-Si mode (bending and symmetric stretching) seems more appropriate (e.g. Awazu and Kawazoe 2003).
The ν_1^{BO} QNM is not only sensitive to the degree of polymerization, but also to the strain of the Si-O-Si angle in small rings (inset in Fig. 4.10). In threefold rings, the Si-O-Si is formally 130°, which is only

slightly less than the angle of minimal energy of about 140° (Newton and Gibbs, 1980). Therefore, the strain is weak and the vibrational frequency of ν_1^{BO} of threefold rings is almost identical to the ν_1^{BO} in fourfold rings. However, in twofold rings, the ν_1^{BO} peak frequency shifts from about 750 cm^{-1} to about 920 cm^{-1} (inset in Fig. 4.10). Twofold silica rings are present as defects in silica glass where they are thought to be responsible for Raman bands at 890 cm^{-1} and 910 cm^{-1} (Ceresoli et al., 2000). It has been found that the strain energy of twofold rings is significantly lower than originally calculated by Newton and Gibbs (Newton and Gibbs, 1980; Hamann, 1997).

The ν_3^{BO} mode (Table 4.3) in the range of about 980 cm^{-1} up to 1200 cm^{-1} shows a similar behavior to that of the ν_1^{BO} mode, with increasing polymerization (Fig. 4.10). The ν_3^{BO} exhibits a trend to lower frequencies for low to intermediate polymerization (from Q^1-Q^1 via Q^1-Q^2 to Q^2-Q^2). We observe increasing frequencies for intermediate to high degree of polymerization. The ν_3^{BO} vibrations are the only cause for vibrational density of the dimer above 1000 cm^{-1}, and its Raman intensity is high, making this mode one of the mosts intense in the case of the dimer (Lasaga and Gibbs 1988; Kubicki and Sykes 1993; Zotov and Keppler 2000; Hunt et al. 2011, see also Lasaga 1982 and Tossell 2005). It is reasonable to extrapolate that the ν_3^{BO} remains an intense Raman-active mode even for a higher degree of polymerization than the dimer. In fitting experimental Raman spectra, the Raman contribution of this vibration is considered in several studies (Mysen and Frantz, 1994; Mysen, 2009, 2010), thus accounting for the BO contribution to the higher-frequency spectral range. However, other experimental Raman studies explain all Raman intensity above a certain frequency (e.g., 980 cm^{-1}, see Kalampounias et al. 2009) by the ν_1^{TET} of Q^2, Q^3 and Q^4, without contribution from ν_3^{BO} vibrations (see Fig. 4.12) (Kalampounias et al., 2009; Herzog and Zakaznova-Herzog, 2011; Malfait et al., 2007). Based on our results for ν_3^{BO}, we argue that neglecting the BO contribution to the higher-frequency vibrations risks to significantly overestimate the degree of polymerization, because Raman bands that should be recognized as BO can be instead treated as higher-Q^n species. In studies that neglected the ν_3^{BO} contribution not only Q^1 and Q^2 peaks were fitted to Raman spectra of Mg_2SiO_4 glasses, but even Q^3 (Kalampounias et al., 2009) (see Fig. 4.12). Moreover, the extension of ν_3^{BO} spectrum up to 1200 cm^{-1} in the case of Q^3-Q^4 (Fig. 4.11) may lead to an overestimation of the Q^4 contribution both in its frequency and its intensity. Based on the results of the present study, we suggest that it may be worthwhile to re-interpret some measurements under the inclusion of the contribution of bridging oxygens at higher frequencies.

The origin of the 900 cm^{-1} band in sub-orthosilicate glasses

Nasikas et al. (2011) have measured Raman spectra of a calcium-magnesium sub-orthosilicate glass and did not observe a band around 700 cm^{-1}, which they, in agreement with the common assignment, interpret as evidence for complete absence of bridging oxygen and therefore of polymerization. However, they observed an unusual depolarized band at about 900 cm^{-1}. They conclude that, due to the absence of polymerization, this band needs to be explained by tetrahedral modes. They suggested an $2\nu_2^{TET}$ overtone. The mode-projection method employed in the present study is capable of detecting spectral overtones. Therefore, if a ν_2^{TET} overtone occurred in the system, it would appear in the calculated spectra. However, the results presented here for the tetrahedral modes of Q^0 (Fig. 4.5) do not show a high-frequency contribution of the ν_2^{TET} (E-bending) mode (Fig. 4.5). The broad high-frequency contribution in the ν_4^{TET} ("umbrella"-bending) QNM is an artifact that is unrelated to overtones (Subsection 4.3 and Fig. 4.2). We found the ν_1^{BO} in twofold rings (edge-sharing tetrahedra) at 920 cm^{-1}. This is in excellent agreement with experimental IR bands of cyclodisiloxane at 908 cm^{-1}, and with calculated IR bands at 909 cm^{-1} and 920 cm^{-1} (Mhin et al., 2010). Twofold rings are observed in leucophoenicites, a group of hydrous low-pressure manganese silicates (Freed, 1993; Moore, 1970).

The calcium-magnesium sub-orthosilicate glass investigated in the above mentioned study is extremely basic (Nasikas et al., 2011). It would not contradict structural models of silicate melts, if this basic composition could drive the little amount of silica into a state of polymerization that "frees" as much

oxygen as possible to balance and shield the cationic charges (Hess, 1995; Lin and Pelton, 1979; Flood and Förland, 1947). In the light of these considerations, we suggest that the depolarized band observed by Nasikas et al. (2011) at about 900 cm^{-1} could be caused by twofold silica rings (cyclodisiloxanes), which formed in the melt phase and persisted during the fast quench. This would be a form of polymerization hitherto not considered in silicate glasses. It could be verified by NMR measurements, and potentially also by UV spectroscopy (Awazu and Kawazoe, 2003; Ceresoli et al., 2000).

4.6 Conclusions

In this study, we have characterized the vibrations of silica species in MgO-SiO_2 glasses. The results give a comprehensive picture of the subspectra of different modes from individual types of structural units like the tetrahedron and the BO. The vibrational behavior of these structural units in any degree of polymerization has been described. The application of our method to crystalline Mg_2SiO_4 demonstrated the capability of the method. Comparison of $SiO_4{}^{4-}$ monomer subspectra to frequencies calculated explicitly with NMA confirmed the applicability of the method to the disordered glasses.

(1) The evolution of tetrahedral stretching modes ν_1^{TET} and ν_3^{TET} with increasing Q^n speciation confirmed the common practice of band assignment for Q^0, Q^3 and Q^4. The frequency crossover of ν_1^{TET} and ν_3^{TET} with increasing degrees of polymerization leads to a double peak of the tetrahedral Q^2 modes, in agreement with observations both from computational and experimental studies (Zotov et al., 1999; Malfait et al., 2007).

(2) The Si-O-Si BO symmetric and asymmetric stretching modes show a frequency decrease between low and intermediate degrees of polymerization. Increasing the polymerization further shifts them to higher frequencies. The Raman intense Si-O-Si asymmetric stretch vibrations fall into the region of 900 cm^{-1} to 1200 cm^{-1}. If this contribution is neglected and the region is fitted by the contributions of Q^n-species only, then the degree of polymerization of a glass is likely to be overestimated.

(3) Analysis of the ethane-like symmetric stretch to the $Si_2O_7{}^{6-}$ dimer revealed a mode that is highly localized in frequency at 935 cm^{-1} peak frequency. This result helps to understand the vibrational origin of the experimentally observed band at 930 cm^{-1} that had previously been assigned to Q^1 species (Kalampounias et al., 2009). Raman spectra of highly polymerized silicate glasses and melts are especially difficult to analyze, because there is strong overlap of several different structural-modal vibrations, as has been demonstrated in this contribution. The modeling conducted in the present study provides significant insight into the origins of measured spectroscopic features, but many interesting questions remain, including the origin of the 800 cm^{-1} band in pure fused silica, and the relationship between tetrahedral and bridging-oxygen modes in the high-frequency region. These issues deserve additional studies.

We expect that the outlined method can be successfully applied to other, more complex systems that involve several network-forming, network-modifying and/or intermediate cations. Application of the bond polarizability model to weakly polymerized MgO-SiO_2 glasses would complement the mode-projection method, allowing estimates of the Raman intensities of all the modes considered here. Future work will incorporate both bond polarizability and the mode-projection technique in order to predict vibrational frequencies and relative intensities of species in glasses and melts.

Chapter 5

Release of molecular water in supercritical SiO_2-H_2O fluid

5.1 Abstract

We report the structure of supercritical SiO_2-H_2O fluid composed of 50mol% SiO_2 and 50mol% H_2O between 3000 K and 2400 K, obtained from ab initio molecular dynamics of 192-atom models. During the simulation, water molecules are continuously formed and dissociated according to the network modifying reaction 2SiOH = SiOSi + H_2O. After quench to 2400 K, the degree of polymerization of the silica network increases noticeably within several tens of picoseconds, accompanied by the release of molecular water. We interpret this process as a sub-critical precursor to phase separation which is expected at lower temperatures. This structural change is subject to a finite size effect that tends to stabilize the high-temperature structure in smaller models. Bond lifetime calculations give insight into the slowing down of the reaction dynamics. At 2400 K the MD run duration required to reach and sample structural equilibrium is above 200 ps.

5.2 Introduction

Geological processes such as rock melting and magmatism are governed by the interplay of silicate matter with volatiles such as H_2O (Johnson et al., 1994; Lange, 1994). The system SiO_2-H_2O is a simplified chemical model to study fluid-melt interaction (Kennedy et al., 1962; Newton and Manning, 2008; Hunt and Manning, 2012). At conditions of the Earth's surface and upper crust it is dominated by a large region of immiscibility. This region limits the mutual solubility of SiO_2 into water and of H_2O into SiO_2 melt or glass to a few weight percent. Mutual solubility increases with pressure and temperature, eventually leading to a single-phase supercritical fluid above the consolute temperature (Mysen, 1998; Hermann et al., 2006; Hack et al., 2007). There is an upper critical end point (UCEP) at 1 GPa and about 1300 K (Stalder et al., 2000; Newton and Manning, 2008), above which SiO_2 melts in the presence of H_2O to form one single fluid phase (Fig. 5.1) (Kennedy et al., 1962; Paillat et al., 1992; Mysen, 1998; Stalder et al., 2000, 2001; Hack et al., 2007; Newton and Manning, 2008). With the UCEP at 1 GPa, which corresponds to a depth of about 30 km, such supercritical hydrous silicate melts can form in the lower crust, if there is a supply of volatiles (Stalder et al., 2000; Hermann et al., 2006; Agee, 2008; Hack and Thompson, 2010). Large amounts of volatiles are released at such depths from the subducted oceanic plate in subduction zones. They can melt the surrounding rock. The composition of partial melts in equilibrium with ultramafic rocks becomes more silicic with increasing amount of water (Bureau and Keppler, 1999). It is therefore possible that supercritical hydrous melts form in or above the subducted slab. The properties of supercritical hydrous melts could govern the magmatic processes witnessed at the surface (Audétat and Keppler, 2004; Mibe et al., 2011). Knowledge about the structure of the supercritical fluid will help to understand its petrological properties such as density and viscosity (Bureau and Keppler, 1999; Audétat and Keppler, 2004; Hack and Thompson, 2010). Computational models can give valuable insight into the structure and behavior of this material that is extremely difficult to investigate by in situ experiments (Shen and Keppler, 1997; Audétat and Keppler, 2004).

The structure of silicate melts in general is governed by a network of interconnected SiO_4^{4-} tetrahedra whose state of polymerization can be characterized in terms of Q^n-species, with n indicating the number of oxygens shared with other tetrahedra. H_2O in silicate melts exists predominantly in the form of hydroxyl groups Si-OH and of molecular H_2O that fills voids in the silicate network or forms small clusters (Farnan et al., 1987; Soper et al., 2006). These species mutually exchange in the network breaking reaction

$$SiOSi + H_2O = 2SiOH. \tag{5.1}$$

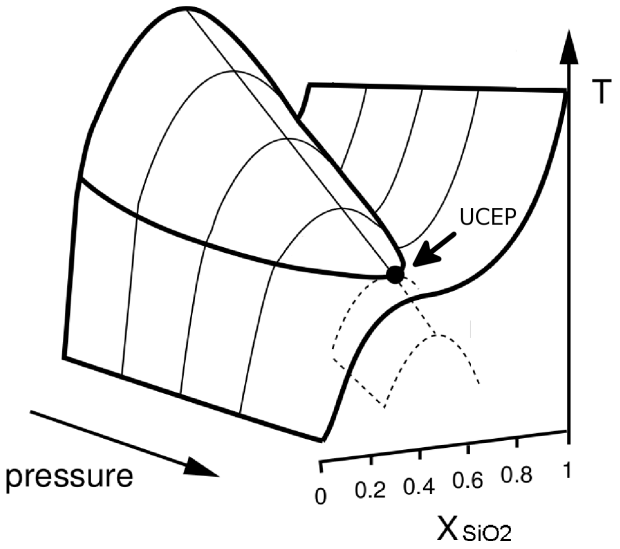

Fig. 5.1: PTx-diagram of the system SiO_2-H_2O (modified after Stalder et al. 2000). The pressure at the upper critical end point (UCEP) is 1 GPa.

Therefore, in the system SiO_2-H_2O oxygen atoms occur in three species: Bridging oxygen (BO) in the silica network, non-bridging oxygen (NBO) at its terminal branches, and molecular H_2O water (WO). Structure, viscosity, self-diffusion coefficients and other properties of a supercritical fluid or a hydrous sub-critical silicate melt are governed by the extend to which reaction 6.1 proceeds to either side. Therefore, considerable experimental effort has been dedicated to the determination of the speciation of H_2O in hydrous silicate glasses and melts (see Mysen and Richet 2005 and Kohn 2000 and references therein). At dilute concentrations, H_2O is found in hydrous glasses mainly as hydroxyl groups. With increasing total H_2O content, the fraction of molecular H_2O increases. In-situ studies have shown that the H_2O speciation changes during the quenching time of a silicate melt to a glass (Nowak and Behrens, 2001). This underlines the need to study the structure of hydrous silicate melts at high temperatures.

The activity of H_2O in silicate melts is highly non-ideal and rises with the square of its mol fraction (Burnham, 1974; Newton and Manning, 2008), due to the large energetic effects of H_2O dissociation. Based on experiments, Newton and Manning (2008) predict for 1350 K and 1 GPa a plateau for H_2O activity at about 50mol% H_2O. The content of molecular water should steeply increase in this compositional region. At higher temperatures, the behavior is expected to be similar. Also in more complicated systems, such as hydrous albitic melts, it has been assumed that at about 30mol% H_2O there may be a change in dissolution mechanism (Sykes and Kubicki, 1993; Kohn, 2000).

Atomic-scale modeling is a useful tool to obtain additional insight into structure and properties of material. As will be described below, conventional unconstrained molecular dynamics simulations of disordered silicate material requires very high temperatures of typically 3000 K. Although this is well above

those temperatures relevant in experiment and nature, valuable insight may be obtained and extrapolations to lower temperatures be made. Karki and Stixrude (2010) found by ab initio molecular dynamics (MD) that in a silica melt with 23mol% H_2O at 0.1 GPa and 3000 K, only 1% of the nominal H_2O forms molecular water, the remainder being completely dissociated by reaction 6.1. Anderson et al. (2008b) found in a Monte-Carlo study using the classical Garofalini-potential (Feuston and Garofalini, 1990), that in a supercritical fluid of 40mol% H_2O in SiO_2 at 3000 K and 1 GPa, only 4% of the nominal water were molecular H_2O. These values, obtained at 3000 K, cannot be compared to experimental results at lower temperatures, because temperature drives reaction 6.1 towards the right side (Kohn, 2000). However, even at the temperatures of MD modeling, the H_2O activity may still follow the same non-ideal trend as at experimental temperatures (Burnham, 1974).

Atomic-scale modeling of systems that involve reaction 6.1 crucially depends on the correct reproduction of its reaction energy and its energetical reaction barriers. The MD sampling time is commonly limited to tiny fractions of a second even in classical MD, even more in ab initio MD. This requires conventional unconstrained MD to be carried out at high temperatures for enhanced dynamics, otherwise reaction 6.1 is an event too rare to reach structural equilibrium in feasible timescales. Therefore, the energy barrier of reaction 6.1 determines the temperature down to which structural equilibrium can be reached in feasible MD trajectory lengths. For future atomic-scale modeling it is necessary to find a precise measure to answer the question, down to which temperature structural equilibrium in the system SiO_2-H_2O can possibly be reached in a given ab initio MD trajectory length of typically less than a few hundreds of picoseconds. Once such a relation between bond dynamics and temperature has been established with ab initio accuracy, the reliability of classical potentials at high temperatures could be benchmarked against this relation (Feuston and Garofalini, 1990; Garofalini and Martin, 1994; Yamahara and Okazaki, 1998; Rao and Gelb, 2004; Fogarty et al., 2010).

Besides the time scale, the small number of atoms is another limitation of ab initio silicate modeling. Periodic boundary conditions (PBC) are usually employed in molecular dynamics. However, they represent a sterical constraint which may keep the structure of the silicate model in an artificial self-confinement. If the model is small, an artificial "caging" effect of PBC stabilizes a given structure, i.e. it inhibits a complete sampling of phase space in time and the adaptation of the structure to e.g. lower temperatures. Silicate networks show considerable variability in their intermediate range structure (Van Ginhoven et al., 2005; Trave et al., 2002). This probably applies especially to the system SiO_2-H_2O where structure adaptation involves the reverse of reaction 6.1 which requires large translational movements and energetical barriers to be overcome.

In this study, we give answers to a series of the questions raised above. We report the structure of equimolar single-phase supercritical SiO_2-H_2O fluid at 3000 K, and the structural changes that occur when the temperature is lowered from 3000 K to 2400 K. These changes are sub-critical changes of polymerization upon cooling, accompanied by release of molecular water. We chose temperatures of 3000 K and 2400 K, both at constant density of 1.88 g/cm^3 which corresponds to a pressure of about 4.3 GPa (3000 K) and 3.5 GPa (2400 K). The average structure of supercritical SiO_2-H_2O fluid is described in terms of the average degree of polymerization, the Q^n-species distribution and the speciation of the nominal H_2O. We investigate the structural variability and the effect of model size on the structure, by carrying out several separate runs each for two different model sizes, 192 atoms (nominally 32 SiO_2 and 32 H_2O) and 96 atoms (nominally 16 SiO_2 and 16 H_2O). Finally, we give an estimate on the lower temperature limit at which structural equilibration can be reached within the timescales accessible to ab initio MD.

5.3 Methods

Modeling technique

We used density functional theory (Kohn and Sham, 1965) in the plane wave pseudopotential approach as implemented in the CPMD code (Marx and Hutter, 2000). For the exchange-correlation functional the PBE (Perdew et al., 1996) generalized gradient approximation (GGA) was used which yields satisfactory results in the description of hydrogen bonds (Pöhlmann et al., 2004). GGA functionals yield better results than those of the local density approximation (LDA) type for disordered network forming systems (Hamann, 1996, 1997; Massobrio et al., 1999; Van Ginhoven et al., 2005; Demichelis et al., 2010). Martins-Troullier type pseudopotentials were used (Troullier and Martins, 1991), and spin polarization has been neglected (Ma et al., 2005), The Kohn-Sham wavefunctions are expanded at the Γ-point with a cutoff energy of 80 Ry. Dependence of electronic potential on more extended k-point sampling was found to be negligible. Forces were within about 1% deviation compared to those obtained with larger plane wave cutoffs of 140 Ry. We used Car-Parrinello molecular dynamics (Car and Parrinello, 1985) with a ficticious electronic mass of 400 a.u. and an integration time step of 4 a.u. (0.097 fs) (Grossman et al., 2004; Schwegler et al., 2004; Kuo et al., 2004). Atomic positions and velocities were recorded every 40 a.u. The ficticious electronic kinetic energy was thermostatted. The Car-Parrinello forces agreed to 98% with the forces from a fully minimized wavefunction as in Born-Oppenheimer MD. This was checked for several configurations throughout a run, up to 5 ps after the last Born-Oppenheimer wavefunction optimization (Pastore et al., 1991). All modeling runs were performed in the canonical (NVT) ensemble in periodic boundary conditions. The temperature was controlled by a Nosé-Hoover thermostat (Martyna et al., 1992). The pressure was calculated from the trace of the continuously calculated stress tensor, which was corrected for incomplete basis set (de Koker et al., 2008; Karki, 2010; Lee and Wan, 2008).

System setup

Table 5.1: The 192 atom models (nominally 32 SiO_2 and 32 H_2O) for an estimate of the density-pressure relation at 3000 K (Fig. 5.2). Molar volume refers to $(SiO_2)_{0.5}(H_2O)_{0.5}$. The pressure mean absolute error (MAE) is indicated as uncertainty.

model label:	D1	D2	D3
density (g/cm^3):	1.4	1.88	2.05
molar volume (cm^3/mol):	28.0	20.7	19.0
model further used as:	–	192-1	–
equilibration run (ps):	11	11	11
production run (ps):	30	30	30
pressure (GPa):	0.7	4.3	5.6
MAE of pressure (GPa):	0.8	1.2	1.2

Firstly, we determined a volume-pressure relation at 3000 K to determine an appropriate density for further modeling steps. For that aim, we set up three 192 atom models at different densities (Table 5.1). These densities were taken from literature data on pure SiO_2, pure H_2O and the partial molar volume of H_2O in silicate melts (Hudon et al., 2002; Trave et al., 2002; Karki et al., 2007; Mookherjee et al., 2008). Initial configurations were generated with two different routines, termed "hydrogun" (HG) and "randombox" (RB). The HG routine proceeds as follows. A classical MD run of pure SiO_2 was carried out at 3000 K and 0 GPa for 200 ps using the PIMAIM potential (Jahn and Madden, 2007). Then an automated routine removed randomly chosen silicon atoms and inserted four hydrogens each near the

four planes of the tetrahedra where the silicon atom had been removed. The RB routine fills a given volume with atoms, under constraints regarding the minimal atomic distances, equal to the positions of the first maximum in the pairwise radial distribution functions from Pöhlmann et al. (2004).

The three models of different density each (Table 5.1) were run for 30 ps after initial equilibration of 11 ps. The calculated pressure was not corrected for the systematic overestimation of GGA (PBE) density calculations, because no experimental data are available for intermediate compositions in the system SiO_2-H_2O. The pressure fluctuation, calculated as mean absolute error, is indicated (Table 5.1). Pressure calculation of each of these models allowed us to establish a simple volume-pressure relation (Fig. 5.2). We chose the molar volume of 20.7 cm^3/mol (density 1.88 g/cm^3) at a pressure of 4.3 GPa at 3000 K (Table 5.1) and about 3.5 GPa at 2400 K (not shown) as representative for upper mantle conditions. These pressures correspond to a depth of about 80 to 120 km.

After the decision for the uniform density of 1.88 g/cm^3, several separate models of equimolar composition were set up: three 192 atom models (32 SiO_2 and 32 H_2O) and three 96 atom models (16 SiO_2 and 16 H_2O, Table 5.1). The setup of different model sizes allows us to obtain information on the structural effect of system size. The setup of several separate (and therefore mutually independent) models allows us to obtain information on the variability of the structure at otherwise identical MD conditions (Trave et al., 2002; Van Ginhoven et al., 2005). The temperature-cascade regime that we carried out on the models is given in Table 5.1. After production runs at 3000 K, four models were quenched directly to 2400 K, two more runs had an intermediate step at 2700 K. Total run duration at 2400 K was at least 100 ps.

For comparison and reference, we carried out a MD run of 20 ps for pure SiO_2 at 3000 K and molar volume of 45.8 $Å^3$/SiO_2, which is similar to the experimental volume of SiO_2 melt at the ambient conditions melting point (Kress and Carmichael, 1991). The initial configuration of the 192 atoms is the same seed that was used to construct model 192-1 via the HG routine, as described above.

Table 5.2: The time-temperature regimes for all runs between 3000 K and 2400 K. Trajectories are divided in equilibration runs and production runs at each temperature. All models are at density of 1.88 g/cm^3. Initial configurations have been generated either with HG or RB (Subsection 6.3). The 192 atom models consist of nominally 32 SiO_2 and 32 H_2O, the 96 atom models of nominally 16 SiO_2 and 16 H_2O.

model name:	192-1	192-2	192-3	96-1	96-2	96-3
number of atoms:	192	192	192	96	96	96
initial setup routine:	HG	RB	RB	RB	HG	HG
cubic cell dimensions:	13.0 Å	13.0 Å	13.0 Å	10.3 Å	10.3 Å	10.3 Å
total trajectory (ps):	141	216	200	262	278	231
3000 K: (4.3 GPa)						
total (ps):	40	51	10	56	56	75
equilibration run (ps):	10	11	5	16	16	15
production run (ps):	30	40	5	40	40	60
2700 K: (4.0 GPa)						
total (ps):	–	–	–	52	52	–
equilibration run (ps):	–	–	–	12	12	–
production run (ps):	–	–	–	40	40	–
2400 K: (3.6 GPa)						
total (ps):	101	165	180	154	170	156
equilibration run (ps):	21	85	100	74	90	76
production run (ps):	80	80	80	80	80	80

5.4 Results

Density-pressure relation

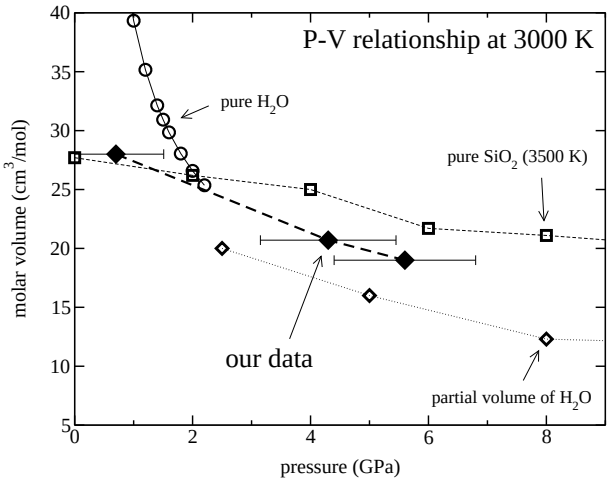

Fig. 5.2: Molar volume against pressure for three models with densities between 1.4 and 2.05 g/cm^3 (Table 5.1). Error bars reflect the mean absolute error (MAE). For comparison, literature data of the molar volume of SiO_2 and of H_2O are shown. Circles: Pure H_2O at 3000 K (Churakov and Gottschalk, 2003). Diamonds: partial molar volume of H_2O in silicate melt (Mookherjee et al., 2008). Squares: pure SiO_2 at 3500 K (Trave et al., 2002).

The molar volume of the three D models refers to $(SiO_2)_{0.5}(H_2O)_{0.5}$ and is plotted against the calculated pressure in Fig. 5.2 (see also Table 5.1). For comparison, literature pressure-volume data of pure SiO_2 and of pure H_2O, and the partial molar volume of H_2O in silicate melts is also shown (Trave et al., 2002; Churakov and Gottschalk, 2003; Mookherjee et al., 2008). The extrapolation to lower temperatures and comparison to experimental data is not very useful because of the extreme temperature differences between model and experiment (Richet and Polian, 1998). At the lowest density of 1.4 g/cm^3 and P=0.7 GPa (D1), the model reflects the high molar volume of H_2O. The volume-pressure relation in Fig. 5.2 suggests a close-to-ideal mixing at 3000 K and for all pressures. For all following modeling runs, we used a uniform density of 1.88 g/cm^3.

Radial distribution and coordination functions

Knowledge of the partial (i.e. pairwise) radial distribution functions (RDF) is the basis for further structural evaluation. RDFs are calculated for Si-O, O-H, O-O, Si-Si and H-H from

$$g_{\alpha\beta}(r) = \frac{1}{4\pi\rho_\beta r^2}\left[\frac{dN_\beta(r)}{dr}\right]. \tag{5.2}$$

The RDFs from various models are shown for 3000 K and 2400 K in Fig. 5.3. Pure SiO_2 is shown for comparison for Si-O, Si-Si and O-O. The RDFs of O-H (A) and Si-O (D) are almost insensitive to temperature between 3000 K and 2400 K. Because of the high temperatures, the O-H RDF (A) does not show a distinct hydrogen bonding shoulder which would be at about 1.9 Å as in the case of water (Schwegler et al., 2004). The fundamental short-range structure of the silica network part of the system is close to that of SiO_2 melt, as can be seen from the similarity of the Si-O and Si-Si RDFs compared to those of pure SiO_2. In fact, the pure SiO_2 Si-O RDF falls completely on top of the Si-O RDF at 2400 K. The Si-Si, O-O and H-H RDFs do reflect varying degrees of polymerization (Anderson et al., 2008b),

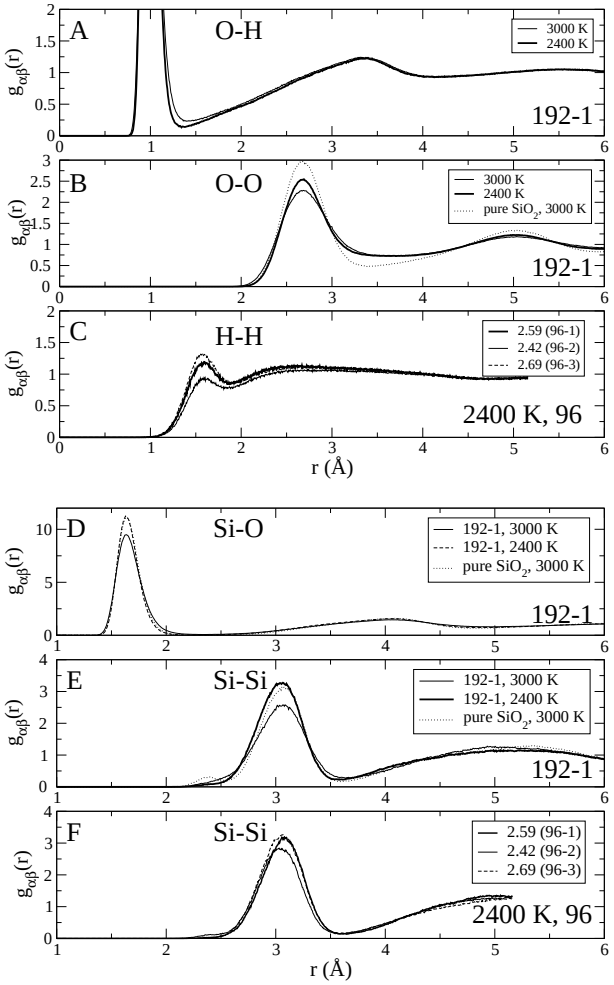

Fig. 5.3: Pairwise radial distribution functions (RDF) from various models for 3000 K and 2400 K. Pure SiO_2 is shown for comparison.

as is shown by comparing the 96 atom models at 2400 K, which vary in the time-averaged degree of polymerization between 2.42 and 2.69.

The pairwise coordination numbers are calculated using the first minimum of the RDFs as the conventional cutoff radius (insets in Fig. 5.4). The Si-O coordination distribution reflects the dominant tetrahedral coordination of silicon by oxygen, plus a small fraction of short-lived fivefold coordination. The O-Si coordination is distributed over zero-, one- and twofold coordination, which reflects the three possible speciations of oxygen, as H_2O, SiOH and SiOSi. The O-H coordination distribution reflects the two possible speciations of hydrogen, as SiOH and as molecular H_2O. The long-range tails of the distance-coordination plots contain information about the H_2O and SiO_2 cluster sizes, but since these are strongly model size dependent, we do not evaluate them here.

The first coordination shells of silicon and oxygen, and oxygen and hydrogen are well defined, as can be assumed because the pairwise RDFs fall to almost zero density at their first minimum. This is crucial for a meaningful determination of the fractional amounts of oxygen species. For this reason we double-checked the well-definedness of the first coordination shells in plots of fractional coordination against radial distance in Fig. 5.4. For instance, the position of the first Si-O RDF minimum at 2.4 Å coincides with plateaus in the three coordinational states of oxygen by silicon of zero silicon neighbors (i.e., WO), one silicon neighbor (i.e., NBO) and two silicon neighbors (BO). The same plateau region exists for the

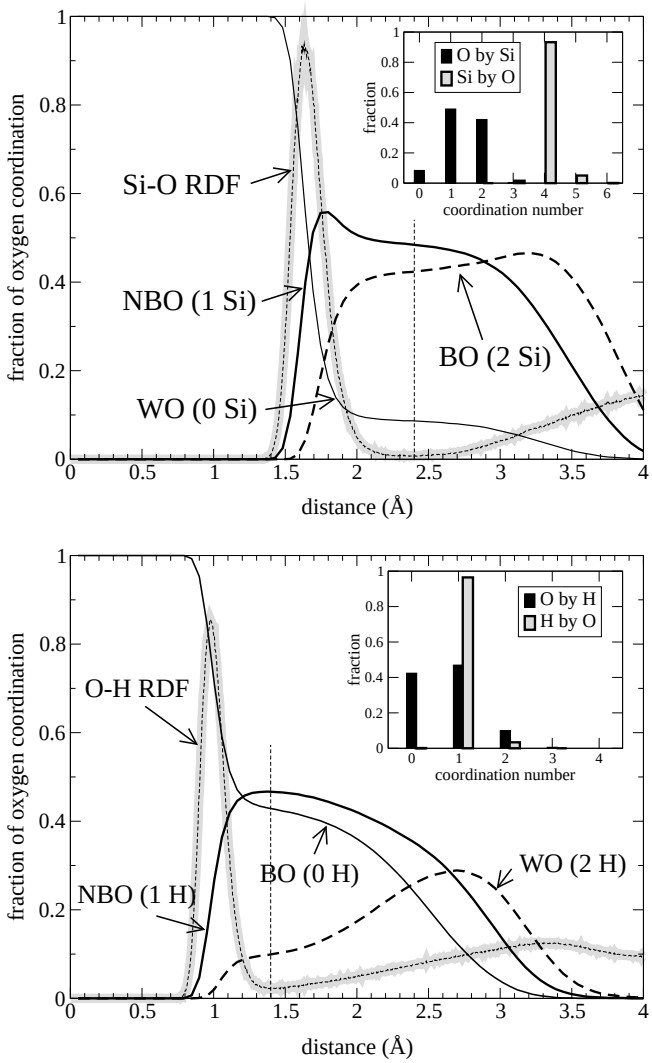

Fig. 5.4: Coordination versus radial distance plots and RDFs for Si-O (top) and O-H (bottom). Graphs indicate the fractional amount of bridging oxygen (BO), non-bridging oxygen (NBO) and oxygen forming water molecules (WO). The Si-O RDF is downscaled by 10 for visualization. The insets show the pairwise coordination distribution within the radial distance cutoff radius indicated by the vertical dashed lines.

three oxygen species with respect to their coordination by zero, one or two hydrogen atoms (bottom of Fig. 5.4). Therefore, the coordinational shells are sufficiently well-defined such that the estimation of relative amounts of oxygen species is insensitive to small variations of the radial cutoff.

Dynamical calculation of molecular water and oxygen speciation

The structure of SiO_2-H_2O and its degree of polymerization can be described in the relative amounts the three oxygen species BO, NBO and WO (see Section 5.2). Structural changes involving reaction 6.1 are necessarily reflected in the relative amounts of oxygen species. The oxygen speciation is dynamically calculated based on the structural considerations outlined in Section 5.4. Counted as WO are those oxygen atoms that have at least two hydrogen atoms in the first neighbor shell, but no silicon. Bridging oxygen atoms are those oxygen, that have at least two silicons as neighbors, but not more than one (accidental) hydrogen. Non-bridging oxygen are those that have one silicon and at least one hydrogen as

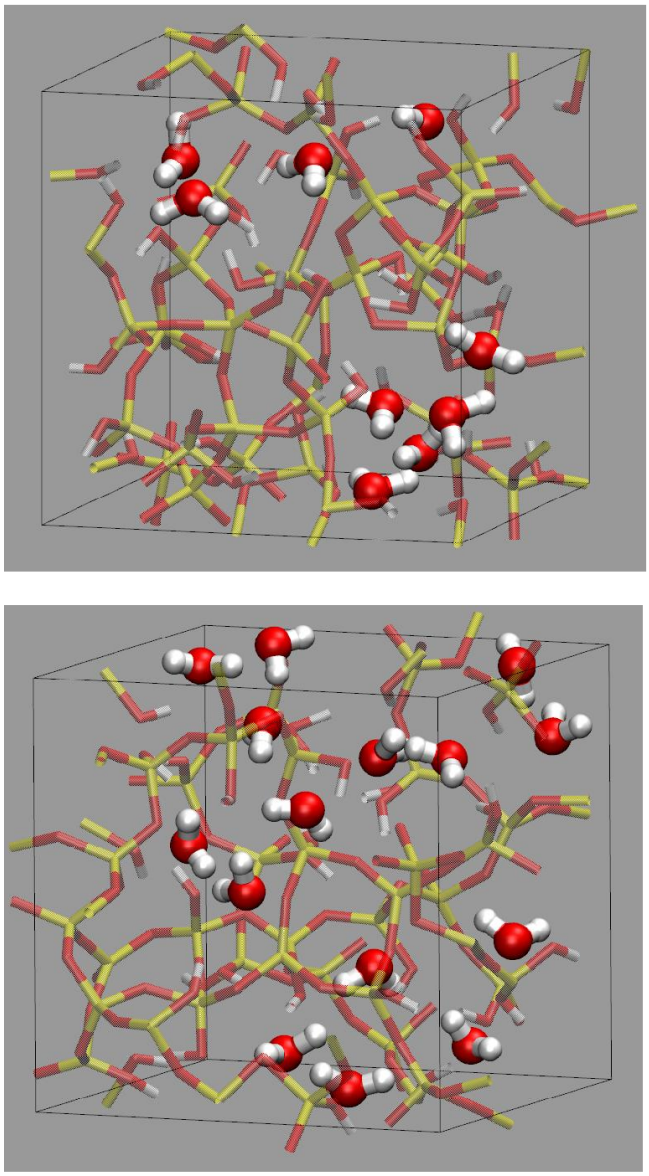

Fig. 5.5: Snapshots of the model M3-1 at 3000 K (top) and 2400 K (bottom) (Table 6.1 and Fig. 5.6). Note the increase of molecular water by 70%.

neighbors.

The amount of molecular water is plotted relative to the total nominal H_2O content in Figs. 5.6 and 5.7 for the 192 atom models and 96 atom models, respectively. At 3000 K, the number of H_2O molecules fluctuates around an average value with a period of about 15 ps (Fig. 5.6). This indicates that structural equilibrium is reached at 3000 K after a few tens of picoseconds. For a sketch of model M3-1 at 3000 K see Fig. 5.5. For the 192 atom models the fraction of molecular water is on average 28% with little scatter between the models. The models from the two different generation routines HG and RB (Section 6.3) become structurally similar within a few picoseconds. High frequency oscillations in Fig. 5.6 result from the analysis routine that calculates the amount of water molecules at every time step anew, without conditions with respect to transient continuity.

In each of the 192 atom models the number of water molecules increases after the thermostat is switched

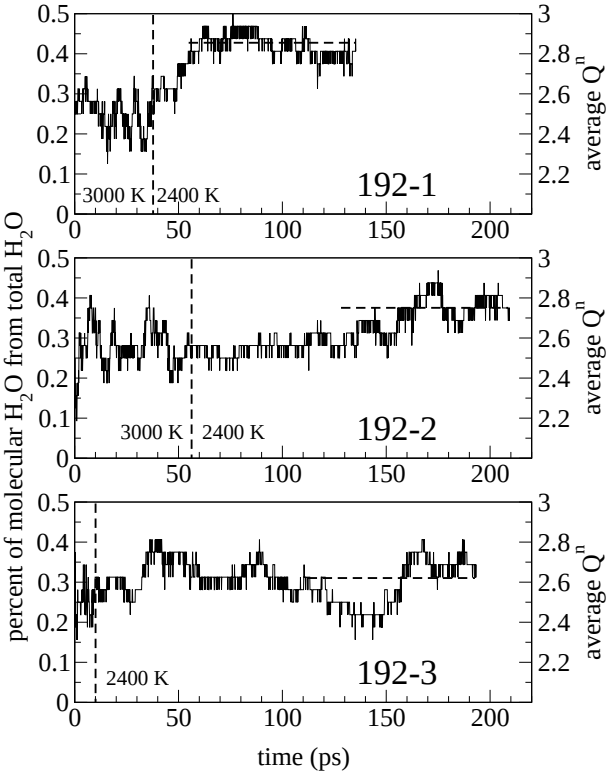

Fig. 5.6: Fraction of the total nominal 32 H_2O forming molecular water in the 192 atom models for 3000 K and 2400 K (Table 6.1).

to 2400 K. The increase takes place after different amounts of time after quench, between about 10 ps (model 192-1) and 100 ps (model 192-2). As opposed to 3000 K, at 2400 K the period of fluctuations of the number of water molecules can no longer be established with certainty, nor do we consider that the new structural equilibrium has been reached, let alone been sampled sufficiently. However, the pronounced polymerization increase is beyond doubt. Despite this uniform trend of increasing polymerization, the models become structurally more different at 2400 K than at 3000 K.

For the 96 atom models, the situation is different (Fig. 5.7). At 3000 K, fluctuations of the amount of molecular water indicate about the same period of 15 ps, and we assume structural equilibrium is reached. The three models agree in the amount of water molecules of 35% with little scatter, which is higher than in the case of the 192 atom models. After switching to 2700 K and later to 2400 K, the 96 atom models do not reflect the same trend as the 192 atom models. Their behavior does not converge on the complete MD trajectory length at 2400 K of more than 100 ps. The model 96-3 shows an increase of water molecules already at 3000 K which later at 2400 K drops to about the initial value. At 2400 K, models 96-1 and 96-2 show fluctuations around a lower value than at 3000 K.

Q^n-species distribution

Next, we evaluate for each temperature step the time-averaged Q^n-species distribution which is obtained from the analysis of all tetrahedra present in a model (Fig. 5.8). The respective average Q^n-value of each model is plotted in Fig. 5.9. Q^2- and Q^3-species are most abundant in all models, the amount of Q^0 was negligibly small below 0.1%. At 3000 K, the Q^n distribution is similar among the three separate 192 atom models. This similarity is reflected in the close agreement of the average Q^n-value of 2.54 for all 192 atom models at 3000 K (Fig. 5.9). The 96 atom models produce in each separate model a higher

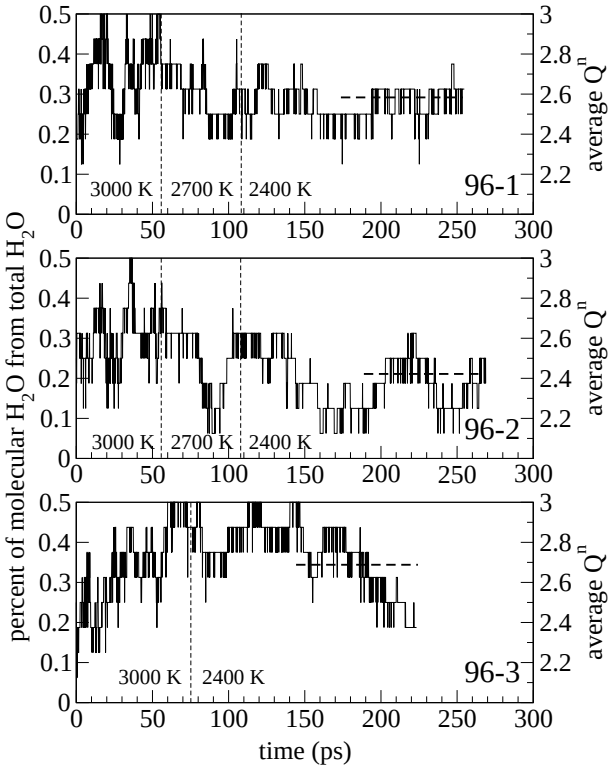

Fig. 5.7: Fraction of total nominal 16 H_2O forming molecular water in the 96 atom models for 3000 K, 2700 K and 2400 K.

degree of polymerization, with a total average Q^n value of 2.72 (Fig. 5.9). The fraction of Q^4-species in the 96 atom models is systematically higher, and the Q^2 content is on average lower than in the 192 atom models.

At 2400 K, the average degree of polymerization of all 192 atom models increases, but the individual average Q^n-values of each model scatter between 2.69 and 2.87 (Fig. 5.9). The average Q^n value correlates well with an increase of Q^3-species and anti-correlates with Q^2-species. The amounts of Q^1- and Q^4-species are still the same in all 192 atom models. The 96 atom models decrease in all three cases the average degree of polymerisation after quench to 2400 K, from the total average of 2.72 at 3000 K to 2.57 at 2400 K (Fig. 5.9). Their Q^n-species distributions are higher in Q^2-species but lower in Q^3- and Q^4-species than the 192 atom models.

Bond dynamics

Finally, we investigate how the dynamics of reaction 6.1 slows down when the system is quenched from 3000 K to 2400 K. The fluctuation of the model structure around an equilibrium structure requires that reaction 6.1 takes place sufficiently often during the MD run, continuously breaking and creating Si-O bonds.

A precise description of the bond dynamics (i.e., the relaxation dynamics) is given by the bond correlation function (BCF, also termed bond population correlation function) (Luzar and Chandler, 1996; Chandra et al., 2007; Vuilleumier and Borgis, 1999; Morrone and Tuckerman, 2002; Chanda et al., 2006). This function expresses the probability that an Si-O bond is still existing after time t, given that it existed at time zero (Luzar and Chandler, 1996). For each timestep of a trajectory, we calculate whether a pair of Si-O is bonded (h=1) or not (h=0). The criterion is the bond distance threshold of 2.4 Å for a Si-O pair

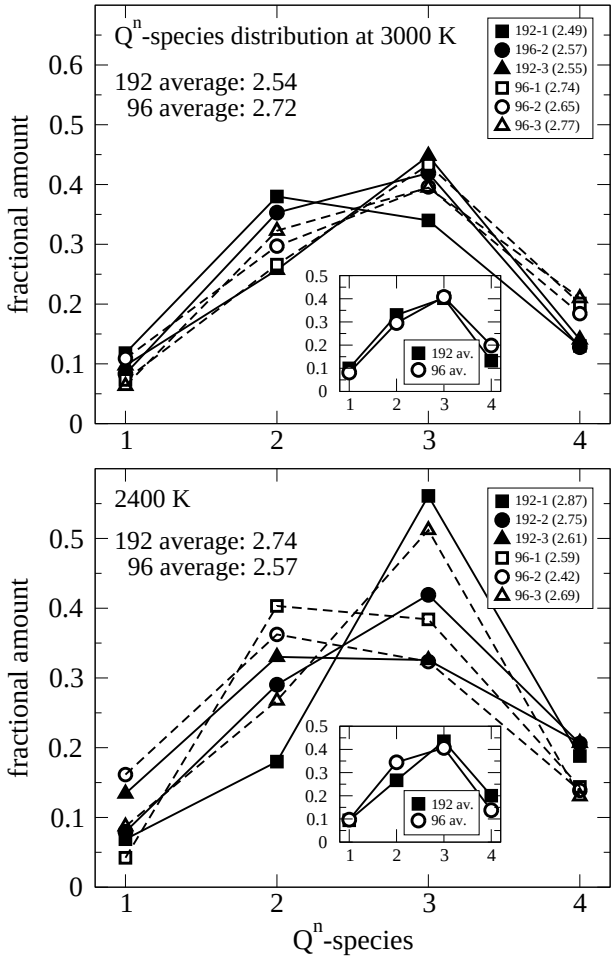

Fig. 5.8: The Q^n-species distribution at 3000 K (top) and 2400 K (bottom) for all 192 and 96 atom models (Table 6.1). See Fig. 5.9 for the average Q^n value of each model. Insets show the average Q^n-species distribution of the 96 atom models and the 192 atom models at 3000 K and 2400 K. Lines are a guide to the eye.

considered to be bonded or not. At 2.4 Å is the first minimum of the Si-O RDF (Fig. 5.3). h changes with time according to whether the bond length is below or above the threshold distance. The time correlation $c(t) = \langle h(0)h(t)\rangle / \langle h\rangle$, with $\langle h\rangle$ being the time average of h, is insensitive to *short-lived* interruptions in the bond's existence. From the BCF we derive a time constant by fitting a single exponentially decaying function (Vuilleumier and Borgis, 1999; Chanda et al., 2006) as $Y = A_0 \exp(-t/\tau_{Si-O})$, where A_0 is a free parameter, and τ_{Si-O} is the time after which the probability of a Si-O bond existence has decayed to 1/e=0.28. The decay is well approximated by a single exponential function (inset in Fig. 6.8).

The results of the Si-O BCF bond time constants are plotted against decreasing temperatures in Fig. 6.8. The scatter between different models is reasonably small. No model size effect can be observed on the bond dynamics. At 3000 K, τ_{Si-O} is about 30 ps, at 2700 K 70 ps, and at 2400 K τ_{Si-O} is about 230 ps for both the 96 and 192 atom models.

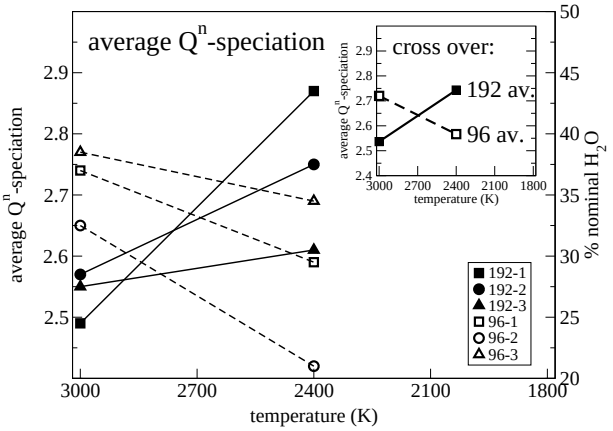

Fig. 5.9: The average Q^n-speciation for all models for 3000 K and 2400 K (Table 6.1). Inset: The average degree of polymerization of the 192 atom models and the 96 atom models versus temperature. Lines are a guide to the eye.

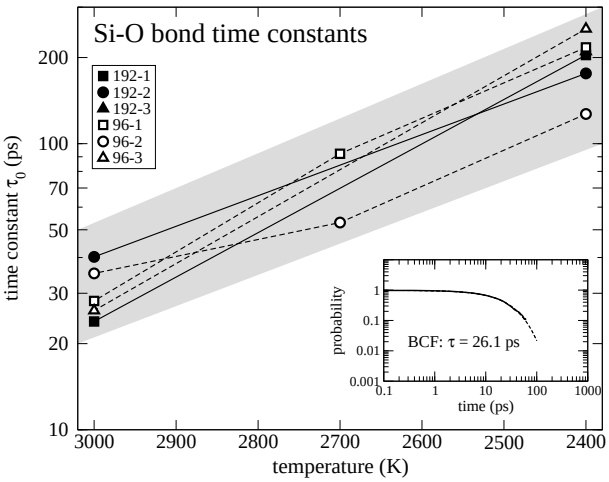

Fig. 5.10: Temperature dependence of the BCF Si-O bond time constants. The inset shows a fit of a single exponential to the bond correlation function (BCF). Lines are a guide to the eye.

5.5 Discussion

Structure at 3000 K

The structural results need to be discussed under several aspects. At 3000 K, the structural results of the three separate 192 atom models are relatively uniform, both in terms of the average Q^n value and the Q^n-species distribution (Figs. 5.8 and 5.9). This shows that the way their initial configurations were generated (HG or RB, Table 6.1) does not have a measurable influence on the structure after few picoseconds at 3000 K. Fluctuation of the total number of molecular water is on the timescales of a few picoseconds. At 3000 K, the Si-O bond time constant is τ_{Si-O}=30 ps. These reasons suggest that structural equilibrium was reached in the MD runs at 3000 K within a few tens of picoseconds. This is also true for the 96 atom models. However, the 96 atom models systematically yield a degree of polymerization larger than the one of the 192 atom models (Fig. 5.9). We address this (seemingly

systematic) difference as a structural finite size effect, see Section 5.5.
The fraction of H_2O present as molecular water in the 192 atom models at 3000 K is 28% on average (Fig. 5.9). As a consequence, the degree of polymerization is higher than the expected nominal average Q^n value based on stoichiometric considerations of 2.0. In the picture of cationic basicity (Flood and Förland, 1947; Fraser, 2005; Moretti, 2005), H_2O (the hydrogen oxide) is the most basic network modifier. Therefore, hydrogen drives the SiO_2 in a stronger polymerized form than less basic cations such as Na_2O would do (Duffy and Ingram, 1976).
The amount of molecular water found in the equimolar SiO_2-H_2O models can be compared to the ab initio MD results of Karki and Stixrude (2010) who found in a silicate melt with 23mol% H_2O at 3000 K only 1% of the water in its molecular speciation. Anderson et al. (2008b), using the classical dissociable Garofalini-potential in a Monte-Carlo study of SiO_2 melt with 40mol% H_2O at 3000 K, found 4% of the H_2O in molecular form. These comparisons give the picture of a steep increase of 1%, 4% and 28% molecular water in melts, where the total content content of H_2O only doubles between 23mol%, 40mol% and 50mol% H_2O. There are many technical details that may account for parts of these differences, such as the initial configuration, run duration, the accuracy of the classical potential, etc. However, the general trend of the steep molecular water increase is in agreement with the Burnham-model of H_2O activity in silicate melts (Burnham, 1974), and with thermodynamic considerations by Newton and Manning (2008). They showed that at 50mol% H_2O, there may be a turning point in the solution mechanism of H_2O in SiO_2. According to them (Newton and Manning, 2008), below 50mol% H_2O, the SiO_2 network is not saturated with respect to hydroxyl groups, and almost all H_2O dissociates. Above 50mol% H_2O, the SiO_2 network is chemically inert to further H_2O input, meaning a steep increase in molecular H_2O around 50mol% H_2O. Our observations are in agreement with these considerations, although one may assume that the change in solution mechanism occurs earlier, around 40mol% or less. Sykes and Kubicki (1993) and Kohn (2000) report a change in the solution mechanism of H_2O in albitic melts at about 30mol% H_2O. We should mention again the large temperature differences between the computational modeling and experiments. Further computational investigation of these changes in the solution mechanism require ab initio sampling of different compositions along the SiO_2-H_2O join under supercritical conditions.

Structural changes upon quench to 2400 K

Between about 10 and 100 picoseconds after quench to 2400 K, the 192 atom models show a remarkable structural rearrangement. The degree of polymerization increases, and in turn the SiO_2 network releases molecular H_2O priorly bound as SiOH hydroxyl groups (Fig. 5.6 and snapshots in Fig. 5.5). The fractional amount of molecular water in the 192 atom models increases between 3000 K and 2400 K on average by 41%. As will be discussed in Section 6.5, structural equilibrium has not been reached in the MD runs at 2400 K, so the process of water release could continue if the runs were longer. The release of water is rather an effect of decreasing temperature than of the drop of pressure, since the structure of silicate melts in the investigated pressure range does not show significant structural changes, such as coordination changes (Mookherjee et al., 2008; Karki and Stixrude, 2010). At 2400 K, the uniform structural picture at 3000 K has been replaced by a variety of average Q^n values and Q^n-species distributions (Fig. 5.8). The average Q^n ranges between 2.61 (model 192-2) to 2.87 (model 192-1). The Q^n-species distributions show a large scatter.
The release of water from the network after lowering the temperature is the expected behavior on the basis of the phase diagram of the system SiO_2-H_2O (Hunt and Manning, 2012). Below 2000 K and 1 GPa, a wide miscibility gap opens over a narrow temperature interval (Fig. 5.1). Although the modeled temperature of 2400 K is still several hundred Kelvin above the real miscibility gap, an increase in the critical compositional fluctuations is expected. Also, the ratio of H_2O and SiOH is expected to increase with decreasing temperature (Kohn, 2000; Newton and Manning, 2008; Hunt and Manning, 2012). Molecular water may cluster to a certain amount without phase separation beyond the nano-scale from the SiO_2 net-

work part. Clustering on the nano-scale is observed in various chemical systems such as silicate glasses and aqueous solution (Vessal et al., 1992; Greaves and Ngai, 1995; Lee et al., 1997; Sunyer et al., 2002; Meyer et al., 2004; Soper et al., 2006; Chandra et al., 2007). There is evidence that critical fluctuations in hydrous melt may even be larger than for any other network modifier (Yamada et al., 2011). For these reasons, we interpret the observed release of molecular water as a precursor of the formation of water clusters in a polymerizing silica network, and eventually as a precursor to phase separation occurring at lower temperatures.

We do not consider the calculation of a reaction constant for reaction 6.1, for several reasons. The temperatures employed in this study are well above any experimentally determined K_d values. Also, the model composition is very unusual. Most importantly, the considerations of Newton and Manning (2008) show the large deviation of activity coefficient from unity which makes the derivation of a reaction constant in the present equimolar composition much less valuable than in the dilute limit as commonly done (Nowak and Behrens, 2001).

Finite size effects in partly broken silica network

The three 192 atom models give mutually consistent structural results with an average Q^n value of 2.54 at 3000 K and 2.75 at 2400 K (Fig. 5.9). The 96 atom models also show a mutually consistent structural change from the average Q^n value of 2.72 at 3000 K to 2.57 at 2400 K. However, the trend of the 96 atom models is in opposite direction to the one of the 192 atom models. The 192 atom models increase the degree of polymerization, whereas the 96 atoms decrease the degree of polymerization with respect to their structures at 3000 K. At 2400 K, each of the 96 atom models show an individual Q^n value higher than any of the 192 atom models. This may not necessarily be true in the long-time limit of several hundreds of picoseconds, as achievable by classical molecular dynamics. However, at 2400 K, the 96 atom models show the inability to reflect the water release demonstrated by the larger 192 atom models on the timescale of hundred picoseconds (Fig. 5.9). On the contrary, the degree of polymerization increases after the 96 models switch to 2400 K. This sheds light on the reliability of structural results on partly broken silica networks from ab initio models of typically about 100 atoms. We address this observation as a combination of the self-confining "caging" finite size effect described above, plus a slowed down reaction dynamics, which will be described in the next Section.

In the case of pure SiO_2 it has been shown by Van Ginhoven et al. (2005) that it is possible to obtain a good structural description of SiO_2 from the average of several small models with less than 100 atoms (Van Ginhoven et al., 2005). According to their results, each small SiO_2 model can be thought of as a small region in a larger system. In the present situation of a partly depolymerized hydrous silica network, this does not seem to be valid. The finite size effect on the structure of *partly depolymerized* silica networks has not been elucidated explicitly before, to the best of our knowledge. However, clustering observations in classical models of silicate glasses with thousands of atoms (Vessal et al., 1992; Sunyer et al., 2002; Meyer et al., 2004) suggest that there is a significant structural finite size effect on the structure of partly depolymerized silica networks, at least up to several hundreds of atoms. The 192 atom models used here are large with respect to the model size of about 100 atoms that is commonly used in ab initio molecular dynamics of silicate glasses and melts, but we cannot assume that the 192 atom models present a structure that is converged with respect to system size.

The impact of model size on the intermediate-range structure (Q^n-distribution) of partly depolymerized silicate networks and on the ability to structurally adapt to changed conditions such as lowered temperature is a very important question. It needs to be thoroughly investigated by classical molecular dynamics. Such a project should, at the same time, investigate the effect of different classical potentials on the Q^n-species distribution.

Bond dynamics as a function of temperature

There is a close dependence of structural equilibration on the temperature of the MD run because temperature determines the bond breaking dynamics crucially on timescales achievable with ab initio MD. The Si-O bond time constant τ_{Si-O} is about 30 ps at 3000 K, 70 ps at 2700 K and about 230 ps at 2400 K. This simple relation allows to quickly estimate whether structural equilibrium in a model can be reached via Si-O bond breaking in a given trajectory length. Most probably, reaching structural equilibrium and sampling it in terms of Q^n speciation at 2400 K is beyond reach in ab initio MD. However, two points are important to note. Firstly, these time constants are a lower limit estimate for the time necessary for structural equilibration, because the equimolar composition under investigation ensures a maximum of interaction between SiO_2 and H_2O. The small size of the models inhibits the formation of clusters of (then "passivated") H_2O molecules. Secondly, these time constants are system-specific. We expect that in other, more ionic systems, such as Na_2O-SiO_2 and MgO-SiO_2, the energy barriers and therefore the time constants may be significantly smaller, indicating that structural equilibrium of the silica network part can be reached within a given MD duration at lower temperatures then in the system H_2O-SiO_2. Compositions closer to naturally occurring hydrous silicate melts include not only SiO_2 and H_2O, but also Na_2O and Al_2O_3 as an approximation to granitic systems. Based on the above reasoning, it can be expected that the Si-O bond dynamics is higher for such melts. Structural equilibrium in such melts could therefore be achievable with common ab initio MD run durations at lower temperatures, eventually down to 2000 K.

5.6 Conclusions

The system SiO_2-H_2O is a first compositional approximation of those natural highly hydrous silicate melts that may form in the crustal wedge above the dehydrating subducted slab in subduction zones. We have investigated supercritical equimolar SiO_2-H_2O fluid at different temperatures and different model sizes under the aspects of structure and structural changes after temperature is decreased. Three points are especially important in our view.

1) We found at 3000 K an average Q^n value of 2.54 and an fraction of molecular H_2O of about 28%. This high content of molecular water at equimolar composition is in agreement with a predicted change in H_2O solution mechanism in silicate melts above about 30mol% H_2O (Newton and Manning, 2008). We found that after quench from 3000 K to 2400 K, the supercritical SiO_2-H_2O fluid releases molecular H_2O on a timescale of tens to hundreds of picoseconds. We interpret this effect as a precursor to critical fluctuations which at even lower temperatures would lead to unmixing.

2) The 96 atom models showed at 3000 K a degree of polymerization consistently higher than the one of the 192 atom models. This points to a structural finite size effect, that is probably stronger on partially depolymerized silicate networks than on pure SiO_2. This finite size effect needs to be investigated further, because it has an impact on the reliability of ab initio MD modeling of silicate melts and glasses in general. At 2400 K, the 192 atom models increase the degree of polymerization, whereas the 96 decrease the degree of polymerization. We interpret this, in addition to the structural finite size effect, as a structure stabilization effect which decreases the probability that smaller models to show the same structural changes as the larger one in the same amount of modeled time.

3) We analyzed the Si-O bond dynamics by bond correlation function to investigate the dissociation reaction H_2O + SiOSi = 2 SiOH. A temperature-time constant relation is described. Si-O bond time constants show that structural equilibrium can not be assured on MD trajectory length of a few tens of picoseconds at 2400 K and below. The presented temperature-time constant relation of Si-O bonds may serve as a guidance to judge whether structural equilibrium can possibly be reached in a given trajectory length. Knowledge of this relation is therefore significant for future modeling in the system SiO_2-H_2O in general, but also for modeling of chemical compositions closer to naturally occurring hydrous silicate

melts (Shen and Keppler, 1997; Stalder et al., 2001; Melekhova et al., 2007; Yamada et al., 2011; Mibe et al., 2011).

Chapter 6
Dynamic properties of silica-rich aqueous fluids

6.1 Abstract

We report several dynamic properties of supercritical silica-rich aqueous fluid with 77wt% SiO_2, obtained from ab initio molecular dynamics between 1800 K and 3000 K and about 2.5 GPa to 4.3 GPa. We calculated bulk self-diffusion coefficients for oxygen, silicon and hydrogen via the Green-Kubo relation from the mean square displacements. Oxygen is distributed among the three different species of bridging oxygen (BO), non-bridging oxygen (NBO) and molecular water oxygen (WO). The self-diffusion coefficient of WO is about four times larger than the one of bulk oxygen. We suggest that the WO-specific self-diffusion coefficient gives a better description of the effective oxygen diffusivity in hydrous silicate melts. We investigated the structural fluctuation dynamics occurring via reaction SiOSi + H_2O = 2SiOH by the calculation of Si-O and O-H bond correlation functions. A relation between decreasing temperature and slowing-down of the Si-O bond breaking dynamics is presented. This relation gives an estimate down to which temperature structural equilibration can be reached for silica-rich aqueous fluids within a given ab initio MD trajectory length.

6.2 Introduction

The system SiO_2-H_2O is of primary importance in geosciences, material science and chemical engineering (Iler, 1979; Lange, 1994; Mysen, 2009; Stalder et al., 2000). At ambient pressures, the system SiO_2-H_2O is dominated by a large region of immiscibility (Kennedy et al., 1962). This region limits the mutual solubility to a few mol% (Newton and Manning, 2008; Kohn, 2000; Burnham, 1974). Therefore, the system SiO_2-H_2O is commonly studied near the dilute limit on either side of the phase diagram. For instance, in optical devices such as silica glass fibers, H_2O is an ubiquitous impurity that alters and degrades the properties of the silica product (Pöhlmann et al., 2004; McMillan and Remmele Jr., 1986; Godet and Pasquarello, 2006). In many studies it is investigated which structural parts of the SiO_2 network are most prone to react with water (Bunker et al., 1989; Awazu and Kawazoe, 2003; Hamann, 1997; Ceresoli et al., 2000). In zeolite research on the aqueous limit of the system SiO_2-H_2O, the cluster formation of silica in solution is investigated (Feuston and Garofalini, 1990; Garofalini and Martin, 1994; Rao and Gelb, 2004; Szyja et al., 2009). In fact, most atomic scale modeling studies of the interaction between silica and water are motivated by either of the latter two applications. An exception to this is the research on silica gels, which are a metastable mixture of both components (Devreux et al., 1990).
In geosciences, the system SiO_2-H_2O is a proxy for the investigation of fluid-rock and fluid-melt interaction (Newton and Manning, 2008; Hunt and Manning, 2012; Gerya et al., 2005). At pressures above 1 GPa, the termn "solidus" of SiO_2 in the presence of H_2O needs to be reconsidered (Stalder et al., 2000). The system SiO_2-H_2O becomes supercritical, SiO_2 and H_2O are completely miscible in a stable state (Kennedy et al., 1962; Paillat et al., 1992; Mysen, 1998; Bureau and Keppler, 1999; Stalder et al., 2000, 2001; Hack et al., 2007; Newton and Manning, 2008; Hack and Thompson, 2010; Hunt and Manning, 2012). The terms fluid and melt for intermediate compositions is a question of semantics. In this study, we refer to this state either as silica-rich fluid or as hydrous silicate melt, if the similarity to silicate melts needs to be emphasized. The upper critical end point (Stalder et al., 2001) at 1 GPa corresponds

to a depth of about 30 km. Such silica-rich fluids may therefore have played a role in the formation of the Earth's crust (Agee, 2008). Even the origin and the location of volcanism today could be governed by the presence of silica-rich fluid in the crustal wedge above subduction zones (Audétat and Keppler, 2004; Mibe et al., 2008). The water dissociation reaction

$$SiOSi + H_2O = 2SiOH, \tag{6.1}$$

is the main chemical interaction of the two molecular subsystems SiO_2 and H_2O. Increasing temperature drives the reaction to the right (Kohn, 2000; Richet, 2005). As is evident from reaction 6.1, oxygen occurs in three species, namely as SiOSi bridging oxygen (BO) between two neighboring SiO_4 tetrahedra, as terminal SiOH non-bridging oxygen (NBO) and as H_2O water oxygen (WO) (Fig. 6.1). Structural and dynamic properties of a hydrous silicate melt depend on the relative amount of these oxygen species and therefore on the extend to which reaction 6.1 proceeds to either side.
For example, the viscosity of silicate melts is directly affected by reaction 6.1. A few weight percent of H_2O in a silicate melt lower its viscosity and mechanical strength by orders of magnitude (Richet and Polian, 1998). This decrease in viscosity is reached by breaking the silica network as in reaction 6.1. Karki and Stixrude (2010) calculated the viscosity of a hydrous silica melt with 23mol% H_2O as 50 mPa·s at 3000 K. This is about two orders of magnitude lower than the viscosity of pure SiO_2 (Karki and Stixrude, 2010). It is important to note that molecular H_2O can fill the voids of silica networks, without significantly lowering its viscosity. This "passiveness" of molecular water cannot be observed in experiment because even at ambient conditions the equilibrium constant of reaction 6.1 is very large and therefore the viscosity-lowering impact of hydroxyl groups overprints the effect of molecular water.

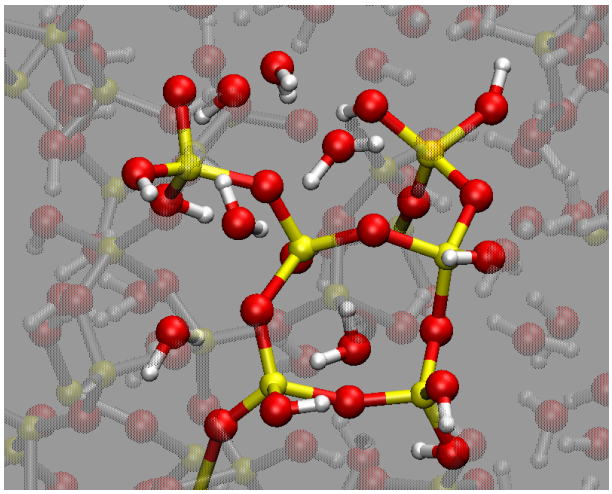

Fig. 6.1: Snapshot of a MD run at 3000 K. The central highlighted part shows several of the three different oxygen species bridging oxygen (BO), non-bridging oxygen (NBO) and water oxygen (WO).

The self-diffusion coefficients in hydrous silicate melts are affected by the presence of H_2O. The experiments investigating the effective "water" diffusivity in hydrous silicate melts have been carried out at H_2O concentrations of a few weight% at most (Zotov et al., 1992; Watson, 1994; Nowak and Behrens, 1997; Behrens and Nowak, 1997; Behrens and Zhang, 2009), and at temperatures much lower than commonly used in molecular dynamics (MD) studies. For this reason, comparison of computational results to experimental diffusivities is difficult. In an ab initio MD study of a hydrous melt with 23mol% H_2O, Karki and Stixrude (2010) found the self-diffusion coefficients to be 10×10^{-9} m^2/s for hydrogen and about 1×10^{-9} m^2/s for oxygen, whereas in a dry melt the bulk oxygen self-diffusion coefficients is

0.05×10^{-9} m^2/s (Karki and Stixrude, 2010). The bulk self-diffusion coefficients of oxygen is calculated from the average mean square displacement of all oxygens, regardless of their speciation. The bulk value therefore covers the different diffusive behavior of the three oxygen species NBO, BO and WO. Usage of the bulk oxygen self-diffusion coefficient in mass transport models implicitly relies on the assumption that the hydrous melt is structurally and chemically homogeneous down to the nanometer scale. The model size in ab initio MD is commonly 100 atoms, which does not allow for clustering, even if it would be expected from experimental observation. However, there is evidence for compositional heterogeneities on the tens of nanometer scale in dry glasses (Vessal et al., 1992; Greaves and Ngai, 1995; Lee et al., 1997; Sunyer et al., 2002; Meyer et al., 2004), dry silicate melts (Polyakov and Ariskin, 2008), aqueous solutions (Soper et al., 2006; Chandra et al., 2007) and hydrous silicate melts (Zavelsky et al., 1998). The oxygen transport through hydrous silica glass proceeds at the speed of water mobility rather than network oxygen mobility (Pfeffer and Ohring, 1981). In experiments, the effective H_2O diffusivity in hydrous silicate melts has been found to be entirely due to the mobility of molecular H_2O, rather than SiOH hydroxyl groups, let alone BO (Watson, 1994; Nowak and Behrens, 1997; Behrens and Nowak, 1997; Nowak and Behrens, 2001; Behrens and Zhang, 2009). Therefore, if in highly hydrous silicate melts the water molecules form clusters or pathways on the nano scale (possibly enhanced by clustering of cations such as sodium), the water oxygen self-diffusion coefficient could give a better estimate for the oxygen diffusivity than the bulk oxygen self-diffusion. Even in very H_2O-rich silicate melts the observed amount of molecular water is low (Karki and Stixrude, 2010), which may be an artifact, since the commonly employed ab initio model sizes of 100 atoms do not allow for clustering to be observed. However, our considerations suggest the calculation of oxygen species-specific self-diffusion coefficients.

The average structure of non-crystalline SiO_2-H_2O mixtures reflects the energy balance and the energetical barrier of reaction 6.1. For this reason, computational studies from different fields of research across the compositional range of SiO_2-H_2O models are dedicated to the energetical aspects of reaction 6.1 (Batyrev et al., 2008; Trinh et al., 2006; Wallace et al., 2010; Bakos et al., 2004). The reaction energy is mostly negative in SiO_2-rich compositions. The reaction volume is considered to be negligibly small (Mysen, 2012). Calculated energy barrier estimates for reaction 6.1 vary between 0.2 eV and 5 eV (Bakos et al., 2004). This large scatter of ab initio energy barrier values results from the fact that reaction 6.1 occurs in the flexible network of SiO_2 with several structural degrees of freedom. These include the variability of the Si-O-Si bending angles, size of the open voids in the network, the direction of H_2O attack and the large atomic translation required in reaction 6.1. It is important to note that all calculated energy barriers are large with respect to the ambient temperature thermal energy of $kT = 26$ meV.

The high energy barrier of reaction 6.1 requires extreme temperatures in conventional unconstrained MD modeling of any composition in the system SiO_2-H_2O, otherwise reaction 6.1 would be an event too rare to reach structural equilibrium in accessible timescales. There is a lower temperature limit down to which structural equilibrium can be reached in typical ab initio MD trajectory lengths of less than a few hundreds of picoseconds. This situation is reflected in several MD studies. Doltsinis et al. (2007) investigated the polymerization reaction of small silica species in aqueous solution at 1200 K and below by ab initio MD, but did not observe a single Si-O bond breaking event in the course of their MD trajectories. Garofalini and co-workers (Feuston and Garofalini, 1990; Garofalini and Martin, 1994) investigated the polymerization of silica clusters in solution. The common temperature of their MD runs was 2500 K. They report that they were able to observe *a few events* of polymerization during several *nanoseconds* long MD runs with a classical potential at 1500 K, but not below. Several other studies confirm this observation, using either the same classical potential as the Garofalini group or ab initio MD (Yamahara and Okazaki, 1998; Rao and Gelb, 2004; Doltsinis et al., 2007). There are numerous computational approaches designed to overcome the problem of reaction energy barriers (Behler et al., 2008; Soper, 1996; Doltsinis, 2006; Bolhuis et al., 2002; Heuer, 2008). They enhance the occurrence of "rare events" and thus can reach minimum energy structures at any temperature, as for instance atomic-scale Monte-Carlo (Anderson et al., 2008b,a). However, information on dynamic properties such as

transport properties cannot easily be obtained from such methods.

The structure of supercritical silica-rich aqueous fluid has recently been investigated by ab initio MD (Chapter 5). A significant increase in polymerization after quench from 3000 K to 2400 K was reported, accompanied by release of molecular water priorly bound to the silica network as SiOH hydroxyl groups. It was shown that the average structure of the models is significantly affected by the model size between 192 atoms and 96 atoms. However, the short-ranged Si-O bond breaking dynamics between 3000 K and 2400 K did not show a dependence on model size.

In the present study, we calculate the self-diffusion coefficients, bond breaking dynamics and viscosity of silica-rich fluid using ab initio MD. The models contain 50mol% SiO_2 and 50mol% H_2O, and their sizes are either 48 atoms (8 SiO_2 + 8 H_2O), 96 atoms (16 SiO_2 + 16 H_2O) or 192 atoms (32 SiO_2 + 32 H_2O). We show how the dynamic properties vary with temperature by running the models in a temperature-cascade-regime, starting at 3000 K and lowering the temperature in steps of 300 K down to 1800 K. The equimolar composition of these models ensures a maximum of interaction between H_2O molecules and the SiO_2 network. It is therefore suited to investigate the temperature dependence of bond dynamics. Si-O and O-H bond time constants are derived from the bond population correlation function (BCF). Thereby we explore the kinetic limitations of ab initio MD modeling of the equilibrium structure of silica-rich fluid. We calculate bulk self-diffusion coefficients for silicon, hydrogen and oxygen, and also separately for water oxygen (WO), and discuss that the self-diffusion coefficient of WO is more meaningful for comparison to experimentally determined diffusivities. We demonstrate that neither the bond lifetime distribution nor the linear (Brownian) diffusive regime of the mean square displacement are reliable measures to decide the question whether structural equilibrium is achieved in a MD run of silica-rich aqeuous fluid, and more general, depolymerized silicate melts. Finally, we demonstrate the effect of molecular water and dissociated water on ficticious "local" viscosities of silica-rich fluids by calculating the viscosities of small 48 atom models.

6.3 Methods

Modeling technique

The modeling for the present study was carried out using the same technical setup as in a preceding study on the structure of the same system (Chapter 5). We use density functional theory (Kohn and Sham, 1965) in the plane wave pseudopotential approach as implemented in the CPMD code (Marx and Hutter, 2000). The exchange-correlation functional is the generalized gradient approximation PBE (Perdew et al., 1996) which has been used in work of other researchers in hydrous silicate melt (Pöhlmann et al., 2004). GGA functionals yield results closer to experiment than LDA for disordered network forming systems (Hamann, 1996, 1997; Massobrio et al., 1999; Van Ginhoven et al., 2005; Demichelis et al., 2010). Martins-Troullier type pseudopotentials (Troullier and Martins, 1991) were used. Spin polarization is commonly assumed not to play a role in silicate melts and has been neglected (Ma et al., 2005). The Kohn-Sham wavefunctions are calculated at the Γ-point with a cutoff energy of 80 Ry. Dependence of forces on more extended k-point sampling was found to be negligible. Forces were within about 1% deviation of the converged value with respect to plane wave cutoff. We use Car-Parrinello MD (Car and Parrinello, 1985) with a ficticious electronic mass of 400 a.u. and an integration time step of 4 a.u. (0.097 fs) (Grossman et al., 2004; Kuo et al., 2004; Schwegler et al., 2004). Atomic positions and velocities were recorded every 40 a.u. The CP-forces agreed to 98% with BO-forces which was checked for several configurations throughout a run, up to 5 ps after the last Born-Oppenheimer wavefunction optimization (Pastore et al., 1991). All modeling runs were performed at constant volume in periodic boundary conditions. Temperature was controlled by a Nosé-Hoover thermostat (Martyna et al., 1992).

System setup

We evaluate the MD trajectories of 96 atom and 192 atom models that have structurally been described in a previous study (Chapter 5). There, for each model size, three separate models had been set up, to investigate the impact of model size on structure and the structural variability of independent models of the same size. In extension to these earlier models, we set up three new separate and mutually fully independent models of each 48 atoms (8 SiO_2 and 8 H_2O) at constant density of 1.88 g/cm^3, which yielded an ab initio pressure of 2.5 GPa at 1800 K and 4.3 GPa at 3000 K. The initial model set up and the run conditions are identical to the settings described in Chapter 5. Pressures were calculated from the stress tensor, to which the Pulay-stress was added to account for incomplete wavefunction basis set (de Koker et al., 2008; Mookherjee et al., 2008). No additional pressure correction term was added due to lack of experimental data for this system at extreme temperatures (Lange, 1994). Temperature cascade runs were performed, starting at 3000 K, in steps of 300 K, down to 1800 K (Table 6.1). At each temperature, the models were equilibrated for at least 12 ps before the production runs which are at least 40 ps long. Three separate models allow to give insight into the variability of properties between structurally slightly different models.

Table 6.1: The time-temperature regime for the three runs of 48 atom models from 3000 K to 1800 K. It is important to note that they are mutually fully independent because their initio configurations were generated separately.

model name:	48-1	48-2	48-3
number of atoms:	48	48	48
cubic cell dimensions:	8.19 Å	8.19 Å	8.19 Å
3000 K:			
total (ps):	69	69	69
equilibration run (ps):	29	29	29
production run (ps):	40	40	40
2700 K:			
total (ps):	52	52	52
equilibration run (ps):	12	12	12
production run (ps):	40	40	40
2400 K:			
total (ps):	52	52	52
equilibration run (ps):	12	12	12
production run (ps):	40	40	40
2100 K:			
total (ps):	83	83	83
equilibration run (ps):	13	13	13
production run (ps):	70	70	70
1800 K:			
total (ps):	163	163	163
equilibration run (ps):	13	13	13
production run (ps):	150	150	150

6.4 Results

Structural aspects

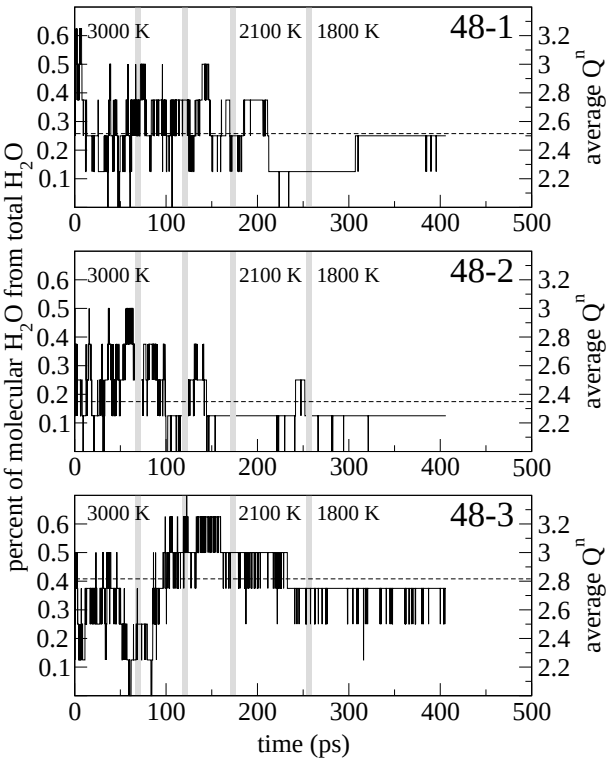

Fig. 6.2: Time-evolution of the fraction of molecular water (left axis) in the 48 atom models on the basis of nominally 8 H_2O molecules. The right axis shows the average degree of polymerization which is linearly coupled to the fraction of molecular water. Quench steps are indicated by grey vertical bars. Dashed horizontal lines indicate the average over the complete trajectory length.

The silica-rich fluid is structurally governed by the relative amounts of the three oxygen species BO, NBO and WO and by the distribution of Q^n-species where Q^n indicates the relative fraction of SiO_4 tetrahedra sharing *n* of its four oxygen with neighboring tetrahedra. The structural aspects of the 96 and 192 atom models have been described in Chapter 5. It was found that "small" 96 atom models are subject to a caging effect by periodic boundary conditions. This sterical effect artificially stabilizes a structure and therefore keeps the models from structural adaptation after, for example, a change of temperature. This caging effect is presumably even stronger for the 48 atom models, whose cubic cell length is 8.19 Å, which is only three times the mean oxygen-oxygen distance in silicate melts (Chapter 5). Therefore, the structures of the 48 atom models should not be considered for evaluation, and we present structural results of the 48 atom models only to completeness. However, it was found in Chapter 5 that the Si-O and O-H bond dynamics and the self-diffusion coefficients are the same for 96 and 192 atom models within the uncertainty of calculation. As we will show in Section 6.4, this is also true for the 48 atom models. Therefore, the three small 48 atom models are a good way to obtain information on dynamic properties and the variability between independent models, at a reasonable computational effort. In Fig. 6.2, the time evolution of the fractional amount of molecular H_2O is shown on the left axis on the basis of nominal 8 H_2O. The right axis indicates the average degree of polymerization, which is linked to the number of water molecules through reaction 6.1. If no water molecule is present, the average degree

of polymerization is 2.0. The average degree of polymerization reaches 3.0 if four water molecules are present. The small model size "quantizes" the structure, and any structural changes necessarily results in large jumps (as in Fig. 6.2). Therefore, the structure strongly varies from one 48 atom model to another, stronger than the 96 and 192 atom models, which can be seen from the Q^n-species distribution in Fig. 6.3.

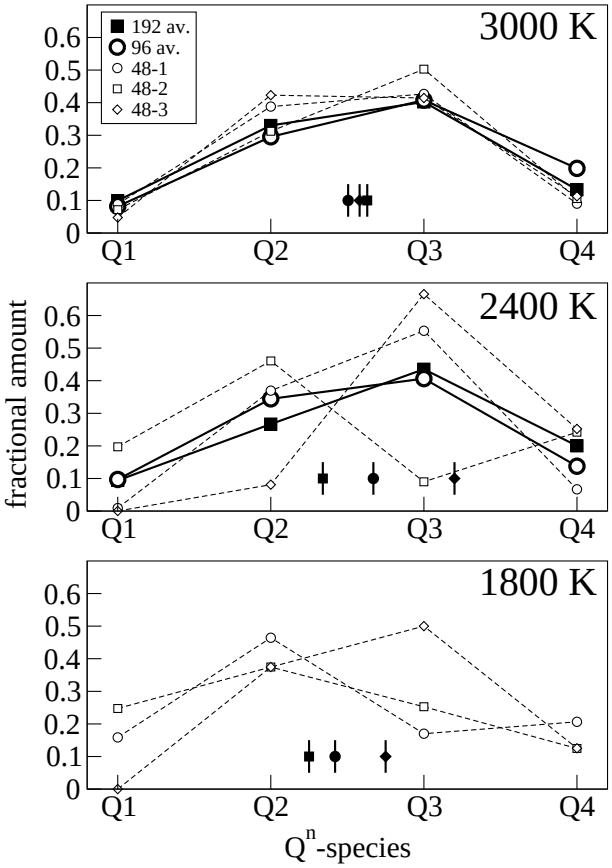

Fig. 6.3: The Q^n-species distribution for the three 48 atom models at 3000 K, 2400 K and 1800 K. The average of the 96 and 192 atom models for 3000 K and 2400 K is shown for comparison. The average degree of polymerization of each 48 atom model is indicated at each temperature by small filled symbols.

Mean square displacement and bulk self-diffusion coefficients

In the remainder of this study, we distinguish between the bulk mean square displacement (MSD) for each element, which is calculated as an average over all atoms of an element, regardless of its speciation, and the species-specific MSD, which is calculated separately for the three oxygen-species BO, NBO and WO. Correspondingly, below we distinguish between the bulk oxygen self-diffusion coefficient D_O and the species-specific water oxygen self-diffusion coefficient D_{WO} We computed the bulk mean square displacement (MSD) as

$$MSD(t) = \frac{1}{N_\alpha} \sum_{i=1}^{N_\alpha} \langle (r_i(t+t_0) - r_i(t_0))^2 \rangle, \tag{6.2}$$

where r_i is the position of i^{th} ion of element α at time t after origin time t_0, and ensemble averages are taken for each element with a total number of atoms N_α. The bulk mean square displacement is

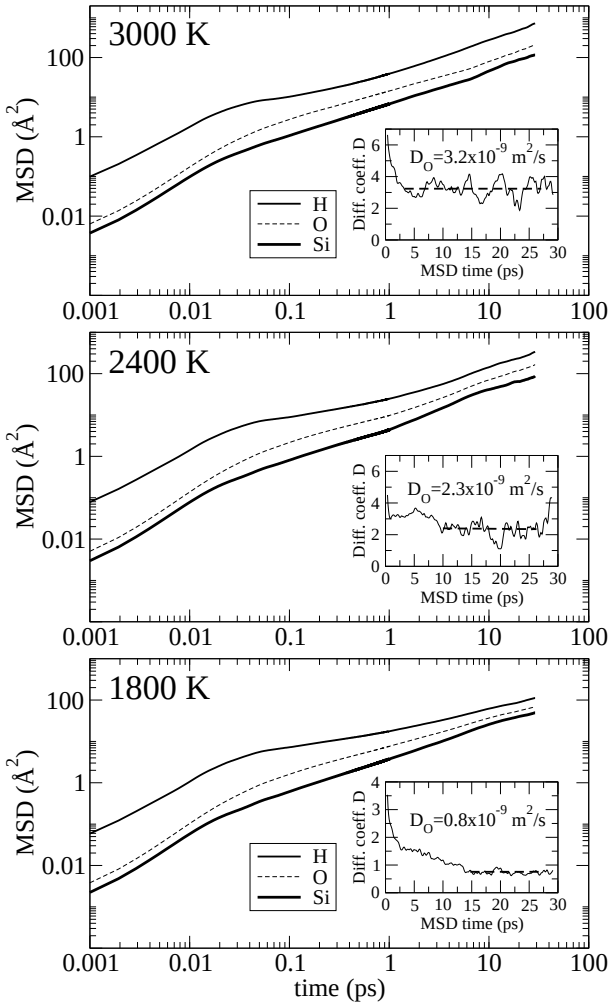

Fig. 6.4: Mean square displacements (MSD) for bulk H, O and Si at 3000 K, 2400 K and 1800 K (from the model 48-1, Table 6.1). Insets: The the slope of the oxygen MSD curve (divided by six, equation 6.3), calculated with a running 0.5 ps time interval. The average of the converged self-diffusion coefficient D_α is indicated by the dashed line.

plotted for 3000 K, 2400 K and 1800 K in Fig. 6.4. The long-time Brownian limit is reached within the correlation time at all temperatures. This can be seen by the convergence of the bulk oxygen MSD slope (in fact, D_O) with respect to the time interval at all temperatures (insets in Fig. 6.4).
From the converged long-term slope of the bulk MSD we derive the bulk self-diffusion coefficient D_α of the individual atomic species from the Einstein relation (Allen and Tildesley, 1987)

$$D_\alpha = \lim_{t\to\infty} \frac{MSD(t)}{6t}. \tag{6.3}$$

The average of the converged bulk oxygen self-diffusion coefficient D_O is indicated in the insets in Fig. 6.4 by dashed horizontal lines. The species-specific WO self-diffusion coefficient D_{WO} is described in the next Section.
The bulk D_O, D_{Si} and D_H are averaged at each temperature over all three 48 atom models and plotted in Fig. 6.5. Error bars indicate the mean absolute error, that is, the variability of the self-diffusion coefficients between the different 48 atom models. The larger 192 atom models reproduce the same temperature trend and even give quantitatively very similar results (Fig. 6.5). The pressure at each

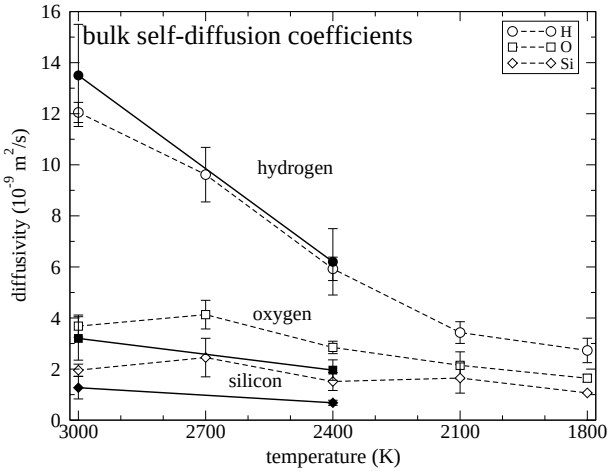

Fig. 6.5: Bulk self-diffusion coefficients for H, O and Si versus temperature. Open symbols: Average of the three 48 atom models. Filled symbols: Average of the three 192 atom models. Error bars indicate the mean absolute error. Lines are a guide to the eye.

temperature is different, because all runs were performed at constant density. However, the pressure effect on the self-diffusion coefficients is expected to be very small, because the structure of silicate melts in the investigated pressure range does not show significant structural changes, such as coordination number increase (Mookherjee et al., 2008; Karki and Stixrude, 2010).
The bulk D_O is about 3.5×10^{-9} m^2/s at 3000 K and 1.8×10^{-9} m^2/s at 1800 K. D_{Si} is about 2.0×10^{-9} m^2/s at 3000 K and about 1×10^{-9} m^2/s at 1800 K. D_H is 12×10^{-9} m^2/s at 3000 K, and decreases gradually to 3×10^{-9} m^2/s at 1800 K. This is only one fourth of its value at 3000 K, whereas D_O and D_{Si} decrease by a factor of two at most in the same temperature range.

Self-diffusion coefficients of oxygen species

We defined a modified MSD function to unmask the diffusive behavior of the WO species. It records the MSD for every single WO and stores the type of species. When a WO changes to a different species, the MSD recording for that oxygen stops. If an oxygen becomes a WO via the reverse of reaction 6.1, the modified MSD calculation starts at zero for that oxygen, storing the displacement from then on. Whether an oxygen is WO or not is calculated at every timestep based on coordinational and bond distance criteria (Chapter 5). Short-lived, accidental changes in the speciation (as described for pairwise bonds below in Section 6.4) are eliminated before-hand by smoothing the species-status time series with a running-average-like discriminator of a 200 fs time window length.
The oxygen species-specific MSDs are plotted for 3000 K, 2400 K and 1800 K in Fig. 6.6, together with the corresponding bulk oxygen MSD from the same model for comparison. For 3000 K and 2400 K, the results are shown from the model 192-1, for 1800 K from the model 48-1. The MSDs of WO are higher (that is, steeper) than the bulk oxygen MSD at all three temperatures, and the BO MSD is less steep. The MSD of NBO matches the one of bulk oxygen, which is as expected, given the large fraction of NBO and their intermediate mobility between WO and BO. The species-specific MSD of WO at 3000 K stops at 10.5 ps, because no water molecule existed for longer than that amount of time. Discontinuities in the MSD curves result from species-change-events. The spikes are more frequent in the MSD curve of the smaller 48 atom models because of the lower number of water molecules and therefore less well averaged MSD. The WO MSD curves at all temperatures reach the long-term linear regime, as can be seen by the fluctuation of the MSD slope (divided by six, see equation 6.3) around an average value (insets in Fig.

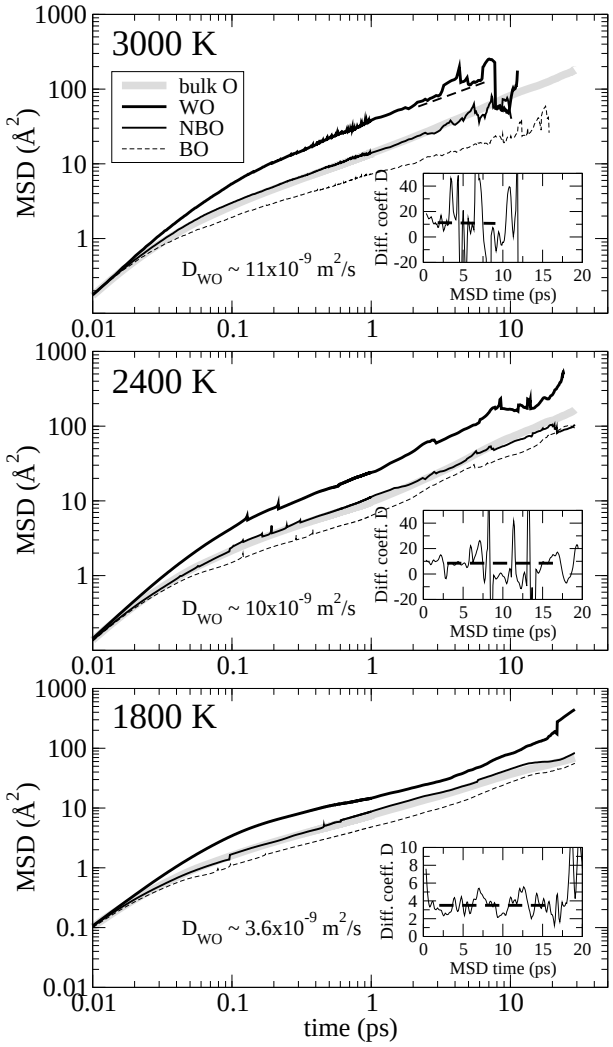

Fig. 6.6: Species-specific mean square displacement (MSD) for the three different oxygen species BO, NBO and WO at 3000 K, 2400 K and 1800 K. The bulk oxygen MSD is shown for comparison (grey). Insets show the slope of the MSD (divided by six, see equation 6.3) as a function of correlation time (with a fitting interval of 0.5 ps width).

6.6, as explained in Section 6.4). The fluctuations in the slope result from the discontinuities in the WO MSD curves mentioned above. The dashed lines represent the averages of the WO-specific self-diffusion coefficients.

The WO-specific self-diffusion coefficient D_{WO} is shown as separate averages over the 48, 96 and 192 atom models in Fig. 6.7. D_H and D_O from Fig. 6.5 are reproduced for comparison. D_{WO} is on overall average 13×10^{-9} m^2/s at 3000 K, which is comparable to D_H, but almost four times higher than D_O. It decreases with decreasing temperature, but at 1800 K the WO-specific value is still more than two times larger than the bulk oxygen self-diffusion coefficient.

Bond dynamics

Next, we investigate the bond breaking dynamics of Si-O and O-H between 3000 K and 1800 K in steps of 300 K (Table 6.1). We use the bond correlation function (BCF, also referred to as bond population correlation function) (Luzar and Chandler, 1996; Vuilleumier and Borgis, 1999; Morrone and Tucker-

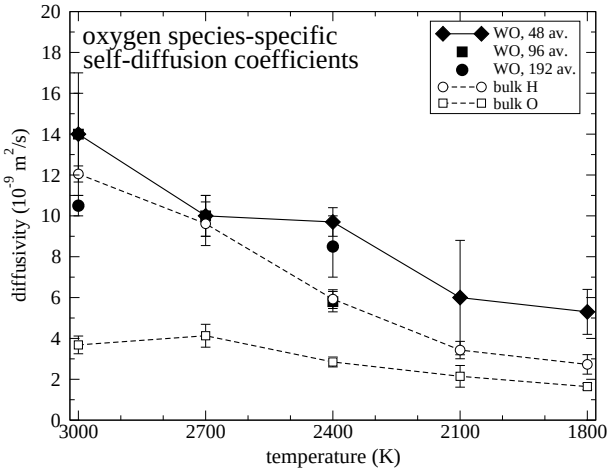

Fig. 6.7: The water oxygen (WO) species-specific self-diffusion coefficient D_{WO}, averaged over the 48, 96 and 192 atom models separately, for all modeled temperatures. Bulk D_O and D_H are shown for comparison. Lines are a guide to the eye.

man, 2002; Chanda et al., 2006; Chandra et al., 2007). In the first step, we determine for each Si-O pair at each timestep whether it is bonded ($h = 1$) or not ($h = 0$). A pair of Si-O is considered as bonded if their distance is below 2.4 Å, which is the position of the first minimum of the Si-O RDF (Chapter 5). The equivalent cutoff for O-H bonds is 1.4 Å. In the second step, the time series of h every Si-O pair is autocorrelated in the BCF as $c(t) = \langle h(0)h(t)\rangle / \langle h\rangle$, with $\langle h\rangle$ being the time average of h. At the common silicate modeling temperatures used in this and other studies, it happens occasionally that pairwise bonds exceed the bond threshold value only for a few femtoseconds, and resume to a lower bond distance. Thus, the bond continues to exist. This behavior is reflected in the pairwise Si-O and O-H RDFs (Chapter 5) where the RDF density at the first minimum does not reach zero, as, for instance, in the RDFs of pure SiO_2 and H_2O at ambient temperatures (Giacomazzi et al., 2009; Grossman et al., 2004; Schwegler et al., 2004). The BCF, as a general feature of autocorrelation functions, is insensitive to such short-lived accidental interruptions of a bond state. The BCF is a normalized decaying function that expresses the probability that an Si-O bond still exists after time t, given that it existed at time zero (Luzar and Chandler, 1996). An example BCF is plotted in the inset in Figure 6.8.

The bond lifetime distribution (BLD) is another measure for bond dynamics (Karki et al., 2010; Karki, 2010). Also here the threshold distances mentioned above are used to discriminate whether a bond exists or not. The BLD is calculated by logging all bond closure and breaking events through the course of a MD trajectory and binning the lifetime of a bond, after it is considered as broken, based on the bond distance criterion. The resulting bond lifetime distribution is also a normalized decaying function (inset in Fig. 6.8). Contrary to the bond correlation function, the BLD is sensitive to short-lived (a few femtoseconds) bond distances that are larger than the bond cutoff threshold. In such situations, the BLD considers the bond as broken and newly formed, whereas the BCF considers the bond as continuing.

From both the BCF and the BLD, we derive bond time constants for Si-O and O-H bonds at each temperature. For this, we separately fit to the BCF and the BLD a single decaying exponential function (Vuilleumier and Borgis, 1999; Chanda et al., 2006) as $Y = A_0 \exp(-t/\tau_{XY})$, where A_0 is a freely varying parameter (close to or equal to 1), and τ_{XY} is the time after which the existence probability of a XY bond has decayed to 1/e=28%. The decay of both the BCF and the BLD is singly exponential, as can be seen by the fits in the inset in Fig. 6.8.

The results of the bond time constants τ_{SiO}^{BCF}, τ_{SiO}^{BLD}, τ_{OH}^{BCF} and τ_{OH}^{BLD} are plotted as separate averages for the 48, 96 and 192 atom models against temperature in Figs. 6.8 and 6.9. The averages of the 48, 96 and 192

atom models are very close to each other, thereby indicating that the bond time constants are not subject to a measurable size effect beyond the uncertainties of our calculation. At 3000 K, for SiO bonds, τ_{SiO}^{BCF} is on total average about 30 ps. This means that after 30 ps, only 1/e=28% of the bonds present at $t = 0$ still exist. At 2700 K, the τ_{SiO}^{BCF} is on average about 60 ps, at 2400 K about 230 ps, and at 1800 K τ_{SiO}^{BCF} reaches about 850 ps. The BLD results give a different picture, because the BLD considers the bonds much more frequently as broken and reformed, regardless whether a bond distance returns below the threshold value a few femtoseconds later. At 3000 K, τ_{SiO}^{BLD} is about 9 ps, at 2700 K it is 18 ps, at 2400 K about 53 ps, and at 1800 K τ_{SiO}^{BLD} reaches 470 ps. The O-H bond time constant τ_{OH}^{BCF} is on average 4 ps at 3000 K, about 7 ps at 2700 K, 11 ps at 2400 K, about 30 ps at 2100 K and finally 310 ps at 1800 K (Fig. 6.9). Also here, the BLD overestimates the dynamics, predicting for 1800 K a bond time constant τ_{OH}^{BLD} of 17 ps. This is more than an order of magnitude less than the value predicted by the BCF.

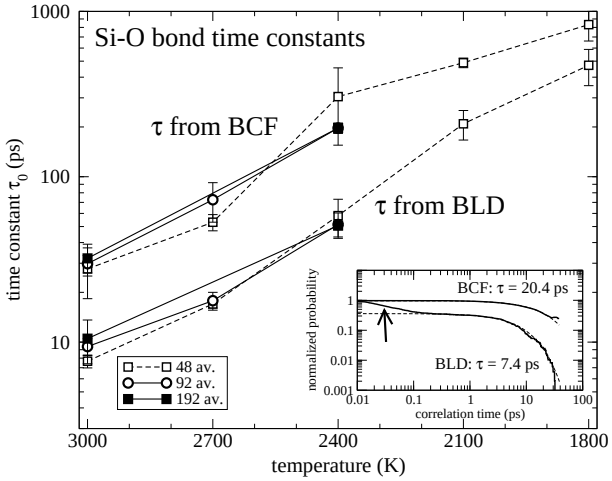

Fig. 6.8: Temperature dependence of the bond time constants τ_{Si-O}^{BCF} and τ_{Si-O}^{BLD}. Results are averaged for each model size of 48, 96 and 192 atoms. Error bars indicate the mean absolute error at each model size. Lines are a guide to the eye. Inset: Single exponential fits to the Si-O BCF and BLD at 3000 K (model 48-1). The arrow indicates the short-time decay of the BLD curve that is caused by short-lived bonds of at most 100 femtoseconds that should not be regarded as bonds. These are the reason why the BLD overestimates bond breaking dynamics.

Viscosity as a function of water dissociation

The three small 48 atom models can be regarded as different "local situations" from a larger model. They allow to calculate a ficticious "local" viscosity of larger models. The viscosity of larger models is calculated as an integral value of many different local averages of degrees of polymerization, and it can therefore not reflect the different contributions of locally varying degrees of polymerization. The small models have different degree of polymerization, and therefore their calculated viscosities allow to get an insight how the degree of polymerization affects the "local" viscosities. The degree of polymerization in the 48 atom models is directly proportional to the fractional amount of molecular water to the sum of molecular and dissociated H_2O. Therefore, the small models allow insight into the local relationship between water dissociation and decrease in viscosity.

We computed the shear viscosity η via the Green-Kubo relation (Allen and Tildesley, 1987) by time integration of the autocorrelation function for the off-diagonal components of the stress tensor as

$$\eta = \frac{V}{k_B T} \int_0^\infty dt \langle \sigma_{ij}(t+t_0)\sigma_{ij}(t_0)\rangle. \tag{6.4}$$

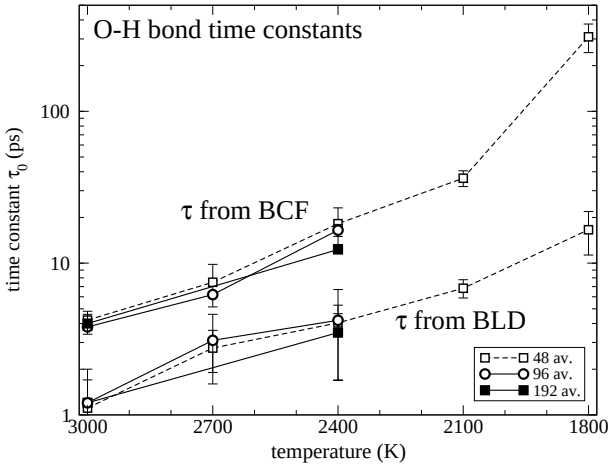

Fig. 6.9: Temperature dependence of the O-H bond time constant. Results are averaged for each model size of 48, 96 and 192 atoms. Error bars indicate the mean absolute error at each model size. Lines are a guide to the eye.

Chevrons denote the average over all running correlation time segments, V is the cell volume, k_B is the Boltzmann constant, and σ_{ij} ($i \neq j$) are the off-diagonal components of the stress tensor σ_{ij}. The three components of the stress tensor are averaged to obtain η (Alfè and Gillan, 1998). In Fig. 6.10 we plot the calculated viscosity of the three 48 atom models for all modeled temperatures (except 1800 K) versus the degree of polymerization (lower axis) and versus the amount of molecular H_2O (upper axis). At 3000 K, the viscosity of the three 48 atom models is on average 14.4 mPa·s with little scatter in the degree of polymerization and therefore little scatter in the viscosity. At lower temperatures, the viscosity reflects the increasing scattering of the average degree of polymerization, which is directly related to the ratio H_2O/OH via reaction 6.1. For example, at 2400 K the viscosity is about 50 mPa·s at average Q^n-value of 2.35, whereas it reaches about 550 mPa·s at an degree of polymerization of 3.15. As indicated by the shaded area, the increase of viscosity is not linear in the degree of polymerization, but rather a percolation limit of polymerization needs to be exceeded for the viscosity to rise steeply. This threshold is estimated to be around 2.7 (Fig. 6.10). The effect of temperature at constant degree of polymerization is indicated by the length of the vertical arrow.

6.5 Discussion

Structure

The structure of silica-rich fluid has been described earlier for the 96 and 192 atom models (see Chapter 5). Structurally, the 48 atom models presented here reproduce well the short-range structure of connected SiO_4^{4-} tetrahedra, terminal SiOH hydroxyl groups and water molecules. However, they cannot reproduce reliably the intermediate-range structure of Q^n-species distribution and average degree of polymerization as found in larger models, for two reasons. Firstly, the structure is subject to a finite size, which is apparent between the 96 and 192 atom models, and likely to act on even smaller models (see Chapter 5). The small volume is "caged" in the periodic boundary conditions which artificially stabilize a given structure, which is sterically kept from structural fluctuation. Secondly, the bond breaking dynamics at temperatures below 2700 K decreases in such a way that the structure does not fluctuate around structural equilibrium in the given trajectory length (see below). The insight into the structure of SiO_2-H_2O fluid is therefore very limited on the basis of the 48 atom models. However, in Chapter 5 it was shown that the

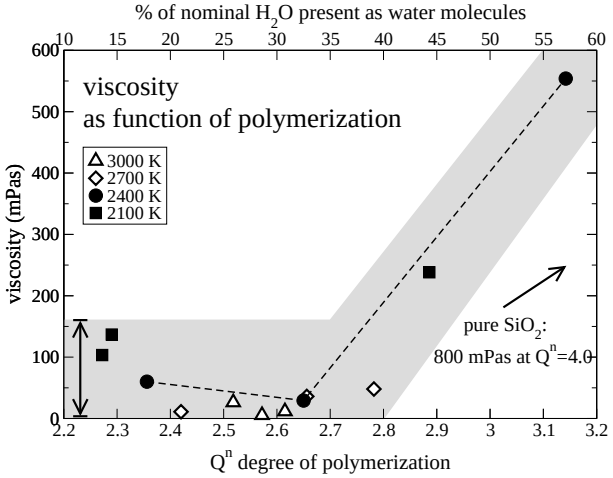

Fig. 6.10: Shear-viscosity of the 48 atom models plotted against the time-averaged degree of polymerization (lower axis) and the fractional amount of molecular H_2O on the basis of 8 H_2O in total (upper axis). The shaded area represents the generalized behavior. The arrow indicates the estimated effect of temperature at constant degree of polymerization between 1800 K and 3000 K. The data for pure SiO_2 was taken from Zhang et al. (2004) for 3300 K and ambient pressure.

bond dynamics (investigated by bond correlation function) does not show an effect of the model size.

Temperature-dependence of bond dynamics

We investigated the Si-O and O-H bond breaking dynamics to get an idea about the temperature down to which structural equilibrium can be reached within tens or at most a few hundreds of picoseconds which is the accessible time scale for ab initio MD. We found that the Si-O bond time constant τ_{SiO}^{BCF} is 30 ps at 3000 K, 230 ps at 2400 K and 850 ps at 1800 K. This simple relation allows to quickly estimate whether structural equilibrium in a model can be reached via Si-O bond breaking in a given trajectory length. Two things are important to note. Firstly, the models investigated here enforce a maximum of interaction between SiO_2 and H_2O, because of their equimolar composition and their small size which does not allow for clustering (and therefore passivation of H_2O molecules). Therefore, the given time constants are a lower time limit needed for structural equilibration. We expect the Si-O bond time constant to increase with increasing H_2O content, because the stiffness of a silica network probably enhances the occurrence of reaction 6.1. Secondly, τ_{SiO}^{BCF} is specific to the chemical system. In other, classically cationic systems such as Na_2O-SiO_2 and MgO-SiO_2, the time constants may be different, because in dry systems changes in the degree of polymerization create free O^{2-} oxygen (Moretti, 2005; Fraser, 2005; Nesbitt et al., 2011), whose valence orbitals are not directionally bonded as in molecular H_2O. Also in hydrous silicate melts involving cations the time constants may be lower than in SiO_2-H_2O, because a fourth oxygen species, OH^- bound loosely to the cations, may be stabilized (LeLosq et al., 2012; Moretti, 2005). OH^- may act as a catalyst for oxygen species interchange. This could be investigated by calculating the Si-O and O-H bond dynamics as function of increasing sodium content in SiO_2-H_2O-Na_2O melts. There are a few other factors that determine whether structural equilibrium at a certain temperature can be reached within a given MD trajectory length, such as the starting configuration. Most probably, reaching structural equilibrium in terms of Q^n speciation in the present model is beyond reach at 2400 K, with τ_{SiO}^{BCF} being about 230 ps (Fig. 6.8).
The bond lifetime distribution (BLD) function systematically overestimates the bond breaking dynamics by considering bonds as broken when in reality they are not broken (Figs. 6.8 and 6.9). The BLD is

therefore not a reliable measure for bond breaking dynamics and the question whether structural equilibrium is achievable within the duration of a MD run. The ratio of the bond time constants from BCF and BLD is not constant for all temperatures. The ratio deserves further investigation.

MSD and self-diffusion coefficients

The bulk oxygen self-diffusion coefficient D_O of about 3.5×10^{-9} m^2/s at 3000 K is in agreement with the corresponding value of 1.0×10^{-9} m^2/s found by Karki and Stixrude (2010) in a silica melt at 3000 K and 0 GPa with only 23mol% H_2O. This is in good agreement, given the difference in H_2O content. D_H is 12×10^{-9} m^2/s at 3000 K, and decreases gradually to 3×10^{-9} m^2/s at 1800 K. This is only one fourth of its value at 3000 K, whereas D_O and D_{Si} in the same temperature range decrease by a factor of two at most. The origin of the decrease in self-diffusion coefficients with decreasing temperature is in the decreasing bond breaking dynamics, as discussed above.
The WO self-diffusion coefficient D_{WO} is at all temperatures at least similar to, but mostly larger than the bulk D_H. At 1800 K, D_{WO} is more than two times higher than bulk D_O, at 3000 K it is four times the value of bulk oxygen. In experimental studies of the diffusive behavior of hydrous silicate melts, the measured quantity is "water diffusivity", and only molecular H_2O contributes to "water" mobility, but not the SiOH hydroxyl groups (Watson, 1994; Nowak and Behrens, 1997, 2001; Behrens and Nowak, 1997). A significant but unknown contribution to the macroscopic water mobility probably results from connected pathways and clusters of molecular H_2O present on the nanoscale even at high temperatures. These cannot be observed in the common ab initio model sizes of 100 or 200 atoms. We suggest that the self-diffusion coefficient of oxygen in silica-rich fluids and hydrous silicate melts is more reasonably approximated by D_{WO} than by bulk D_O.
The mean square displacement (MSD) reaches the Brownian linear regime at all modeled temperatures down to 1800 K, as is shown by the convergence of D_O with MSD time interval (insets in Fig. 6.4). Commonly in MD studies of silicate melts, the long-term linear Brownian behavior of the mean square displacement (MSD) is considered as a measure to decide whether structural equilibrium is reached within a given trajectory length. Based on this MSD measure, one could assume that structural equilibrium has been reached in all trajectories of the present study. The displacement is real. However, the silica network is unchanged while floating through the model, as the Si-O bond dynamics suggests (see above). Therefore, the MSD is misleading, as is shown by the freezing Si-O bond dynamics (see above). We suggest that the presence of a linear regime in the mean square displacement is not an appropriate measure for the question whether structural equilibrium has been reached in a silicate melt MD trajectory.

Viscosity - insight on the effect of dissociation of H_2O

The small 48 atom models can be understood as representative for different areas in larger models, but because of the finite size effect the structural average of several small models is different from the average structure of larger models (as discussed above and in Chapter 5). The representation of local situations in large models by smaller models opens the interesting possibility to visualize the impact of local silica network depolymerization on a local contribution to viscosity. It can be seen how the spatially varying relative amounts of molecular H_2O and SiOH hydroxyl groups affect a ficticious local viscosity directly (Fig. 6.10). Dissociated water breaks the SiO_2 network and lowers viscosity, whereas molecular water in voids leaves the viscosity of the surrounding network closer to that of completely polymerized pure SiO_2.
Our data in Fig. 6.10 give a rather qualitative, yet meaningful insight of how the viscosity is not a linear function of the degree of (local) polymerization. The viscosity rather shows a percolation-threshold-like increase at an average degree of polymerization of about 2.7 to 2.8. By reaching an average Q^n-value of about 3.1, the viscosity has increased by one order of magnitude with respect to the viscosity at Q^n=2.8. We assume that the increase in viscosity slows down at even larger degrees of polymerization, showing

an S-like relation around the percolation limit. It would be interesting to follow this trend even to higher degrees of polymerization in a more systematic way.
Comparison of our results to experimental data or to other computational results is not helpful, for two reasons. The less important reason is the large temperature gap between the temperatures employed here and the highest temperatures reached in experiments (Audétat and Keppler, 2004; Hui et al., 2009; Hack and Thompson, 2010). The effect of temperature at constant degree of polymerization is small (see the arrow in Fig. 6.10), but temperature affects the extend to which reaction the network breaking 6.1 proceeds to the right. For this reason, comparison to experimental viscosities at lower temperatures are not useful. The pressure effects on viscosity are small, a factor three at most (Adjaoud et al., 2008; Hui et al., 2009; Hack and Thompson, 2010). The most important reason why our results cannot easily be compared is that the 48 atom models yield purposely ficticious "local" viscosities of larger models. The calculation of viscosity is subject to a finite size effect (Zhang et al., 2004) whose impact varies with model size, with model composition (for pure SiO_2, converged results are reached with 800 atoms, for Mg_2SiO_4, 500 atoms are sufficient (Adjaoud et al., 2008).) and therefore, most probably, even with the degree of polymerization.
Nonetheless, we do a thought experiment. Consider the computed shear-viscosity of pure SiO_2 at 3300 K and ambient pressure as 800 mPa·s, as reported by Zhang et al. (2004) Leaving aside the above discussed sources of error, comparison of this value to our results of 550 mPa·s at Q^n=3.12 at 2400 K suggests that between Q^n=4.0 and Q^n=3.1 the viscosity is lowered only from 800 mPa·s to 550 mPa·s (Fig. 6.10). Seemingly, the modeled SiO_2 network can host a large fraction of Q^3-species without a strong decrease in viscosity. Weakening starts when Q^2-species appear in large fractions. For these reasons, the viscosity as a function of the average degree of polymerization could be described by a sigmoid-like function, with a slope of almost zero at very low and at very high degrees of polymerization. However, in experiments, the viscosity of silicate melts is significantly lowered at water contents of 0.2wt%, although stoichiometrically the average degree of polymerization is still close to "dry" Q^n-value of Q^n=4.0. In the light of the viscosity-polymerization relation in Fig. 6.10 we suggest that the experimentally determined decrease of melt viscosity caused by small amounts of added water is not caused by average depolymerization of the network from, say, Q^n=4.0 to, for example, Q^n=3.9. We suggest that the viscosity decrease is reached by clustering of SiOH hydroxyl groups and eventually molecular H_2O that form locally high concentrations of Q^2-species (Zotov et al., 1992; Zavelsky et al., 1998). These depolymerized, H_2O- and SiOH-enriched domains would act as weakened zones, leading to an overall decreased viscosity. This line of reasoning should be substantiated on the computational side by extension of the data in Fig. 6.10 to higher degree of polymerization.

6.6 Conclusions

We have investigated several dynamic properties of silica-rich aqueous fluid. We analyzed the Si-O bond breaking dynamics using the bond correlation function and established a relation between decreasing temperature and decreasing bond breaking dynamics. The Si-O bond time constant at 2400 K is about 230 ps, which indicates the necessary order of MD trajectory length required at 2400 K such that a system at 2400 K can be said to reach structural equilibrium. Since these time constants were calculated under conditions most favorable to interaction between SiO_2 and H_2O, they represent minimum estimates. We showed that neither the commonly used bond lifetime distribution (BLD) nor the Brownian long-term linear diffusive limit of the mean square displacement give a reliable measure to answer the question whether in a given MD trajectory, structural equilibrium of the silica species is reached.
We calculated oxygen-species specific self-diffusion coefficients. The one of water oxygen (WO) is at least two times higher than the bulk oxygen self-diffusion coefficient. We suggest that for hydrous silicate melt, the D_{WO} gives a more realistic description of the oxygen diffusivity than the bulk D_O.
We have established a relation between a local average degree of polymerization and the hypothetical

viscosity of the same volume. We have shown that depolymerization below Q^3 is necessary to substantially decrease the viscosity. We take this as indicator of Q^2-species-enriched domains in hydrous silicate melts, and therefore for a tendency of SiOH hydroxyl groups and molecular H_2O to form clusters on the nanoscale even at high temperatures.

Further work on this project will plot self-diffusion coefficients and bond time constants in Arrhenius-like plots to allow closer comparison to experimental values and to calculate activation energies and activation volumes. The ratio of bond time constants calculated from BCF and BLD will be plotted.

Chapter 7
Conclusions and Outlook

This work is aimed to enhance our understanding of dynamical and structural properties of SiO_2-bearing aqueous fluids and glasses. The theoretical basis and frame for this work is ab initio molecular dynamics (MD). A significant part of the effort was dedicated to develop computational "post-processing" algorithms that would make ab initio modeling an even more useful (and ultimately indispensable) tool for scientific work on disordered silicate matter.

In Chapters 2, 3 and 4, the vibrational properties of silica species have been presented for different environments and different degrees of polymerization. For these calculations, a method needed to be theoretically extended and computationally implemented. The mode-decomposition approach, which had previously been applied only to pure SiO_2, H_2O and network-forming salts (Taraskin and Elliott, 1997; Pavlatou et al., 1997; Kalinichev and Heinzinger, 1995) was extended to partially (and completely) depolymerized silica species such as the H_4SiO_4 monomer and the $H_6Si_2O_7$ dimer, and to all other possible degrees of polymerization of the SiO_4^{4-} tetrahedra. The extension of the mode-decomposition approach required considerable effort in theoretical development, since each Q^n-species has its own specific vibrational modes, in addition to the modes common to all Q^n-species such as tetrahedral symmetric stretching. The implementation of the method was written in Fortran90 and termed SPECDOC (SPECtral Decomposition Of Calculated trajectories).

The results, in the form of a comprehensive list of modes for each species and their vibrational frequencies, are of immediate use in the band assignment of Raman spectra of silicate glasses and melts, and silica species in aqueous fluids. The main finding is the corroboration of the bimodal Q^2 tetrahedral symmetric stretching contribution to Raman spectra of silica glasses, which had been previously presumed by Malfait and co-workers (Malfait et al., 2007, 2008; Zakaznova-Herzog et al., 2007) This finding demonstrates that at least a part of the Raman intensity, which is commonly attributed to Q^3-species should instead be attributed to Q^2-species. Another important result from the present work is the prediction of a $H_6Si_2O_7$ dimer vibrational contribution at about $790\,cm^{-1}$. This finding can explain the observed shift of the $770\,cm^{-1}$ to $800\,cm^{-1}$ in "aging" (i.e., polymerizing) silica solutions (Alvarez and Sparks, 1985; Dutta and Shieh, 1985b). There indeed is a sufficiently well resolved Raman band at 790-800 cm^{-1} in experimental spectra which had not been addressed before (Zotov and Keppler, 2000).

It is now up to the Raman specialists to include this insight in future band assignment of Raman spectra. The consequences will probably change our current understanding of how silica species polymerize in glasses, melts and aqueous fluids. The mode-decomposition code is ready to be applied to other future questions, such as the vibrational properties of chemically more complex glasses and melts, or the vibrational mode frequencies of supercritical water. On several occasions throughout the last year, experimentalists expressed to me their interest in having the mode-decomposition applied to the vibrational contributions of the different hydroxyl groups and molecular H_2O dissolved in silicate glasses. The existing code would need almost no modifications for such an modeling investigation which will give considerable insight into the origin of the broad Raman features resulting from O-H stretching vibrations currently being investigated (Mysen, 2012; LeLosq et al., 2012; Mysen, 2009).

I imagine that someone working on experimental Raman spectra of silicate material will be interested in having not only the frequencies, but also the relative Raman intensities of the different vibrational contributions of silica species. Still today, Raman spectroscopists are forced to use several very simple and weakly justified assumptions regarding the relative Raman intensities of, for instance, the tetrahedral

symmetric stretch of Q^0- to Q^4-species (Mysen and Richet, 2005; McMillan, 1984; McMillan et al., 1992; Mysen, 2009, 2010). Raman intensities of silicates can be calculated in various classical approximations (Zotov et al., 1999; Bornhauser and Bougeard, 2001; Bougeard and Smirnov, 2009) and also in ab initio density functional perturbation theory (Putrino and Parrinello, 2002; Giacomazzi et al., 2009; McKeown et al., 2010). These methods should become standard for disordered silicate matter in the future. This is a goal for the next years.

Chapter 5 sheds light on surprising structural changes in several 192 atom models of SiO_2-H_2O fluid that occur within tens picoseconds after quench from 3000 K to 2400 K. The silicate networks increases its degree of polymerization and releases water molecules. We interpret this structural change as a precursor to nano-scale chemical heterogeneity, which eventually could lead to phase-separation at even lower temperatures, if the models were large enough. However, in several smaller 96 atom models, the structural change consistently developed to the opposite direction, that is, decreasing the average degree of polymerization. This poses questions on observed structural changes in studies where *only* the common model size of about 100 atoms or less was used. This find is relevant to any modeler of disordered silicate systems in general.

Chapter 6 investigates the same system as Chapter 5, but under the aspects of dynamics. The equimolar composition ensures maximal interaction between SiO_2 and H_2O via the network breaking reaction H_2O + SiO_2 = 2 SiOH. Therefore, the system is ideally suited to a estimate the upper limit for the Si-O bond breaking dynamics. The main result is the calculated relation between decreasing temperature and decreasing Si-O bond breaking dynamics. The numbers are somehow discouraging for ab initio MD. At 2400 K, the Si-O bond time constant, i.e., its average lifetime, is about 200 ps. In systems with less enforcement of interaction such as aqueous fluids this constant will be even larger. This demonstrates that reaching structural equilibrium of silica species in aqueous fluids requires MD trajectory durations that are far beyond what is nowadays affordable.

The investigated sterical and dynamical limitations of silicate ab initio molecular dynamics call for reliable dissociable classical potentials that are required to overcome the run duration limits of ab initio MD. Dissociable water potentials have been developed before (Feuston and Garofalini, 1990; Garofalini and Martin, 1994; Fogarty et al., 2010; Pinilla et al., 2012), but their reliability at temperatures relevant for geosciences remains to be verified. The established temperature-bond dynamics relation can be a benchmark for future classical potentials.

Bibliography

O. Adjaoud, G. Steinle-Neumann, and S. Jahn. Mg_2SiO_4 liquid under high pressure from molecular dynamics. *Chemical Geology*, pages 184–191, 2008.

C. B. Agee. Static compression of hydrous silicate melt and the effect of water on planetary differentiation. *Earth and Planetary Science Letters*, 265:641–654, 2008.

D. Alfè and M. J. Gillan. First-principles calculation of transport coefficients. *Physical Review Letters*, 81:5161–5164, 1998.

M. P. Allen and D. J. Tildesley. *Computer Simulations of Liquids*. Oxford University Press, Oxford, 1987.

R. Alvarez and D. L. Sparks. Polymerization of silicate anions in solutions at low concentrations. *Nature*, 318: 649–651, 1985.

K. E. Anderson, L. C. Grauvilardell, M. M. Hirschmann, and J. I. Siepmann. Structure and speciation in hydrous silica melts. 2. Pressure effects. *Journal of Physical Chemistry B*, 112:13015–13021, 2008a.

K. E. Anderson, M. M. Hirschmann, and J. I. Siepmann. Structure and speciation in hydrous silica melts. 1. Temperature and composition effects. *Journal of Physical Chemistry B*, 112:13005–13014, 2008b.

N. W. Ashcroft and N. D. Mermin. *Solid State Physics*. Brooks/Cole CENGAGE Learning, Belmont, California, 1976.

A. Audétat and H. Keppler. Viscosity of fluids in subduction zones. *Science*, 303:513–516, 2004.

K. Awazu and H. Kawazoe. Strained Si-O-Si bonds in amorphous SiO_2 materials: A family member of active centers in radio, photo, and chemical processes. *Journal of Applied Physics*, 94:6243–6262, 2003.

K. Baba, A. D. Chave, R. L. Evans, G. Hirth, and R. L. Mackie. Mantle dynamics beneath the east pacific rise at 17 degrees s; insights from the mantle electromagnetic and tomography (melt) experiment. *Journal of Geophysical Research*, 111(B02101), 2006. doi: 10.1029/2004JB003598.

T. Bakos, S. N. Rashkeev, and S. T. Pantelides. H_2O and O_2 molecules in amorphous SiO_2: Defect formation and annihilation mechanisms. *Physical Review B*, 69:195206, 2004.

E. Balan, A. M. Saitta, F. Mauri, and G. Calas. First-principles modeling of the infrared spectrum of kaolinite. *American Mineralogist*, 86:1321–1330, 2001.

R. A. Barrio, F. L. Galeener, E. Martinez, and R. J. Elliott. Regular ring dynamics in AX_2 tetrahedral glasses. *Physical Review B*, 48:15672, 1993.

W. S. Bassett, A. H. Shen, M. Bucknum, and I. M. Chou. A new diamond anvil cell for hydrothermal studies to 2.5 GPa and from -190 to 1200 °C. *Review of Scientific Instruments*, 64:2340–2345, 1993.

I. G. Batyrev, B. Tuttle, D. M. Fleetwood, R. D. Schrimpf, L. Tsetseris, and S. T. Pantelides. Reactions of water molecules in silica-based network glasses. *Physical Review Letters*, 100:105503, 2008.

J. Behler, R. Martonák, D. Donadio, and M. Parrinello. Metadynamics simulations of the high-pressure phases of silicon employing a high-dimensional neural network potential. *Physical Review Letters*, 100:185501, 2008.

H. Behrens and M. Nowak. The mechanisms of water diffusion in polymerized silicate melts. *Contributions to Mineralogy and Petrology*, 126:377–385, 1997.

H. Behrens and Y. Zhang. H_2O diffusion in peralkaline to peraluminous rhyolitic melts. *Contributions to Mineralogy and Petrology*, 157:765–780, 2009.

P. G. Bolhuis, D. Chandler, C. Dellago, and P. L. Geissler. Transition path sampling: Throwing ropes over rough mountain passes, in the dark. *Annual Review of Physical Chemistry*, 53:291–318, 2002.

P. Bopp. A study of the vibrational motions of water in an aqueous $CaCl_2$ solution. *Chemical Physics*, 106: 205–212, 1986.

P. Bornhauser and D. Bougeard. Intensities of the vibrational spectra of siliceous zeolites by molecular dynamics calculations. II - Raman spectra. *Journal of Raman spectroscopy*, 32:279–285, 2001.

D. Bougeard and K. S. Smirnov. Calculation of off-resonance Raman scattering intensities with parametric models. *Journal of Raman spectroscopy*, 40:1704–1719, 2009.

H. Brasse and D. Eydam. Electrical conductivity beneath the bolivian orocline and its relation to subduction processes at the south american continental margin. *Journal of Geophysical Research*, 113(B07109), 2008. doi: 10.1029/2007JB005142.

B. C. Bunker, D. M. Haaland, K. J. Ward, T. A. Michalske, and W. L. Smith. Infrared spectra of edge-sharing silicate tetrahedra. *Surface Science*, 210:406–428, 1989.

H. Bureau and H. Keppler. Complete miscibility between silicate melts and hydrous fluids in the upper mantle: Experimental evidence and geochemical implications. *Earth and Planetary Science Letters*, 165:187–196, 1999.

C. W. Burnham. $NaAlSi_3O_8$-H_2O solutions: A thermodynamic model for hydrous magmas. *Bulletin de la Société Française de Minéralogie et de Cristallographie*, 97:223–230, 1974.

R. Car and M. Parrinello. Unified approach for molecular dynamics and density functional theory. *Physical Review Letters*, 55:2471–2474, 1985.

D. Ceresoli, M. Bernasconi, S. Iarlori, M. Parrinello, and E. Tosatti. Two-membered silicon rings on the dehydroxylated surface of silica. *Physical Review Letters*, 84:3887–3890, 2000.

J. Chanda, S. Chakraborty, and S. Bandyopadhyay. Sensitivity of hydrogen bond lifetime dynamics to the presence of ethanol at the interface of a phospholipid bilayer. *Journal of Physical Chemistry B*, 110:3791–3797, 2006.

A. Chandra, M. E. Tuckerman, and D. Marx. Connecting solvation shell structure to proton transport kinetics in hydrogen-bonded networks via population correlation functions. *Physical Review Letters*, 99:145901, 2007.

S. M. Chemtob, G. R. Rossman, and J. F. Stebbins. Natural hydrous amorphous silica: Quantification of network speciation and hydroxyl content by ^{29}Si MAS NMR and vibrational spectroscopy. *American Mineralogist*, 97: 203–211, 2012.

A. Chopelas. Single crystal Raman spectra of forsterite, fayalite and monticellite. *American Mineralogist*, 76: 1101–1109, 1991.

S. V. Churakov and M. Gottschalk. Perturbation theory based equation of state for polar molecular fluids: I. Pure fluids. *Geochimica et Cosmochimica Acta*, 67:2397–2414, 2003.

D. T. Cromer and J. T. Waber. *International tables for x-ray crystallography, Vol. IV*. Kynoch Press, Birmingham, U.K., 1974.

W. B. De Almeida and P. J. O'Malley. The vibrational spectrum of H_4SiO_4 calculated using ab initio molecular orbital methods. *Journal of Molecular Structure*, 246:179–184, 1991.

W. B. De Almeida and P. J. O'Malley. Ab initio infrared and Raman spectra of the $H_3SiO_4^-$ monomeric anionic species. *Vibrational Spectroscopy*, 5:325–335, 1993.

N. P. de Koker, L. Stixrude, and B. B. Karki. Thermodynamics, structure, dynamics, and freezing of Mg_2SiO_4 liquid at high pressure. *Geochimica et Cosmochimica Acta*, 72:1427–1441, 2008.

R. Demichelis, B. Civalleri, P. D'Arco, and R. Dovesi. Performance of 12 DFT functionals in the study of crystal systems: Al_2SiO_5 orthosilicates and Al hydroxides as a case study. *International Journal of Quantum Chemistry*, 110:2260–2273, 2010.

F. Devreux, J. P. Boilot, F. Chaput, and A. Lecomte. Sol-gel condensation of rapidly hydrolyzed silicon alkoxides: A joint ^{29}Si NMR and small-angle x-ray scattering study. *Physical Review A*, 41:6901–6909, 1990.

D. Dolejš and C. E. Manning. Thermodynamic model for mineral solubility in aqueous fluids: Theory, calibration and application to model fluid-flow systems. *Geofluids*, 10:20–40, 2010.

N. L. Doltsinis. Free energy and rare events in molecular dynamics. In J. Grotendorst, S. Blügel, and D. Marx, editors, *Computational Nanoscience: Do It Yourself!*, pages 375–387. John von Neumann Institute for Computing, Jülich, NIC-Series Vol. 31, 2006.

N. L. Doltsinis, M. Burchard, W. V. Maresch, A. D. Boese, and T. Fockenberg. Ab initio molecular dynamics study of dissolved SiO_2 in supercritical water. *Journal of Theoretical and Computational Chemistry*, 6:49–62, 2007.

R. T. Downs. The RRUFF project: An integrated study of the chemistry, crystallography, Raman and infrared spectroscopy of minerals. *Program and Abstracts of the 19th General Meeting of the International Mineralogical Association in Kobe, Japan*, O03:13, 2006.

D. A. Drabold. Topics in the theory of amorphous materials. *The European Physical Journal B*, 68:1–21, 2009.

J. A. Duffy and M. D. Ingram. An interpretation of glass chemistry in terms of the optical basicity concept. *Journal of Non-Crystalline Solids*, 21:373–410, 1976.

D. J. Durben, P. F. McMillan, and G. H. Wolf. Raman study of the high-pressure behavior of forsterite Mg_2SiO_4 crystal and glass. *American Mineralogist*, 78:1143–1148, 1993.

P. K. Dutta and D. C. Shieh. Influence of alkali chlorides on distribution of aqueous base solubilized silicate species. *Zeolites*, 5:135–138, 1985a.

P. K. Dutta and D. C. Shieh. Raman spectral study of the composition of basic silicate solutions. *Applied Spectroscopy*, 39:343–346, 1985b.

J. E. Earley, D. Fortnum, A. Wojcicki, and J. O. Edwards. Constitution of aqueous oxyanions: Perrhenate, tellurate and silicate ions. *Journal of the American Chemical Society*, 81:1295–1301, 1959.

I. Farnan, S. C. Kohn, and R. Dupree. A study of the structural role of water in hydrous silica glass using cross-polarisation magic angle spinning NMR. *Geochimica et Cosmochimica Acta*, 51:2869–2873, 1987.

A. R. Felmy, H. Cho, J. R. Rustad, and M. J. Mason. An aqueous thermodynamic model for polymerized silica species to high ionic strength. *Journal of Solution Chemistry*, 30:509–525, 2001.

B. P. Feuston and S. H. Garofalini. Oligomerization in silica sols. *Journal of Physical Chemistry*, 94:5351–5356, 1990.

H. Flood and T. Förland. The acidic and basic properties of oxides. *Acta Chemica Scandinavica*, 1:592–604, 1947.

J. C. Fogarty, H. M. Aktulga, A. Y. Grama, and A. C. T. van Duin. A reactive molecular dynamics simulation of the silica-water interface. *Journal of Chemical Physics*, 132:174704, 2010.

D. Fortnum and J. O. Edwards. The Raman spectrum and the structure of the aqueous silicate ion. *Journal of Inorganic and Nuclear Chemistry*, 2:264–265, 1956.

D. G. Fraser. Acid-base properties and structons: Towards a structural model for predicting the thermodynamic properties of silicate melts. *Annals of Geophysics*, 48:549–559, 2005.

R. L. Freed. Ribbeite, a second example of edge-sharing silicate tetrahedra in the leucophoenicite group. *American Mineralogist*, 78:190–194, 1993.

E. Freund. Étude par spectroscopie Raman-laser des solutions aqueuses de silicates de sodium. II. Interprétation des spectres. *Bulletin de la Société Chimique de France*, 7-8:2244–2249, 1973.

F. L. Galeener. Band limits and the vibrational spectra of tetrahedral glasses. *Physical Review B*, 19:4292–4297, 1979.

S. H. Garofalini and G. Martin. Molecular simulations of the polymerization of silicic acid molecules and network formation. *Journal of Physical Chemistry*, 98:1311–1316, 1994.

T. V. Gerya, W. V. Maresch, M. Burchard, V. Zakhartchouk, N. L. Doltsinis, and T. Fockenberg. Thermodynamic modeling of solubility and speciation of silica in H_2O-SiO_2 fluid up to 1300 °C and 20 kbar based on the chain reaction formalism. *European Journal of Mineralogy*, 17:269–283, 2005.

L. Giacomazzi and A. Pasquarello. Vibrational spectra of vitreous SiO_2 and vitreous GeO_2 from first principles. *Journal of Physics: Condensed Matter*, 19:415112, 2007.

L. Giacomazzi, P. Umari, and A. Pasquarello. Medium-range structure of vitreous SiO_2 obtained through first-principles investigation of vibrational spectra. *Physical Review B*, 79:064202, 2009.

M. J. Gillan, D. Alfè, J. Brodholt, L. Vocadlo, and G. D. Price. First-principles modelling of Earth and planetary materials at high pressures and temperatures. *Reports on Progress in Physics*, 69:2365–2441, 2006.

J. Godet and A. Pasquarello. Proton diffusion mechanism in amorphous SiO_2. *Physical Review Letters*, 97:155901, 2006.

R. Gout, G. S. Pokrovski, J. Schott, and A. Zwick. Raman spectroscopic study of aluminum silicate complexation in acidic solutions from 25 to 150 °C. *Journal of Solution Chemistry*, 28(1):73–82, 1999.

R. Gout, G. S. Pokrovski, J. Schott, and A. Zwick. Raman spectroscopic study of aluminum silicate complexes at 20 °C in basic solutions. *Journal of Solution Chemistry*, 29(12):1173–1186, 2000.

G. N. Greaves and K. L. Ngai. Reconciling ionic-transport properties with atomic structure in oxide glasses. *Physical Review B*, 52:6358–6380, 1995.

J. C. Grossman, E. Schwegler, E. W. Draeger, F. Gygi, and G. Galli. Towards an assessment of the accuracy of density functional theory for first principles simulation of water. *Journal of Chemical Physics*, 120:300–311, 2004.

A. C. Hack and A. B. Thompson. Density and viscosity of hydrous magmas and related fluids and their role in subduction zone processes. *Journal of Petrology*, 52:1333–1362, 2010.

A. C. Hack, A. B. Thompson, and M. Aerts. Phase relations involving hydrous silicate melts, aqueous fluids and minerals. *Reviews in Mineralogy and Geochemistry*, 65:129–185, 2007.

D. R. Hamann. Generalized gradient theory for silica phase transitions. *Physical Review Letters*, 76:660–663, 1996.

D. R. Hamann. Energies of strained silica rings. *Physical Review B*, 55:14784–14793, 1997.

R. J. Heaton and P. A. Madden. Fluctuating ionic polarizabilities in the condensed phase: First-principles calculations of the Raman spectra of ionic melts. *Molecular Physics*, 106:1703–1719, 2008.

G. S. Henderson, D. R. Neuville, B. Cochain, and L. Cormier. The structure of GeO_2-SiO_2 glasses and melts: A Raman spectroscopy study. *Journal of Non-Crystalline Solids*, 355:468–474, 2009.

J. Hermann, C. Spandler, A. Hack, and A. V. Korsakov. Aqueous fluid and hydrous melt in high-pressure and ultra-high pressure rocks: Implications for element transfer in subduction zones. *Lithos*, 92:399–417, 2006.

F. Herzog and V. P. Zakaznova-Herzog. Quantitative Raman spectroscopy: Challenges, shortfalls, and solutions - Application to calcium silicate glass. *American Mineralogist*, 96:914–927, 2011.

A. C. Hess, P. F. McMillan, and M. O'Keeffe. Force fields for SiF_4 and H_4SiO_4: Ab initio molecular orbital calculations. *Journal of Physical Chemistry*, 90:5661–5665, 1986.

P. C. Hess. Upper and lower critical points: Thermodynamic constraints on the solution properties of silicate melts. *Geochimica et Cosmochimica Acta*, 60:2365–2377, 1995.

A. Heuer. Exploring the potential energy landscape of glass-forming systems: From inherent structures via metabasins to macroscopic transport. *Journal of Physics: Condensed Matter*, 20:373101, 2008.

P. Hohenberg and W. Kohn. Inhomogeneous electron gas. *Physical Review*, 136:B864–B871, 1964.

M. Hosaka and S. Taki. Raman spectral studies of SiO_2-NaOH-H_2O system solution under hydrothermal conditions. *Journal of Crystal Growth*, 100:343–346, 1990.

P. Hudon, I. Jung, and D. R. Baker. Melting of β-quartz up to 2.0 GPa and thermodynamic optimization of the silica liquidus up to 6.0 GPa. *Physics of the Earth and Planetary Interiors*, 130:159–174, 2002.

H. Hui, Y. Zhang, Z. Xu, P. Del Gaudio, and H. Behrens. Pressure dependence of viscosity of rhyolitic melts. *Geochimica et Cosmochimica Acta*, 73:3680–3693, 2009.

W. Humphrey, A. Dalke, and K. Schulten. VMD - Visual Molecular Dynamics. *Journal of Molecular Graphics*, 14:33–38, 1996.

J. D. Hunt and C. E. Manning. A thermodynamic model for the system SiO_2-H_2O near the upper critical end point based on quartz solubility experiments at 500-1100 °C and 5-20 kbar. *Geochimica et Cosmochimica Acta*, 86: 196–213, 2012.

J. D. Hunt, A. Kavner, E. A. Schauble, D. Snyder, and C. E. Manning. Polymerization of aqueous silica in H_2O-K_2O solutions at 25-200 °C and 1 bar to 20 kbar. *Chemical Geology*, 283:161–170, 2011.

K. Iishi. Lattice dynamics of forsterite. *American Mineralogist*, 63:1198–1208, 1978.

R. K. Iler. *The chemistry of silica*. Wiley-Interscience, New York, 1979.

S. Ispas, N. Zotov, S. De Wisepelere, and W. Kob. Vibrational properties of a sodium tetrasilicate glass: Ab initio versus classical force fields. *Journal of Non-Crystalline Solids*, 351:1144–1150, 2005.

M. Ivanda, R. Clasen, M. Hornfeck, and W. Kiefer. Raman spectroscopy on SiO_2 glasses sintered from nanosized particles. *Journal of Non-Crystalline Solids*, 322:46–52, 2003.

S. Jahn and P. A. Madden. Modeling Earth materials from crustal to lower mantle conditions: A transferable set of interaction potentials for the CMAS system. *Physics of the Earth and Planetary Interiors*, 162:129–139, 2007.

M. C. Johnson, A. T. J. Anderson, and M. J. Rutherford. Pre-eruptive volatile contents in magmas. *Reviews in Mineralogy*, 30:281–330, 1994.

A. G. Kalampounias, N. K. Nasikas, and G. N. Papatheodorou. Glass formation and structure in the $MgSiO_3$-Mg_2SiO_4 pseudobinary system: From degraded networks to ioniclike glasses. *Journal of Chemical Physics*, 131:114513, 2009.

A. G. Kalinichev and K. Heinzinger. Molecular dynamics of supercritical water: A computer simulation of vibrational spectra with the flexible BJH potential. *Geochimica et Cosmochimica Acta*, 59:641–650, 1995.

B. B. Karki. First-principles molecular dynamics simulations of silicate melts: Structural and dynamical properties. *Reviews in Mineralogy and Petrology*, 71:355–389, 2010.

B. B. Karki and L. Stixrude. First-principles study of enhancement of transport properties of silica melt by water. *Physical Review Letters*, 104:215901, 2010.

B. B. Karki, D. Bhattarai, and L. Stixrude. First-principles simulations of liquid silica: Structural and dynamical behaviour at high pressure. *Physical Review B*, 76:104205, 2007.

B. B. Karki, D. Bhattarai, M. Mookherjee, and L. Stixrude. Visualization-based analysis of structural and dynamical properties of simulated hydrous silicate melt. *Physics and Chemistry of Minerals*, 37:103–117, 2010.

G. C. Kennedy, G. J. Wasserburg, H. C. Heard, and R. C. Newton. The upper three-phase region in the system SiO_2-H_2O. *American Journal of Science*, 260:501–521, 1962.

A. K. Kleppe, A. P. Jephcoat, and J. R. Smyth. High-pressure Raman spectroscopic study of Fo_{90} hydrous wadsleyite. *Physics and Chemistry of Minerals*, 32:700–709, 2006.

C. T. G. Knight, J. Wang, and S. D. Kinrade. Do zeolite precursor species really exist in aqueous synthesis media? *Physical Chemistry Chemical Physics*, 8:3099–3103, 2006.

S. Kohara, K. Suzuya, K. Takeuchi, C.-K. Loong, M. Grimsditch, J. K. R. Weber, J. A. Tangeman, and T. S. Key. Glass formation at the limit of insufficient network formers. *Science*, 303:1649–1652, 2004.

S. C. Kohn. The dissolution mechanisms of water in silicate melts; a synthesis of recent data. *Mineralogical Magazine*, 64(3):389–408, 2000.

W. Kohn and L. J. Sham. Self-consistent equations including exchange and correlation effects. *Physical Review*, 140:A1133–A1138, 1965.

B. A. Kolesov and C. A. Geiger. A Raman spectroscopic study of Fe-Mg olivines. *Physics and Chemistry of*

Minerals, 31:142–154, 2004.

V. C. Kress and I. S. E. Carmichael. The compressibility of silicate liquids containing Fe_2O_3 and the effect of composition, temperature, oxygen fugacity and pressure on their redox states. *Contributions to Mineralogy and Petrology*, 108:82–92, 1991.

S. Kroeker and J. F. Stebbins. Magnesium coordination environments in glasses and minerals: New insight from high-field magnesium-25 MAS NMR. *American Mineralogist*, 85:1459–1464, 2000.

D. M. Krol and J. G. van Lierop. Raman study of the water adsorption on monolithic silica gels. *Journal of Non-Crystalline Solids*, 68:163–166, 1984.

J. D. Kubicki and D. Sykes. Molecular orbital calculations on $H_6Si_2O_7$ with a variable Si-O-Si angle: Implications for the high-pressure vibrational spectra of silicate glasses. *American Mineralogist*, 78:253–259, 1993.

J. D. Kubicki and D. G. Sykes. Molecular orbital calculations on the vibrational spectra of Q^3T-(OH) species and the hydrolysis of a three-membered aluminosilicate ring. *Geochimica et Cosmochimica Acta*, 59(23):4791–4797, 1995.

J. D. Kubicki and D. G. Sykes. Ab initio calculation of ^{1}H, ^{17}O, ^{27}Al and ^{29}Si NMR parameters, vibrational frequencies and bonding energetics in hydrous silica and Na-aluminosilicate glasses. *Geochimica et Cosmochimica Acta*, 68:3909–3918, 2004.

J. D. Kubicki, S. E. Apitz, and G. A. Blake. G2 theory calculation on $H_3SiO_4^-$, H_4SiO_4, $H_3AlO_4^{2-}$, $H_4AlO_4^-$, and H_5AlO_4: Basis set and electron correlation effects on molecular structures, atomic charges, infrared spectra, and potential energies. *Physics and Chemistry of Minerals*, 22:481–488, 1995.

I. F. W. Kuo, C. J. Mundy, M. J. McGrath, J. I. Siepmann, J. VandeVondele, M. Sprik, J. Hutter, B. Chen, M. L. Klein, F. Mohamed, M. Krack, and M. Parrinello. Liquid water from first principles: Investigation of different sampling approaches. *Journal of Physical Chemistry B*, 108:12990–12998, 2004.

D. J. Lacks, D. B. Rear, and J. A. Van Orman. Molecular dynamics investigation of viscosity, chemical diffusivities and partial molar volumes of liquids along the MgO-SiO_2 join as functions of pressure. *Geochimica et Cosmochimica Acta*, 71:1312–1323, 2007.

R. A. Lange. The effect of H_2O, CO_2 and F on the density and viscosity of silicate melts. *Reviews in Mineralogy*, 30:331–370, 1994.

R. A. Lange and I. S. E. Carmichael. Density of Na_2O-K_2O-CaO-MgO-FeO-Fe_2O_3-Al_2O_3-TiO_2-SiO_2 liquids: New measurements and derived partial molar properties. *Geochimica et Cosmochimica Acta*, 51:2931–2946, 1987.

A. C. Lasaga. Optimization of CNDO for molecular orbital calculation on silicates. *Physics and Chemistry of Minerals*, 8:36–46, 1982.

A. C. Lasaga and G. V. Gibbs. Quantum mechanical potential surfaces and calculations on minerals and molecular clusters. *Physics and Chemistry of Minerals*, 16:29–41, 1988.

M. Lee, S. K. Saha, C. T. Moynihan, and J. Schroeder. Non-exponential structural relaxation, anomalous light scattering and nanoscale inhomogeneities in glasses. *Journal of Non-Crystalline Solids*, 222:369–375, 1997.

S. H. Lee and J. T. K. Wan. Pressure correction in density-functional calculations. *Physical Review B*, 78:224103, 2008.

C. LeLosq, D. R. Neuville, R. Moretti, and J. Roux. Determination of water content in silicate glasses using Raman spectroscopy: Implications for the study of explosive volcanism. *American Mineralogist*, 97:779–790, 2012.

Y. Liang, R. M. Caetano, and S. Scandolo. Infrared and Raman spectra of silica polymorphs from an ab initio parameterized polarizable force field. *The Journal of Chemical Physics*, 125:194524, 2006.

P. L. Lin and A. D. Pelton. A structural model for binary silicate systems. *Metallurgical Transactions B*, 10B: 667–675, 1979.

A. Luzar and D. Chandler. Effect of environment on hydrogen bond dynamics in liquid water. *Physical Review Letters*, 76(6):928–931, 1996.

Y. Ma, A. S. Foster, and R. M. Nieminen. Reactions and clustering of water with silica surface. *Journal of Chemical Physics*, 122:144709, 2005.

W. J. Malfait, V. P. Zakaznova-Herzog, and W. E. Halter. Quantitative Raman spectroscopy: High-temperature speciation of potassium silicate melts. *Journal of Non-Crystalline Solids*, 353:4029–4042, 2007.

W. J. Malfait, V. P. Zakaznova-Herzog, and W. E. Halter. Quantitative Raman spectroscopy: Speciation of Na-silicate glasses and melts. *American Mineralogist*, 93:1505–1518, 2008.

M. Martinez, M.-P. Gaigeot, D. Borgis, and R. Vuilleumier. Extracting effective normal modes from equilibrium dynamics at finite temperature. *Journal of Chemical Physics*, 125:144106, 2006.

G. J. Martyna, M. L. Klein, and M. Tuckerman. Nosé-Hoover chains: The canonical ensemble via continuous dynamics. *Journal of Chemical Physics*, 97:2635–2643, 1992.

D. Marx and J. Hutter. Ab initio molecular dynamics: Theory and implementation. *Modern Methods and Algorithms of Quantum Chemistry, (ed. J. Grotendorst), Forschungszentrum Jülich, NIC Series*, 1:301–449, 2000.

C. Massobrio, A. Pasquarello, and R. Car. Intermediate range order and bonding character in disordered network-forming systems. *Journal of the American Chemical Society*, 121:2943–2944, 1999.

G. J. McIntosh, P. J. Swedlund, and T. Söhnel. Experimental and theoretical investigations into the counter-intuitive shift in the antisymmetric ν(Si-O) vibrational modes upon deuteration of solvated silicic acid H_4SiO_4. *Physical Chemistry Chemical Physics*, 13:2314–2322, 2011.

D. A. McKeown, M. I. Bell, and R. Caracas. Theoretical determination of the Raman spectra of single-crystal forsterite (Mg_2SiO_4). *American Mineralogist*, 95:980–986, 2010.

P. McMillan. Structural studies of silicate glasses and melts: Applications and limitations of Raman spectroscopy. *American Mineralogist*, 69:622–644, 1984.

P. McMillan and A. M. Hofmeister. Infrared and Raman spectroscopy. *Reviews in Mineralogy*, 18:99–160, 1988.

P. F. McMillan and R. L. Remmele Jr. Hydroxyl sites in SiO_2 glass: A note on infrared and Raman spectra. *American Mineralogist*, 71:772–778, 1986.

P. F. McMillan, G. H. Wolf, and B. T. Poe. Vibrational spectroscopy of silicate liquids and glasses. *Chemical Geology*, 96:351–366, 1992.

E. Melekhova, M. W. Schmidt, P. Ulmer, and T. Pettke. The composition of liquids coexisting with dense hydrous magnesium silicates at 11-13.5 GPa and the endpoints of the solidi in the MgO-SiO_2-H_2O system. *Geochimica et Cosmochimica Acta*, 71:3348–3360, 2007.

J. P. Merrick, D. Moran, and L. Radom. An evaluation of harmonic vibrational frequency scale factors. *Journal of Physical Chemistry*, 111:11683–11700, 2007.

A. Meyer, J. Horbach, W. Kob, F. Kargl, and H. Schober. Channel formation and intermediate range order in sodium silicate melts and glasses. *Physical Review Letters*, 93:027801, 2004.

B. J. Mhin, H.-I. Seo, and S.-J. Kim. Theoretical investigation on the IR spectra of four-membered silicon oxide rings. *International Journal of Quantum Chemistry*, 111:3755–3760, 2010.

K. Mibe, I. M. Chou, and W. A. Bassett. In situ Raman spectroscopic investigation of the structure of subduction-zone fluids. *Journal of Geophysical Research*, 113:B04208, 2008.

K. Mibe, T. Kawamoto, K. N. Matsukage, Y. Fei, and S. Ono. Slab melting versus slab dehydration in subduction-zone magmatism. *Proceedings of the National Academy of Science*, 108:8177–8182, 2011.

M. Mookherjee, L. Stixrude, and B. Karki. Hydrous silicate melt at high pressure. *Nature*, 452:983–986, 2008.

P. B. Moore. Edge-sharing silicate tetrahedra in the crystal structure of leucophoenicite. *American Mineralogist*, 55:1146–1166, 1970.

M. J. Mora-Fonz, R. A. Catlow, and D. W. Lewis. H-bond interactions between silicates and water during zeolite pre-nucleation. *Physical Chemistry Chemical Physics*, 10:6571–6578, 2007.

R. Moretti. Polymerisation, basicity, oxidation state and their role in ionic modelling of silicate melts. *Annals of Geophysics*, 48:583–608, 2005.

J. A. Morrone and M. E. Tuckerman. Ab initio molecular dynamics study of proton mobility in liquid methanol. *Journal of Chemical Physics*, 117(9):4403–4413, 2002.

W. F. Murphy. The rovibrational Raman spectrum of water vapour ν_1 and ν_3. *Molecular Physics*, 36(3):727–732, 1978.

S. C. B. Myneni. Soft x-ray spectroscopy and spectromicroscopy studies of organic molecules in the environment. In P. Fenter, M. Rivers, N. Sturchio, and S. Sutton, editors, *Reviews in Mineralogy and Geochemistry: Applications of Synchrotron Radiation in Low-Temperature Geochemistry and Environmental Science*, pages 485–579. 2002.

B. O. Mysen. Interaction between aqueous fluid and silicate melt in the pressure and temperatures regime of the Earth's crust and upper mantle. *Neues Jahrbuch der Mineralogischen Abhandlungen*, 172:227–244, 1998.

B. O. Mysen. Olivine/melt transition metal partitioning, melt composition, and melt structure - melt polymerization and Q^n-speciation in alkaline earth silicate systems. *Geochimica et Cosmochimica Acta*, 73:4796–4812, 2008.

B. O. Mysen. Solution mechanisms of silicate in aqueous fluid and H_2O in coexisting silicate melts determined in situ at high pressure and high temperature. *Geochimica et Cosmochimica Acta*, 73:5748–5763, 2009.

B. O. Mysen. Structure of H_2O-saturated peralkaline aluminosilicate melt and coexisting aluminosilicate-saturated aqueous fluid determined in situ to 800 °C and ~800 MPa. *Geochimica et Cosmochimica Acta*, 74:4123–4139, 2010.

B. O. Mysen. Silicate-COH melt and fluid structure, their physicochemical properties, and partitioning of nominally refractory oxides between melts and fluids. *Lithos*, 148:228–246, 2012.

B. O. Mysen and J. D. Frantz. Silicate melts at magmatic temperatures: In-situ structure determination to 1651 °C

and effect of temperature and bulk composition on the mixing behaviour of structural units. *Contributions to Mineralogy and Petrology*, 117:1–14, 1994.

B. O. Mysen and P. Richet. *Silicate glasses and melts: Properties and structure*. Elsevier Scientific Publishing Company, 2005.

B. O. Mysen and D. Virgo. Volatiles in silicate melts at high pressure and temperature. 1. Interaction between OH groups and Si^{4+}, Al^{3+}, Ca^{2+}, Na^{+} and H^{+}. *Chemical Geology*, 57:303–331, 1986.

N. K. Nasikas, A. Chrissanthopoulos, N. Bouropoulos, S. Sen, and G. N. Papatheodorou. Silicate glasses at the ionic limit: Alkaline-Earth sub-orthosilicates. *Chemistry of Materials*, 23:3692–3697, 2011.

H. W. Nesbitt, G. M. Bancroft, G. S. Henderson, R. Ho, K. N. Dalby, Y. Huang, and Z. Yan. Bridging, non-bridging and free (O^{2-}) oxygen in Na_2O-SiO_2 glasses: An x-ray photoelectron spectroscopic (XPS) and nuclear magnetic resonance (NMR) study. *Journal of Non-Crystalline Solids*, 357:170–180, 2011.

D. R. Neuville and B. O. Mysen. Role of aluminum in the silicate network: In situ, high-temperature study of glasses and melts on the join SiO_2-$NaAlO_2$. *Geochimica et Cosmochimica Acta*, 60:1727–1737, 1996.

D. R. Neuville, L. Cormier, V. Montouillot, P. Florian, F. Millot, J.-C. Rifflet, and D. Massiot. Structure of Mg/Ca alumosilicate glasses: ^{27}Al NMR and Raman spectroscopy investigations. *American Mineralogist*, 93:1721–1731, 2008.

D. R. Neuville, G. S. Henderson, L. Cormier, and D. Massiot. The structure of crystals, glasses, and melts along the CaO-Al_2O_3 join: Results from Raman, Al L- and K-edge x-ray absorption, and ^{27}Al NMR spectroscopy. *American Mineralogist*, 95:1580–1589, 2010.

M. D. Newton and G. V. Gibbs. Ab initio calculated geometries and charge distributions for H_4SiO_4 and $H_6Si_2O_7$ compared with experimental values for silicates and siloxanes. *Physics and Chemistry of Minerals*, 6:221–246, 1980.

R. C. Newton and C. E. Manning. Thermodynamics of SiO_2-H_2O fluid near the upper critical end point from quartz solubility measurements at 10 kbar. *Earth and Planetary Science Letters*, 274:241–249, 2008.

Y. Noel, M. Catti, P. D'Arco, and R. Dovesi. The vibrational frequencies of forsterite Mg_2SiO_4; an all-electron ab initio study with the CRYSTAL code. *Physics and Chemistry of Minerals*, 33:383–393, 2006.

M. Nowak and H. Behrens. An experimental investigation on diffusion of water on haplogranitic melts. *Contributions to Mineralogy and Petrology*, 126:365–376, 1997.

M. Nowak and H. Behrens. Water in rhyolitic systems: Getting a grip on a slippery problem. *Earth and Planetary Science Letters*, 184:515–522, 2001.

O. Paillat, S. C. Elphick, and W. L. Brown. The solubility of water in $NaAlSi_3O_8$ melts: A re-examination of Ab-H_2O phase relationships and critical behaviour at high pressures. *Contributions to Mineralogy and Petrology*, 112:490–500, 1992.

G. Pastore, E. Smargiassi, and F. Buda. Theory of ab initio molecular-dynamics calculations. *Physical Review A*, 44:6334–6346, 1991.

E. A. Pavlatou, P. A. Madden, and M. Wilson. The interpretation of vibrational spectra of ionic melts. *Journal of Chemical Physics*, 107(24):10446–10457, 1997.

M. C. Payne, M. P. Teter, D. C. Allan, T. A. Arias, and J. D. Joannopoulos. Iterative minimization techniques for ab initio total-energy calculations: Molecular dynamics and conjugate gradients. *Reviews of Modern Physics*, 64:1045–1097, 1992.

J. Perdew, K. Burke, and M. Ernzerhof. Generalized gradient approximation made simple. *Physical Review Letters*, 77:3865, 1996.

J. C. G. Pereira, C. R. A. Catlow, and G. D. Price. Silica condensation reaction: An ab initio study. *Chemical Communications*, 13:1387–1388, 1998.

R. Pfeffer and M. Ohring. Network oxygen exchange during water diffusion in SiO_2. *Journal of Applied Physics*, 52:777–784, 1981.

C. Pinilla, A. H. Irani, N. Seriani, and S. Scandolo. Ab initio parameterization of an all-atom polarizable and dissociable force field for water. *Journal of Chemica Physics*, 136:114511, 2012.

M. Pöhlmann, M. Benoit, and W. Kob. First-principles molecular-dynamics simulations of a hydrous silica melt: Structural properties and hydrogen diffusion mechanism. *Physical Review B*, page 184209, 2004.

V. B. Polyakov and A. A. Ariskin. Simulation of the composition and proportions of anions in polymerized silicate melts. *Glass Physics and Chemistry*, 34:50–62, 2008.

A. Putrino and M. Parrinello. Anharmonic Raman spectra in high-pressure ice from ab initio simulations. *Physical Review Letters*, 88(17):176401, 2002.

N. Z. Rao and L. D. Gelb. Molecular dynamics simulations of the polymerization of aqueous silicic acid and analysis of the effects of concentration of silica polymorph distributions, growth mechanisms, and reaction

kinetics. *Journal of Physical Chemistry*, 108:12418–12428, 2004.

M. C. C. Ribeiro, M. Wilson, and P. A. Madden. On the observation of propagating sound modes at high momentum transfer in viscous liquids and glasses. *Journal of Physical Chemistry*, 108(21):9027–9038, 1998a.

M. C. C. Ribeiro, M. Wilson, and P. A. Madden. The nature of the "vibrational modes" of the network-forming liquid $ZnCl_2$. *Journal of Physical Chemistry*, 109(22):9859–9869, 1998b.

M. C. C. Ribeiro, M. Wilson, and P. A. Madden. Raman scattering in the network liquid $ZnCl_2$ relationship to the vibrational density of states. *Journal of Physical Chemistry*, 110(10):4803–4811, 1999.

P. Richet. Water: An elusive component of silicate melts? *Physics and Chemistry of Glasses*, 46:333–339, 2005.

P. Richet and A. Polian. Water as a dense icelike component in silicate glasses. *Nature*, 281:396–398, 1998.

A. Romero-Serrano, A. Cruz-Ramirez, B. Zeifert, M. Hallen-Lopez, and A. Hernandez-Ramirez. Thermodynamic modelling of the BaO-SiO_2 and SrO-SiO_2 binary melts. *Glass Physics and Chemistry*, 36:171–178, 2010.

J. Sarnthein, A. Pasquarello, and R. Car. Origin of the high-frequency doublet in the vibrational spectrum of vitreous SiO_2. *Science*, 275:1925–1927, 1997.

F. Schilling, R. Trumbull, H. Brasse, C. Haberland, G. Asch, D. Bruhn, K. Mai, V. Haak, P. Giese, M. Munoz, J. Ramelow, A. Rietbrock, E. Ricaldi, and T. Vietor. Partial melting in the central andean crust: A review of geophysical, petrophysical, and petrologic evidence. In O. Oncken, G. Chong, G. Franz, P. Giese, H.-J. Götze, V. Ramos, M. Strecker, and P. Wigger, editors, *The Andes: Active Subduction Orogeny*, Frontiers in Earth Sciences, pages 459–474. Springer-Verlag, Berlin-Heidelberg, 2006.

F. R. Schilling and G. M. Partzsch. Quantifying partial melt fraction in the crust beneath the central andes and the tibetan plateau. *Physics and Chemistry of the Earth Part A: Solid Earth and Geodesy*, 26(4-5):239–246, 2001.

C. Schmidt and A. Watenphul. Ammonium in aqueous fluids to 600 °C, 1.3 GPa: A spectroscopic study on the effects on fluid properties, silica solubility, and K-feldspar to muscovite reactions. *Geochimica et Cosmochimica Acta*, 74:6852–6866, 2010.

E. Schwegler, J. C. Grossman, F. Gygi, and G. Galli. Towards an assessment of the accuracy of density functional theory for first principles simulation of water. II. *Journal of Chemical Physics*, 121:5400–5409, 2004.

J. Sefcik and A. Goddard. Thermochemistry of silicic acid deprotonation: Comparison of gas-phase and solvated DFT calculations to experiment. *Geochimica et Cosmochimica Acta*, 65:4435–4443, 2001.

P. N. Sen and M. F. Thorpe. Phonons in AX_2 glasses: From molecular to band-like modes. *Physical Review B*, 15: 4030–4038, 1977.

S. Sen and J. Tangeman. Evidence for anomalously large degree of polymerization of Mg_2SiO_4 glass and melt. *American Mineralogist*, 93:946–949, 2008.

T. J. Shankland, R. J. O'Connell, and H. S. Waff. Geophysical constraints on partial melt in the upper mantle. *Reviews of Geophysics and Space Physics*, 19(3):394–406, 1981.

A. H. Shen and H. Keppler. Direct observation of complete miscibility in the albite-H_2O system. *Nature*, 385: 710–712, 1997.

A. K. Soper. Empirical potential Monte Carlo simulation of fluid structure. *Chemical Physics*, 202:295–306, 1996.

A. K. Soper, L. Dougan, J. Crain, and J. L. Finney. Excess entropy in alcohol-water solutions: A simple clustering explanation. *Journal of Physical Chemistry B*, 110:3472–3476, 2006.

R. Stalder, P. Ulmer, A. B. Thompson, and D. Günther. Experimental approach to constrain second critical end points in fluid/silicate systems: Near-solidus fluids and melts in the system albite-H_2O. *American Mineralogist*, 85:68–77, 2000.

R. Stalder, P. Ulmer, A. B. Thompson, and D. Günther. High pressure fluids in the system MgO-SiO_2-H_2O under upper mantle conditions. *Contributions to Mineralogy and Petrology*, 140:607–618, 2001.

R. H. Stolen and G. E. Walrafen. Water and its relation to broken bond defects in fused silica. *Journal of Chemical Physics*, 64(6):2623–2631, 1976.

E. Sunyer, P. Jund, W. Kob, and R. Jullien. Molecular dynamics study of the diffusion of sodium in amorphous silica. *Journal of Non-Crystalline Solids*, 307-310:939–945, 2002.

D. Sykes and J. D. Kubicki. A model for H_2O solubility mechanisms in albite melts from infrared spectroscopy and molecular orbital calculations. *Geochimica et Cosmochimica Acta*, 57:1039–1052, 1993.

B. Szyja, A. Jansen, T. Verstraelen, and R. van Santen. Molecular dynamics study of the silica-water-SDA interactions. *Physical Chemistry Chemical Physics*, 11:7605–7610, 2009.

S. N. Taraskin and S. R. Elliott. Nature of vibrational excitations in vitreous silica. *Physical Review B*, 56(14): 8605–8622, 1997.

M. Tokonami. Atomic scattering factor for O^{2-}. *Acta Crystallographica*, 16:485, 1965.

J. Tomasi, B. Mennucci, and R. Cammi. Quantum mechanical continuum solvation models. *Chemical Reviews*, 105:2999–3093, 2005.

J. A. Tossell. Theoretical study of the dimerization of $Si(OH)_4$ in aqueous solution and its dependence on temperature and dielectric constant. *Geochimica et Cosmochimica Acta*, 69(2):283–291, 2005.

A. Trave, P. Tangney, S. Scandolo, A. Pasquarello, and R. Car. Pressure-induced structural changes in liquid SiO_2 from ab initio simulations. *Physical Review Letters*, 89:245504, 2002.

T. T. Trinh, A. P. J. Jansen, and R. A. van Santen. Mechanism of oligomerization reactions of silica. *Journal of Physical Chemistry B*, 110:23099–23106, 2006.

T. T. Trinh, A. P. J. Jansen, R. A. van Santen, and E. J. Meijer. The role of water in silicate oligomerization reaction. *Physical Chemistry Chemical Physics*, 11:5092–5099, 2009.

N. Troullier and J. L. Martins. Efficient pseudopotentials for plane-wave calculations. *Physical Review B*, 43: 1993–2006, 1991.

P. Umari, A. Pasquarello, and A. Dal Corso. Raman scattering intensities in α-quartz: A first-principles investigation. *Physical Review B*, 63:094305, 2001.

P. Umari, X. Gonze, and A. Pasquarello. Concentration of small ring structures in vitreous silica from a first-principles analysis of the Raman spectrum. *Physical Review Letters*, 90(2):027401, 2003.

R. M. Van Ginhoven, H. Jónsson, and L. R. Corrales. Silica glass structure generation for ab initio calculations using small samples of amorphous silica. *Physical Review B*, 71:024208, 2005.

M. Veithen, X. Gonze, and P. Ghosez. Nonlinear optical susceptibilities, Raman efficiencies, and electro-optic tensors from first-principles density functional perturbation theory. *Physical Review B*, 71:125107, 2005.

B. Vessal, G. N. Greaves, P. T. Marten, A. V. Chadwick, R. Mole, and S. Houde-Walter. Cation microsegregation and ionic mobility in mixed alkali glasses. *Nature*, 356:504–506, 1992.

Y. K. Voronko, A. A. Sobol, and V. E. Shukshin. Raman spectra and structure of silicon-oxygen groups in crystalline, liquid and glassy Mg_2SiO_4. *Inorganic Materials*, 42:1080–1087, 2006.

R. Vuilleumier and D. Borgis. Transport and spectroscopy of the hydrated proton: A molecular dynamics study. *Journal of Chemical Physics*, 111(9):4251–4266, 1999.

R. Vuilleumier, N. Sator, and B. Guillot. Computer modeling of natural silicate melts: What can we learn from ab initio simulations. *Geochimica et Cosmochimica Acta*, 73:6313–6339, 2009.

A. F. Wallace, G. V. Gibbs, and P. M. Dove. Influence of ion-associated water on the hydrolysis of Si-O bonded interactions. *Journal of Physical Chemistry A*, 114:2534–2542, 2010.

E. A. Wasserman, D. A. Yuen, and J. R. Rustad. Compositional effects on the transport and thermodynamic properties of MgO-SiO_2 mixtures using molecular dynamics. *Physics of the Earth and Planetary Interiors*, 77: 189–203, 1993a.

E. A. Wasserman, D. A. Yuen, and J. R. Rustad. Molecular dynamics study of the transport properties of perovskite melts under high temperature and pressure conditions. *Earth and Planetary Science Letters*, 114:373–384, 1993b.

E. B. Watson. Diffusion in volatile-bearing magmas. *Reviews in Mineralogy*, 30:371–411, 1994.

M. C. Wilding, C. J. Benmore, J. A. Tangeman, and S. Sampath. Coordination changes in magnesium silicate glasses. *Europhysics Letters*, 67:212–218, 2004.

M. C. Wilding, C. J. Benmore, and J. K. R. Weber. In situ diffraction studies of magnesium silicate liquids. *Journal of Material Science*, 43:4707–4713, 2008.

M. C. Wilding, C. J. Benmore, and J. K. R. Weber. Changes in the local environment surrounding magnesium ions in fragile MgO-SiO_2 liquids. *Europhysics Letters*, 89:26005, 2010.

M. Wilke, C. Schmidt, F. Farges, V. Malavergne, L. Gautron, A. Simionovici, M. Hahn, and P.-E. Petit. Structural environment of iron in hydrous aluminosilicate glass and melt-evidence from x-ray absorption spectroscopy. *Chemical Geology*, 229:144–161, 2006.

M. Wilson and P. A. Madden. Polarization effects, network dynamics, and the infrared spectrum of amorphous SiO_2. *Physical Review Letters*, 77(16):4023–4026, 1996.

A. Yamada, T. Inoue, S. Urakawa, K. Funakoshi, N. Funamori, T. Kikegawa, and T. Irifune. In situ x-ray diffraction study on pressure-induced structural changes in hydrous forsterite and enstatite melts. *Earth and Planetary Science Letters*, 308:115–123, 2011.

K. Yamahara and K. Okazaki. Molecular dynamics simulation of the structural development in sol-gel process for silica systems. *Fluid Phase Equilibria*, 144:449–459, 1998.

V. P. Zakaznova-Herzog, W. J. Malfait, F. Herzog, and W. E. Halter. Quantitative Raman spectroscopy: Principles and application to potassium silicate glasses. *Journal of Non-Crystalline Solids*, 353:4015–4028, 2007.

V. O. Zavelsky, N. I. Bezmen, and V. A. Zharikov. Water in albite glasses: OH-groups, isolated molecules, and clusters. *Journal of Non-Crystalline Solids*, 224:225–231, 1998.

Y. Zhang, G. Guo, K. Refson, and Y. Zhao. Finite size effect at both high and low temperatures in molecular dy-

namics calculations of the self-diffusion coefficient and viscosity of liquid silica. *Journal of Physics: Condensed Matter*, 16:9127–9135, 2004.

N. Zotov and H. Keppler. In situ Raman spectra of dissolved silica species in aqueous fluids to 900 °C and 14 kbar. *American Mineralogist*, 85:600–604, 2000.

N. Zotov and H. Keppler. Silica speciation in aqueous fluids at high pressures and high temperatures. *Chemical Geology*, 184:71–82, 2002.

N. Zotov, Y. Yanev, M. Epelbaum, and L. Konstantinov. Effect of water on the structure of rhyolite glass - x-ray diffraction and Raman spectroscopy studies. *Journal of Non-crystalline Solids*, 142:234–246, 1992.

N. Zotov, I. Ebbsjö, D. Timpel, and H. Keppler. Calculation of Raman spectra and vibrational properties of silicate glasses: Comparison between $Na_2Si_4O_9$ and SiO_2 glasses. *Physical Review B*, 60:6383–6397, 1999.

Erklärung der Eigenständigkeit

Hiermit versichere ich, daß ich die vorliegende Arbeit selbständig verfaßt und keine anderen als die angegebenen Hilfsmittel benutzt habe. Die Stellen der Arbeit, die anderen Werken wörtlich oder inhaltlich entnommen sind, wurden durch entsprechende Angaben der Quellen kenntlich gemacht.

Diese Arbeit hat in gleicher oder ähnlicher Form noch keiner Prüfungsbehörde vorgelegen.